UNIVERSITY OF CALIFORNIA
RIVERSIDE

Titanium-Based Microreactors for Water Purification

A Dissertation submitted in partial satisfaction
of the requirements for the degree of

Doctor of Philosophy

in

Mechanical Engineering

by

Duncan Zetzer Ashby

December 2019

Dissertation Committee:
Dr. Masaru P. Rao, Chairperson
Dr. Guillermo Aguilar
Dr. Alex Greaney

The Dissertation of Duncan Zetzer Ashby is approved:

_____

_____

_____

Committee Chairperson

University of California, Riverside

ACKNOWLEDGEMENTS

I would first like to thank my advisor, Dr. Masaru Rao, for seeing promise in me when I approached him as a Master's student searching for a research lab. When we first met, I had no clue as to what the relationship would become and all the knowledge I would learn under your advisement. Thank you for cultivating a positive environment designed for learning, self-improvement, and personal growth.

I would like to thank all my labmates in the Biomedical Microdevices Laboratory who have been the most supportive and kind people I have known. Thank you, Dr. Omid Khandan, Dr. Shannon Gott, Ryan Peck, Dr. Harish Dixit, Dr. Bryan Woo, Samantha Corber, Pranee Pairs, Kairui Xia, Edver Bahena, Ben Sommerkorn, and Morgan Dundon, the best lab partners, mentors, and peers anyone could ask for. I want to thank all the undergraduate researchers who committed their valuable free time to help me work on these projects, Vinh Nguyen, Kenneth Ply, Taylor Beaulieu, and Alexandrea Jackson, thank you for your dedication. Thank you especially to Harish Dixit and Bryan Woo for the incredible life-long friendships we developed through post-lab meeting climbing sessions and the time we spent living together.

Thank you to our collaborators who helped us to develop the knowledge and understanding needed to build such a successful device. Thank you, Dr. Phillip Christopher and Yibo Jiang for teaching us about photocatalysis and helping to build the first bulk reactor system used to test NPT. Thank you, Dr. Alex Greaney, and Pegah Mirabedini for collaborating with us to develop a deeper understanding of fluid and light interactions with our device; I am greatly looking forward to our future publication together. Thank you, Dr.

Luat Vuong, for being so welcoming and accommodating and helping us learn more about optics.

I would also like to thank Dr. Guillermo Aguilar for involving me in the Window to the Brain. It has truly been a wonderful experience to be a part of such an exciting project. The breadth of knowledge I gained over my four years of involvement will be cherished forever. I want to thank everyone apart of the Windows to the Brain project as well. This is one of the best and brightest groups of people I have ever had the pleasure of working with. Thank you for all the new friendships and unforgettable experiences on this journey.

Thank you to the staff of the Center for Nanoscale Science and Engineering center at UC Riverside for all the training and project guidance you have provided me over my tenure at UC Riverside. It has been an invaluable experience to be able to work so closely with you. Thank you, Mark Heiden, Dr. Dong Yan, and Frank Lee.

I would like to thank my friends and family. Thank you, Michael Nguyen, Randy Baggao, Ralph Torrefranca, Kevin Lamb, and Skyler Bible. Your support and friendships over my entire life have helped me get to this point and I couldn't have done it without each of you. I want to thank my incredible fiancé, Dr. Michelle Tom, for your endless love, support, and compassion. I am so incredibly thankful that our paths crossed at the UC Riverside climbing gym all those years ago. You brought Scout and Fitz into my life and have brought me an infinite amount of happiness. I want to thank my brother, Graham Ashby, for being an incredible best friend and an amazing brother. I'm so proud of your accomplishments. Finally, thank you to my parents, Dr. F. Gregory Ashby and Dr. Heidi

A. Zetzer, for being such amazing role models. Your love and ever-lasting support helped me in so many ways. You are the reason that I pushed on when things were dark and difficult. Thank you for being proof that you can achieve anything, and I have so much appreciation for you. I love you both.

ABSTRACT OF THE DISSERTATION

Titanium-Based Microreactors for Water Purification

by

Duncan Zetzer Ashby

Doctor of Philosophy, Graduate Program in Mechanical Engineering
University of California, Riverside, December 2019
Dr. Masaru P. Rao, Chairperson

A new era of space exploration is on the horizon. Over the past decade interest in crewed missions to Mars and beyond has rapidly developed in the private sector. Innovation in spaceflight has taken center stage but to achieve these ambitious goals improvements to the Environmental Control and Life Support Systems (ECLSS) will be a necessity as well. The system aboard the International Space Station (ISS) can be viewed as a model to assess the demands for sustaining a long-term crew on deep space voyages. Currently, as part of the Water Recovery System (WRS), a thermal catalytic reactor is used to eliminate dissolved low molecular weight volatile organic compounds (VOC). This catalytic reactor uses high temperature and oxygen to oxidize VOCs into harmless by-products. However, components used to maintain the high temperature and pressure fail for more frequently that would be feasible for eventual use in deep space missions. We propose that by replacing the catalytic reactor with photocatalytic microfluidic reactors, which operate at standard temperature and pressure, reliability can be greatly improved.

Herein, we present a multi-faceted study to develop a high-density photocatalytic microfluidic reactor with design enhancements to mitigate common limitations associated with this technology. The first aim was to apply a design of experiments (DOE) approach to optimize nanoporous titania (NPT) for use within the microfluidic reactor concept. NPT is a unique form of titanium dioxide (TiO_2) that directly forms on titanium (Ti) surfaces through a hydrogen peroxide (H_2O_2) based oxidation process. The Taguchi method and grey relational analysis (GRA) were applied to the oxidation conditions (H_2O_2 concentration, temperature, and time) to maximize the reaction rate constant, *k*, and NPT film quality. The second aim applied Ti microelectromechanical systems (MEMS) fabrication techniques to create the first, high-density microfluidic reactor system utilizing a high aspect ratio Ti micropillar array for enhanced catalyst loading and reduced diffusion distance. The micropillar reactors outperformed conventional flat planar reactors and achieved 2-fold or greater photocatalytic activity than all other devices reported in the literature thus far. These results demonstrate the significant performance enhancements of the micropillar array and identify future directions for further validating the concept for use in ECLSS applications.

TABLE OF CONTENTS

LIST OF FIGURES

LIST OF TABLES

1 INTRODUCTION

1.1. Deep Space Exploration and Life Support Systems

A new era of space exploration is rapidly developing in the private sector and the possibility of crewed missions to Mars and beyond is approaching reality. Reaching ambitious destinations will necessitate innovation, not only in the development of advanced spacecraft, but in life-support systems as well. The Environmental Control and Life Support Systems (ECLSS) currently in operation on the International Space Station (ISS) serve as a model to help understand the limitations and demands of sustaining life in the isolated environment of space. Astronauts are typically stationed aboard the ISS for six months at a time, while the total travel time to Mars is slightly longer, around seven months. Due to the ISS's proximity to Earth, it is common, though expensive, to send replacement parts or supplies when needed. However, this may not be possible on long journeys deeper into space. The level of complexity and cost dramatically increases as we seek destinations from Mars and beyond. Crews must be equipped with sufficient resources to survive independently during the seven-month trip to Mars, where upon arrival planetary-based support systems can be developed.

One essential function of these life-support systems is to produce clean potable water, a necessity for sustaining crewmembers aboard these long-term missions. Due to the weight, volume of water, and high demand for uses including consumption, hygiene, oxygen production, and experiments, it is not practical to repeatedly send water to the ISS. Roughly 25 lbs of water (3 gallons) is needed daily to support a crew of six aboard the ISS, while the cost to deliver water to the ISS is around $10,000/lb.[1] In 2008 NASA installed

the Water Recovery System (WRS) on the ISS to cut down costs and decrease the need for frequent re-supplies, the WRS produces 75-100% of the crew's potable drinking water.

The system is comprised of two main components, the Urine Processor Assembly (UPA) and the Water Processor Assembly (WPA), which process waste water collected from urine, humidity condensate, and Sabatier product water (method for repurposing excess carbon dioxide and hydrogen into water) into potable water.[2] After a decade of use on the ISS, the WRS has been successful and continues to produce potable water, however several shortcomings have become apparent and need to be addressed to improve reliability for use in deep space missions. Specifically, there is opportunity for improvement with downstream components, such as the Thermal Catalytic Oxidation Reactor and the Multifiltration Beds which are responsible for removal of volatile organic compounds (VOCs). Figure 1.1 depicts a schematic of the WPA and the process for purification of wastewater.

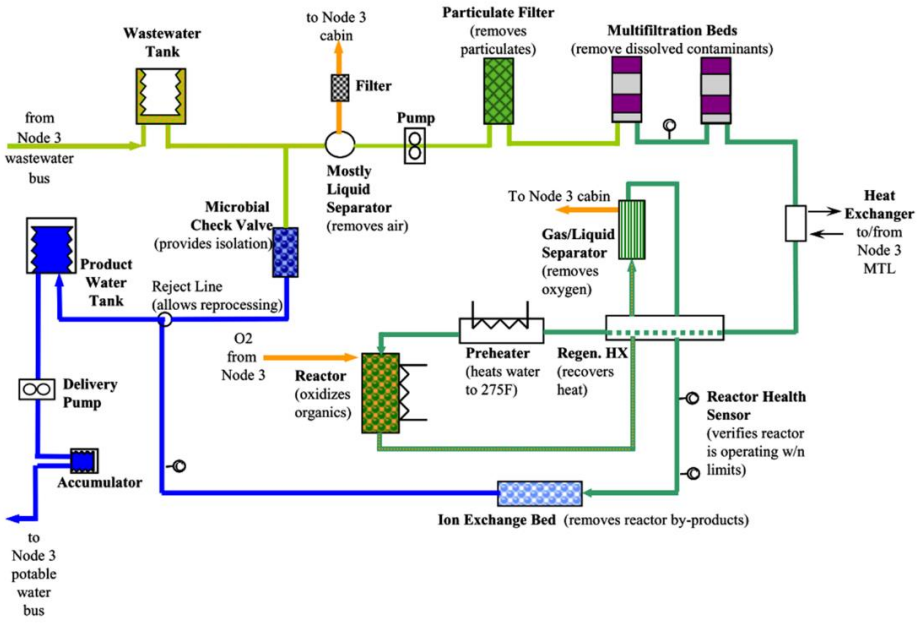

Figure 1.1. Caption on following page.

Figure 1.1. Schematic of the Water Processor Assembly, part of the Water Recovery System used on the International Space Station. The WPA passes collected wastewater through a gas separator to remove odorous air, a series of filtration systems to remove particulate, a catalytic reactor which removes volatile organic compounds, and components to remove oxidation by-products.[3]

1.2. Thermal Catalytic Oxidation Reactor

NASA's target concentration of total organic carbon (TOC) is less than 0.5 ppm TOC, with an upper limit of 3 ppm. Several components of the WPA are design to remove or degrade VOCs to maintain safe TOC levels. The Multifiltration Beds (Figure 1.1) remove large, non-soluble organics by absorbing and removing ionic compounds through ion exchange. However, highly water-soluble non-polar VOCs can pass through the Multifiltration Beds unaffected. An essential downstream component of the WPA is the Thermal Catalytic Oxidation Reactor, which is responsible for removal of low molecular weight VOCs that pass through the Multifiltration Beds.[3] The catalytic reactor is one of the final water processing steps in the WPA and oxidizes the VOCs into water, organic acids, and CO_2, which are then removed via the Ion Exchange Bed. The catalytic reactor operates at high temperatures (265˚F) and pressures (3.7 atm) with an oxygen feed to initiate highly efficient oxidation of VOCs. The high pressure is required to prevent the water from boiling and components upstream from the catalytic reactor operate under the same pressure.[4] The demanding temperature requirements to achieve a high rate of catalytic degradation of VOCs has caused the O-rings within the catalytic reactor to fail on numerous occasions.[5,6] Lower temperature oxidation with alternative catalysts has been investigated but temperatures as high as 200˚F are still required and efficiency equivalent to high temperature oxidation has not been reached.[4] We propose that photocatalytic microreactors

could serve as a replacement to the catalytic oxidation reactor, mitigating the risk of damage to other components by operating at standard temperature and pressure, while requiring only UV-light to initiate removal of VOCs.

1.3. VOC Removal

The catalytic reactor's main function is to oxidize low-weight molecular organics. To test oxidation efficiency of new catalysts, reactors, Multifiltration Beds, and other components, NASA and Hamilton Sundstrand (HS) developed a proprietary solution known as Ersatz, which consists of alcohols, organic acids, and inorganic species.[7] An Ersatz table of contents and concentrations has been included in Appendix A. Future studies for validation of the photocatalytic microreactor concept will attempt to oxidize the Ersatz solutions for direct comparison to the current thermal catalytic reactor.

Beginning in 2010, the TOC analyzer on board the ISS measured unexplained spikes in TOC, which was later identified as dimethylsilanediol (DMSD). At the time it was unclear what the source of the DMSD was and exactly how the WPA was affecting it.[8] Further investigation found that the humidity condensate was largest contributor of DMSD, meaning DMSD was being out-gassed from a source and accumulating in the moisture collected in the air. One of the main sources of DMSD has been found to be personal crew items containing siloxanes, such as hair and skin-care products. The second main source is vapors emitted from cabin adhesives, coatings, paints, and electronics. DMSD is mainly removed by the Multifiltration Bed; however, once the system becomes saturated, excess DMSD passes through the Bed, as well as the rest of the WPA. This

impacts the lifetime of the Multifiltration Beds and can necessitate frequent replacement. While this can be accommodated on the ISS via ground resupply as needed (albeit at high cost),[9] this will not be an option for future deep space missions, thus necessitating the search for a more tractable solution.

DMSD has proven difficult to remove using the systems available in the WPA so alternative removal processes are being investigated to offset the cost of Multifiltration Bed replacements. The most recent research has been on the use of a deep UV light reactor to degrade DMSD. Shortwave UV photons (185 nm and 254 nm) have been demonstrated to break the molecular bonds of siloxane through photo-chemical reactions. Byproducts of this reaction were eventually removed from the gas phase through mineralization into glassy material which condensed onto the chamber walls of the gas-phase reactor.[10] A different flow cell reactor was also tested to investigate penetration depth of shortwave UV for mitigation of DMSD. Three flow orientations, single pass, recycled flow, and single pass with recycled flow, were also explored to determine how the flow-cell reactor may be situated in-line within the WPA system. A single pass configuration is needed to position this system inline on the ISS WRS, however the single pass mode was not as efficient as the recycled mode. Long residence times of up to 120 minutes were investigated for the single pass system. With a chamber volume of approximately 31 ml, this would yield flow rates as low as 260 μL/min in an active flow system, which is within the operational capabilities of microfluidic reactors. The single pass flow cell reactor degraded approximately 60% of a 75 ppm (parts per million) DMSD solution over 120 minutes of UV exposure and yielded a reaction rate constant on the order of bulk reactor systems.[11]

Further innovation is required before this device will be ready for use on the ISS. Microfluidic reactors are a potential solution which can improve reaction rates by 1000x over bulk reactor systems. The long residence time required for effective degradation of DMSD using the flow cell reactor indicates that a microfluidic reactor, capable of flow rates on the order of 260 μL/min, may be just as effective but with a smaller footprint. The DMSD degradation performance of the flow cell reactor serves as a benchmark for future studies to evaluate the capabilities of microfluidic reactors and their use for removal of a variety of VOCs.

1.4. Device Proposal

Herein, we propose that titanium dioxide (TiO_2) photocatalytic microfluidic reactors (PMFR), could be an effective replacement to thermal catalytic oxidation reactors in ECLSS systems for deep space exploration. This is due to the potential afforded by PMFRs for operating at far lower temperatures and pressures, as well as exploiting the UV-rich environment of space, thus collectively providing opportunity for increased reliability and drastic reduction in size, weight, and power (SWaP). The proposed device concept combines titanium (Ti) microelectromechanical systems (MEMS) fabrication techniques with TiO_2–based photocatalysis to create the first, high density water purification system utilizing a high aspect ratio Ti micropillar array for enhanced catalyst loading. The micropillar array serves as scaffolding for catalyst fixation and significantly increases the catalyst surface area-to- reactor volume (SA:V) ratio. Additional benefits include a reduced and fixed mass diffusion distance, and improved photon utilization through light trapping.

Design of experiments (DOE) optimized nanoporous titania (NPT) is used as the photocatalyst within the PFMR concept to deposit a homogeneous layer of TiO_2 across all surfaces. The benefits of the proposed device could alleviate the key shortcomings reported for microfluidic reactors, namely throughput. In short, the advantages of the micropillar scaffolding improve the degradation efficiencies without the need to scale-up the device, thus leading to increased throughput and photocatalytic performance compared to conventional planar reactor designs.

1.5. Dissertation Outline

This dissertation details the efforts taken to optimize NPT for use within a microfluidic system and the design, fabrication, and evaluation of a novel Ti PMFR concept. Chapter 2 presents an overview of photocatalytic microreactors and the current state of research within the field is presented to establish a narrative for drawing comparisons. Chapter 3 describes the methods of titanium microfabrication, as considerable time was spent improving upon these processes, largely done in-house at UC Riverside. Chapter 4 details a study to optimize NPT for use within microfluidic reactors. Taguchi DOE and grey relational analysis were used to evaluate NPT growth parameters and optimized conditions were found that equally balanced maximizing the reaction rate constant and minimizing crack size. Chapter 5 covers a study to evaluate the efficacy of micropillar scaffolding within the PMFR concept. Two reactor designs were fabricated, one with micropillars and the other without otherwise identical, and etched to three different depths for directly evaluating the effect of scaffolding. An extensive literature

comparison is also presented to demonstrate the PMFR concept's marked improvements over all other devices reported to date. Finally, Chapter 6 includes a summary of the findings and discusses future directions, such as degradation of VOCs and viral species, and design improvements.

2 MICROREACTORS AND TITANIUM DIOXIDE

2.1. Photocatalysis

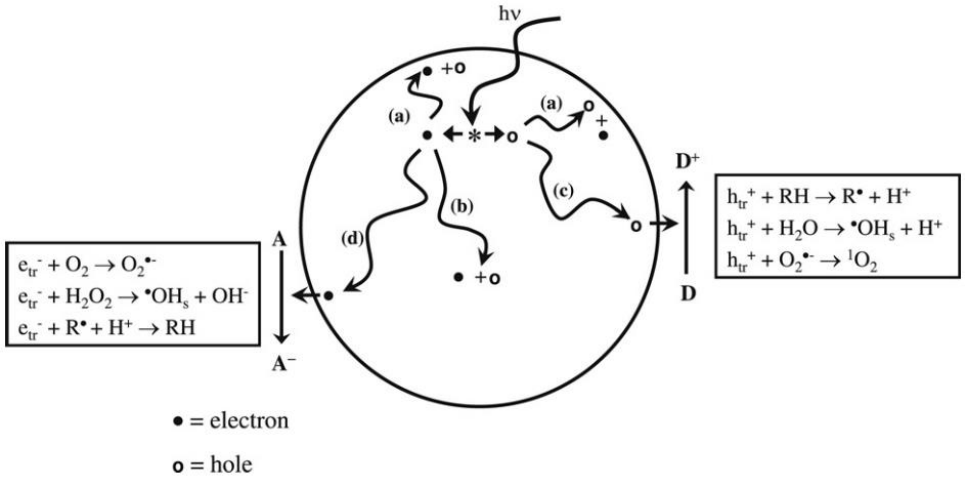

Figure 2.1. Electron-hole pair generation and formation of reactive oxygen species particle after UV excitation.[12]

Semiconductors undergo photoexcitation when photons with energy greater than the material's band gap, E_G (eV), are absorbed at its surface. The incident photon initiates a charge separation when an electron is excited from the valence band to the conduction band forming an electron-hole pair. The photon energy necessary to achieve this reaction is described by

$$E_G = \frac{hc}{\lambda} \qquad (1)$$

where h is Plank's constant, c is the speed of light (m/s), and λ is the wavelength (m).[13] The excited electron can reduce dissolved oxygen to form oxygen radicals, useful for degradation of organic species, while the hole can oxidize water to form hydroxyl radicals, the main reactive species for reducing pollutants or microorganisms.[14] The chemical equations that describe this process of photoactivation and formation of reactive species are described by Figure 2.1. These oxidation and reduction reactions cause

photodegradation that mineralizes organic compounds into CO_2, H_2O, NO_3^-, or other oxides, halide ions, phosphates, etc.[15]

Photocatalysis has rapidly grown in interest since 1972, when Fujishima and Honda demonstrated the water splitting capabilities of photoexcited TiO_2.[16] Since 1972, photocatalysis has been investigated for use in air and water purification, agricultural applications, medical uses, energy conversion such as solar cells, water splitting, and more.[17] Water purification is one of the most commonly researched applications for photocatalysis because, in addition to global health issues, purifying contaminated water remains a persistent issue in a variety of fields. Photocatalysis for water purification has been heavily researched for decontamination of water containing pesticides, bacteria, viruses, dyes, VOCs, and more using bulk and microscale systems.

2.2. Bulk Reactors

Bulk reactor systems use photocatalysis to purify water on a large scale (mL-L volumes) and there are two categories, slurry and immobilized. Slurry reactors consist of semiconductor photocatalyst particles suspended in the target solution, whereas in an immobilized reactor the catalyst is fixed onto a surface. Slurry reactors have received the most attention due to their high surface area advantages over immobilized devices. The suspended particles greatly reduce the mass diffusion distance thus facilitating efficient mass transfer within the system and achieve greater reaction rates compared to immobilized systems. Two main disadvantages decrease the utility of a slurry reactor. The first is that the photocatalyst particles need to be filtered out after the purification has been

completed. Typically, nanoparticles are used in slurry reactors to maximize accessible catalyst surface area, but their small size adds to the complexity of filtering them out. The second problem with slurry reactors is photon utilization, since dense slurries limit the photon penetration depth.[18]

Immobilized reactors are an alternative design that have certain advantages over slurry systems. An immobilized catalyst reactor has highly efficient photon transfer because the catalyst is fixed to a surface, and thus positioned for maximum photon flux. In addition, no filtering is required after the purification process has been completed. The major disadvantages with this system are lower overall catalyst surface area, larger mass diffusion distance, decreased mass transport, and decreased reaction rates compared to a slurry device. For oxidation or reduction reactions to occur, the pollutant must diffuse to the immobilized catalyst surface, so such systems will employ some form of mixing or active flow to promote molecular diffusion. Film thickness also contributes to the reaction rate, thicker films, with at least some degree of porosity, will allow greater fluidic accessibility and contribute to improved reaction rates.[19] Several limitations of bulk reactors have hindered their use in commercial and industrial applications. Both categories of bulk reactors suffer from poor oxygenation when there is a large amount of pollutant to be degraded. Oxygen is required to produce powerful reactive oxygen species (ROS) and in large reactors there is a risk of running out of oxygen which would negatively impact the reaction rate. Bubbling oxygen into the reactor has been investigated but adds complexity. The low mass or photon transfer in each bulk reactor system have remained

persistent limitations and research has shifted towards microfluidics to further improve reaction efficiency.[20]

2.3. Microfluidic Reactors

Microfluidic reactors enhance photocatalytic effects by decreasing all dimensions below the mm-scale. This change in length-scale significantly improves the reaction rate compared to bulk reactor systems.[21] The SA:V ratio is dramatically increased, usually by a minimum of two orders of magnitude. Mass and photon transfer are improved as a result of reaction chamber volumes on the order of μL and channel depths between tens to hundreds of microns. Pollutants and photons have a much smaller distance to travel within the system before reaching the immobilized photocatalyst, making it more efficient compared to bulk immobilized systems. Another benefit is a much shorter reaction time. Bulk reactor systems require exposure times on the order of minutes to hours to completely degrade the contaminant, whereas, microreactors have a residence time on the order of seconds to achieve the same result. Precise control can be maintained over the entire system meaning that the residence time, or the time it takes for one molecule of pollutant to pass through the entire device, can be modified via flow rate. Longer residence times increase the amount of time for redox reactions to occur which results in a greater percentage of degradation as the pollutant passes through the system. Short residence times increase the reaction rate because a greater number of pollutant molecules are being degraded per unit time.[22,23]

The major disadvantages of microfluidic reactor technology are throughput, recycled flow, and inefficient mass transfer due to laminar flow. With μL-scale chamber volumes, the flow rates commonly achieved by these devices are on the order of μL/min. Flow rates such as these from a single device would produce impractical volumes of water a day (< 1L). Increasing flow rates to yield higher throughput negatively impacts degradation efficiency so, in some cases, repeatedly cycling water through the device may be required in order to fully degrade pollutants. Finally, even though mass transfer for a microfluidic system is greatly improved over bulk reactors it is still hindered by the immobilized catalyst within the microreactor due to laminar flow.[20] Figure 2.2, from de Sá et al., illustrates an example of the flow regime within the reaction chamber of a microfluidic device. Region A is the area in which UV-based photolytic reactions are the dominating source of pollutant degradation. Region B is the intermediate region which varies in size based on the reaction chamber dimensions. Region C is the solid photocatalyst/liquid interface where photocatalytic redox reactions are the main degradation mechanism.[23] Region B is where, under a laminar flow regime, pollutants can pass through the system unperturbed. If the residence time is sufficiently long, then diffusional transport of the pollutants to either photolytic or photocatalytic regions is more likely; however, this probability decreases as flow rate is increased.

Several solutions to overcome these limitations have been proposed. The most feasible would be to run multiple devices in parallel at their photocatalytically ideal residence time so that a larger throughput can be produced without sacrificing the advantages listed above.[24] Another commonly reported solution is to scale up the

dimensions of the device to sustain larger throughput. This is a viable solution as long as diffusion lengths are not increased too drastically that a loss of sub-mm scale benefits occurs.[25] The device proposed in this document seeks to overcome these limitations by occupying the intermediate region with photocatalyst-coated micropillars. Under ideal circumstances the micropillars create a fixed molecular diffusion distance regardless of depth and allow the microreactor to be scaled-up without suffering severe efficiency loss.

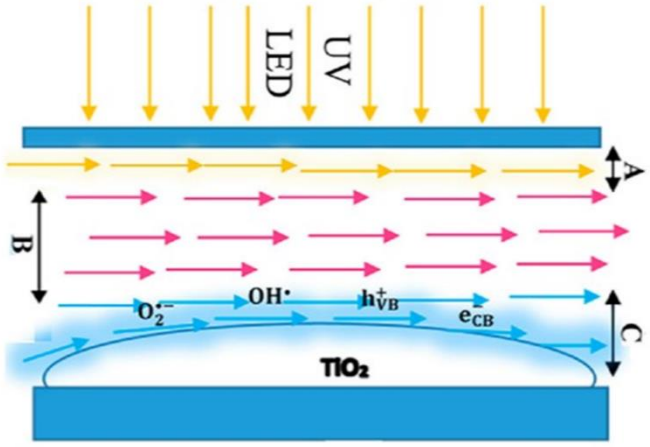

Figure 2.2. Schematic of a photocatalytic chamber. A) Photolysis region; B) Intermediate region; C) TiO_2 Solid/Liquid interface.[23]

2.3.1. Types of Microfluidic Reactors

Numerous PMFR designs have been reported thus far, most falling within four general categories, namely micro-capillary, single channel, multi-channel, and planar channel reactors, examples of which can be seen in Figure 2.3.[20] The micro-capillary reactor has a large SA:V ratio due to the cylindrical reactor chamber geometry; however, uniform catalyst coatings within the narrow lumens can be difficult to achieve, and throughput is also limited. Capillary reactors are also prone to a lower photon flux at the catalyst-liquid interface because many incident photons are absorbed at the catalyst-

support interface. Single and multi-channel microreactors are relatively easy to fabricate out of soft materials such as PDMS. Typically, a glass slide is coated with a photocatalyst and a micro-fabricated PDMS layer is bonded to the surface of the glass creating a water-tight seal.[26] The limitations of single channel reactors are the small cross-sectional area that limits throughput, and the small photoactive area for photon absorption. Multi-channel reactors improve upon the single channel design by increasing the photoactive area with more channels but suffer the same limitations as single-channel systems though to a lesser extent. Of the four categories listed, planar reactors are ideal for maximizing efficiency. A planar device maximizes the accessible photocatalyst area relative to the other designs through the use of a single wide channel.[22] A planar reactor design was used for the high density PMFR concept explored in this document. The wide planar chamber allowed maximum coverage for integrating micropillars into the reaction chamber.

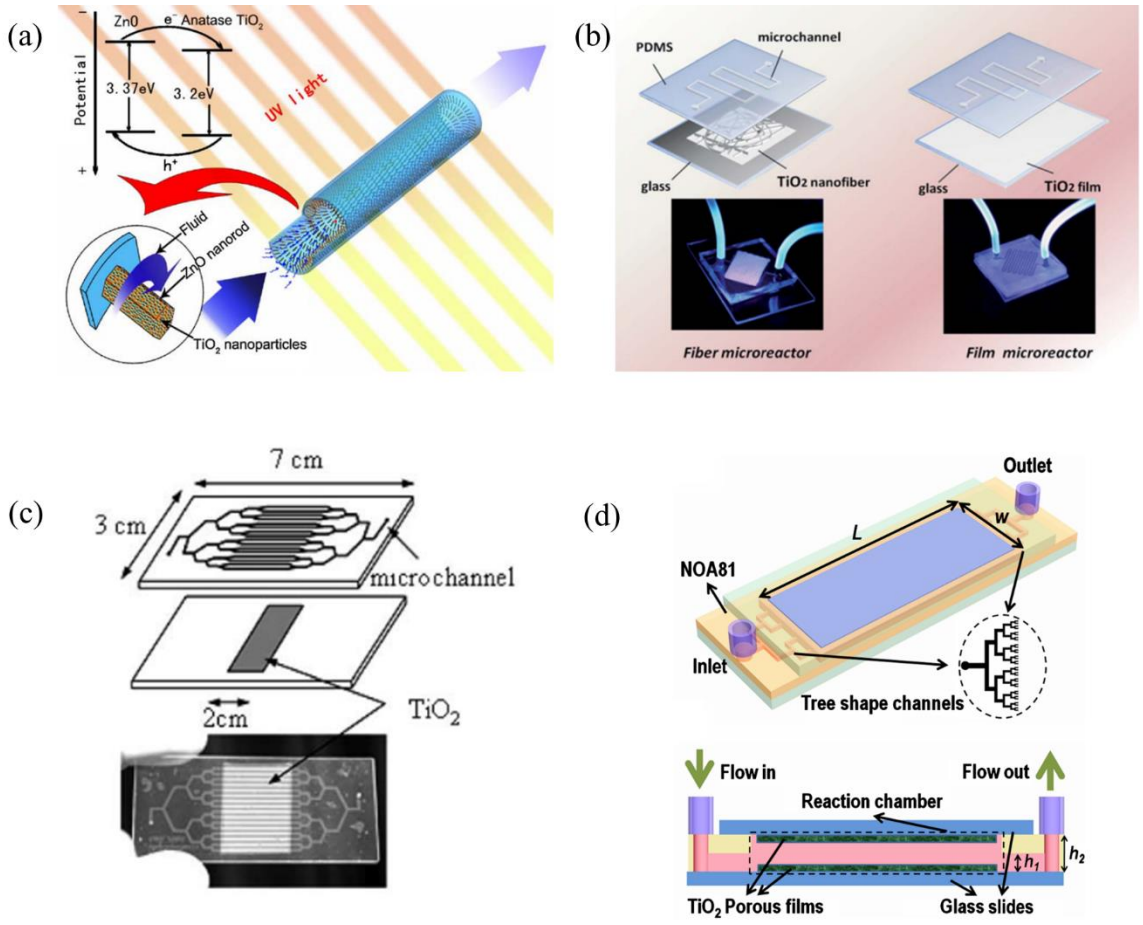

Figure 2.3. Examples of the four categories of microreactors. A) ZnO nanorods and TiO_2 micro-capillary reactor;[27] B) TiO_2 nanofibrous single-channel microreactor;[26] C) TiO_2 multi-channel reactor;[28] D) The schematic and cross-section of a TiO_2 planar reactor[29].

2.4. Titanium Dioxide for Microreactor Applications

TiO_2 is one of the most commonly used photocatalysts for microreactors, due to its availability, excellent anticorrosive and non-toxic properties, ideal band gap for reduction-oxidation reactions, and low cost.[30] TiO_2 has four crystalline structures, amorphous (non-crystalline), anatase, rutile, and brookite. Rutile and anatase have been heavily investigated for photocatalytic applications due to their ideal band gaps.[12] Rutile and anatase TiO_2 are

intrinsically n-type semiconductors, due to oxygen deficiencies, which contribute to TiO_2's classification as a donor-type material.[31] Rutile has a band gap of 3.0 eV and is the most thermodynamically stable, while anatase has a band gap of 3.2 eV and has properties ideal for photocatalytic reactivity.[32] Anatase's larger band gap means that it has a larger valence band energy over rutile which increases redox reaction capabilities. Anatase also has an indirect bandgap which delays recombination of electron-hole pairs, which increases the lifetime of an electron-hole pair, and thus, increases the probability of initiating redox reactions. Rutile is capable of either a direct or indirect bandgap, but there is minimal difference in recombination rates between the two. For these reasons, anatase is considered the preferable crystal structure for photocatalysis.[33]

The photocatalytic nature of titania was first demonstrated by Fujishima and Honda in 1972[16], and since then the material has been heavily investigated for many applications including water splitting[34], gas sensors[35], superhydrophilic surfaces[36], solar cells[37], and water purification[12]. The type of TiO_2 used in these applications varies depending on the intended purpose. TiO_2 has been produced in many morphologies, such as spheres[38], tubes[39,40], wires[41], rods[42], and more[43] in efforts to increase the photocatalytic effect for the desired application. The most widely used form of TiO_2 is Degussa P25 nanoparticles. P25 has been optimized for photocatalysis over decades and generally consists of a combination of 80% anatase and 20% rutile. The more positive conduction band potential of rutile acts as an electron sink for excited electrons from the anatase conduction band, which lowers the recombination rate and increases the lifetime of electron-hole pairs.[44]

For microreactor use, P25 is one of the most commonly used forms of TiO_2 photocatalyst. It is typically mixed into a slurry using a solvent, and then drop-cast onto the floor of the planar channel systems using a sol-gel method.[45] Other forms of TiO_2 have been explored for use within planar channel systems as well. Jayamohan et al. investigated the use of titania nanotube arrays within a microfluidic chamber and found enhanced performance over P25 films.[46] Li et al. explored the use of a dual-film TiO_2 nanorod planar reactor and found that the higher surface area of the nanorods and increased SA:V from the dual-film nearly doubled performance over a conventional single-film microreactor.[47] The main complication that precludes these forms of TiO_2 from use within the proposed microreactor concept is the difficultly in translating the titania onto vertical features within a device. The proposed PMFR concept contains vertical micropillars within the reaction chamber, TiO_2 sol-gel deposition with P25 would not cover vertical features homogeneously and particle aggregation would occur, ultimately resulting in clogging. Anodization of titanium to produce horizontally aligned nanotubes on vertical sidewalls may be a feasible option but it is overly complex compared to the proposed method and it is unclear how nanotubes would form on curved surfaces.[39] Therefore, a different form of TiO_2 that is capable of homogeneous fixation on all exposed, vertical and horizontal, surfaces within a reaction chamber is needed.

2.5. Nanoporous Titania

NPT, also known as nanostructured titania (NST), is a compelling form of TiO_2 for use in microreactor devices. When Ti is submerged into heated hydrogen peroxide (H_2O_2),

chemical reaction produces a nanoporous, hydrated, amorphous TiO_2 film on all exposed Ti surfaces.[48,49] Afterward, the film is annealed to form the desired crystalline state. Peroxide-based oxidation is an efficient, one-step method for depositing NPT onto all surfaces within a microreactor which ensures the device has the largest possible SA:V ratio. The oxidation process produces no hazardous byproducts, and there is minimal risk of contaminating the sample with ions or carbon.[50] The advantages of NPT include: a) conformal coverage of complex geometries, that would be difficult if not impossible to coat using sol-gel or thin-film deposition methods; b) a reticulated, open-framework porosity that provides higher surface area than dense films, and greater fluidic accessibility than nanoparticle-based films; and c) a high degree of scalability and potential for fabrication of robust, large-area photocatalytic devices.

Interest in NPT and its use for photocatalytic applications has grown over the past decade and half since Wu et al. first reported on the low temperature oxidation of titanium with H_2O_2 to form anatase TiO_2. Commercially pure titanium foils were soaked in heated H_2O_2 for 1 hour and annealed in air at 300˚C for 1 hour to form a thin film of crystalline TiO_2 on the Ti substrate.[48] To further improve the photocatalytic activity of NPT, Wu et al. continued to experiment by increasing oxidation times and doping to change the morphology and surface area.[50–52] Zuruzi et al. was one of the first to integrate NST into MEMS applications, and even translated the oxidation procedure onto microfabricated titanium pillars to demonstrate wicking properties.[53–57] The unique oxidation characteristics of the material have been further studied by DeRosa et al. who analyzed the reaction kinetics of the H_2O_2-Ti interactions to theorize that NST forms in two-stages.

Stage 1 is controlled diffusion of Ti molecules away from the substrate and TiO_2 formation occurs at the titanium/hydrated titania layer. Stage 2's mechanism is diffusion of the H_2O_2 molecules through the titania to the boundary layer of unreacted Ti and hydrated titania.[49] Other notable NST studies include a comparison between NST and other titania thin films through organic dye degradation.[58] Ao et al. experimented with the titania morphology and degradation efficiency by adding various inorganic salts and solvents to the H_2O_2 oxidation process.[59,60] To the author's knowledge NPT, or NST, has not yet been tested within a microfluidic reactor and has only been investigated for water purification in an immobilized bulk reactor system. The advantages listed above make NPT an ideal material for use within a high-density microfluidic reactor. The surface area enhancements and its unique oxidation characteristics can yield significant performance improvements when applied to micropillar scaffolding. For these reasons, NPT was selected as the photocatalyst for this study.

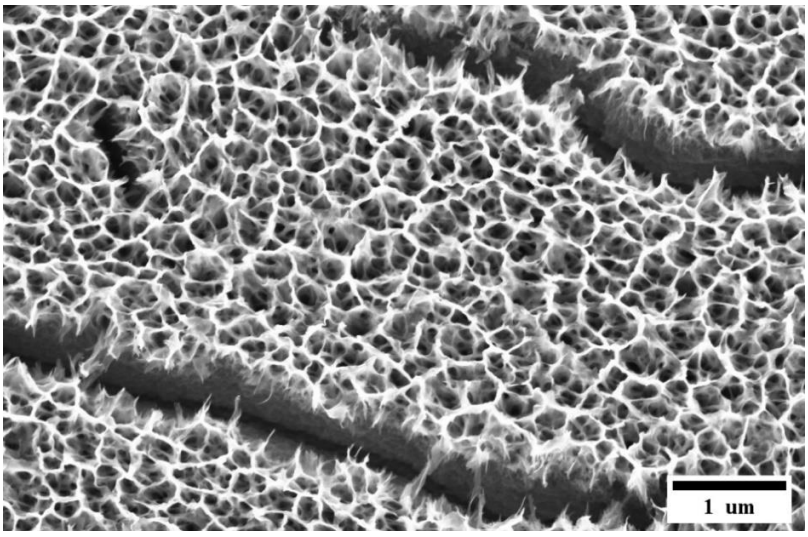

Figure 2.4. NPT oxidized onto a flat Ti substrate. The SEM micrograph shows the variations in morphology. NPT has large pores that decrease in size the closer they are to the Ti-NPT interface. Large cracks are common in films oxidized over several hours.

3 TITANIUM MICROREACTOR FABRICATION METHODS

3.1. Materials for Photocatalytic Reactors

Microfabrication of Ti is a relatively new method of applying techniques developed for traditional silicon (Si) semiconductors to the development of Ti MEMS. Ti, being a metal, has mechanical properties that make it a compelling alternative to brittle Si. Ti is ductile, meaning that microfabricated structures are more likely to bend than break under load, this is especially advantageous for devices such as microneedles[61]. The native oxide layer that forms on the surface of Ti when exposed to oxygen in the ambient air makes the material biocompatible and corrosion resistant; many dental and orthopedic implants are Ti or a Ti alloy.[62] Ti also has a high strength-to-weight ratio making it an ideal material for use in aerospace applications.[63] In regards to PMFRs, microfabrication of Si or Ti is required in order to achieve the desired feature size of the micropillar array, and would be impossible to implement in traditional soft materials, such as PDMS, commonly used in planar reactors. The desired feature size ($\geq$ 15 μm) is easily obtainable in Si but NPT would not form natively on Si; instead, a layer of Ti would have to be deposited onto the microstructured Si. This could potentially be achieved by depositing a thin Ti film through methods such as sputter coating, but the densely packed micropillar arrays in the PMFR concept would likely limit homogeneous deposition of the Ti. Therefore, the most straightforward method is to use bulk Ti as the substrate and microfabricate the reactor into the Ti itself.

3.3. Patterning the Substrate

Microfabrication of titanium is achieved via a top-down manufacturing process that transfers a 2D pattern from a photomask into the Ti substrate. The steps involved simply consist of additive material steps and selective removal of material steps. Physically and chemically reactive etching procedures are applied at various stages to remove material and protective layers called masks are used to prevent etching in predetermined areas of the substrate. To achieve high-aspect ratio features and depths up to 150 µm (deepest reaction chamber depth targeted for this study) a hard mask must be deposited onto the bulk Ti substrate. This hard mask material is usually an oxide, such as TiO_2 or SiO_2 (on the order of hundreds of nm to several µm thick), because oxides have high selectivity compared to soft masks such as photoresist. Selectivity is the ratio of the substrate etch rate to the mask etch rate. Higher selectivity allows fabrication of anisotropic high-aspect ratio features. Selectivity is typically 30-40:1 for oxide hard masks and only 1-2:1 for photoresist. The most commonly used methods to deposit oxide hard masks are low pressure chemical vapor deposition (LPCVD) and plasma-enhanced chemical vapor deposition (PECVD).[64] PECVD was used to deposit an SiO_2 hard mask for patterning the Ti substrates used to make the PMFR concept devices.

After hard mask deposition, photolithography pattering is applied by spinning photoresist onto the substrate. Photoresist, a light-sensitive organic polymer, has a low selectivity so it is ideal for transferring the photomask pattern into the oxide hard mask. Photoresist is deposited (on the order of several µm thick) onto a substrate using a spin coater bench which uses a vacuum chuck to hold the substrate in place. The vacuum chuck

spins at a programmable speed and time which determines the thickness of the photoresist on the sample. A mask aligner is commonly used to expose photoresist. The photomask is placed between the photoresist and the UV exposure lamp so that regions of the photoresist can be protected from incident photons, which transfer the pattern from the photomask into the resist after exposure and development. When photoresist is exposed to UV light, it either cross-links or degrades. A positive resist weakens when exposed to light, and subsequent development in a base solution washes away the degraded resist leaving the mask pattern. Negative photoresist cross-links during exposure strengthening the resist, and development washes away the unexposed resist, leaving the inverse of the mask pattern in the photoresist. A positive photoresist was used to fabricate the PMFR concept presented in this work.

3.4. ICP Reactive Ion Etching

After patterning the photoresist, the oxide hard mask is dry etched using reactive ion etching (RIE) or inductively coupled plasma RIE (ICP RIE) to transfer the photoresist pattern into the oxide hard mask. Reactive ion etching relies on high energy directional ions to remove material through either chemical reactions forming volatile etch by-products, or through physical ion bombardment. ICP generates a higher density plasma compared to RIE, and is capable of anisotropic etching with high etch rates.[65] Plasma chemistries of C_4F_8, CHF_3, and CF_4 are most commonly used to etch SiO_2 hard masks, because fluorine-based dry etching is highly reactive with SiO_2.[66,67]

3.5. Titanium Deep Reactive Ion Etching

High aspect ratio bulk titanium microfabrication through anisotropic dry etching is a relatively new field established in 2004 by Aimi at al.[68] The metal anisotropic reactive ion etching with oxidation (MARIO) process originated from the cyclic Bosch process used to etch Si. The MARIO process allows free-standing, stress-free, high aspect ratio structures to be etched into Ti substrate.[68] Using a cyclical isotropic etch step, followed by an oxidation step to protect the sidewalls from the next cycle, MARIO etches Ti at a rate of 0.5 μm/min. Similar to the Bosch process, the alternating etch and oxidation steps result in scalloped sidewalls. In 2005, the MARIO process was improved upon to increase etch rates without the need for cyclical process and the oxidation step was removed. This new process called titanium deep reactive ion etching (TIDE), resulted in higher aspect ratio features with smooth vertical sidewalls. Figure 3.1 is a comparison of MEMS devices fabricated using the MARIO and TIDE processes.

The TIDE process uses an ICP plasma source to etch titanium in a single process step. It uses a Cl_2/Ar plasma to achieve etch rates of 2 μm/min, mask selectivity of 40:1 ($Ti:TiO_2$), and has a minimum feature size of 750 nm.[69] The main etching mechanism is the chemical reaction between Ti and Cl^- ions. The Ar increases plasma density and stability, and due to its large size, enhances physical etching through ion bombardment. Since the development of TIDE, further process refinement has been conducted to produce ultrahigh resolution titanium patterning, down to a minimum feature size of 150 nm.[70] Over the past decade TIDE has also been used for Ti MEMS application that demonstrate the versatility and benefits of the material in a variety of fields. For example, TIDE has been

used to: increase vascular endothelial cell adhesion via micropatterned titanium;[71] fabricate the first submicron-patterned titanium stent;[72] etch in-plane fenestrated microneedles for ocular drug delivery;[61] and used to demonstrate the potential of Ti microfluidic channels oxidized with NPT for future photocatalytic reactor applications explored herein.[73] The TIDE process was used to fabricate the micropillar reactors used in this study.

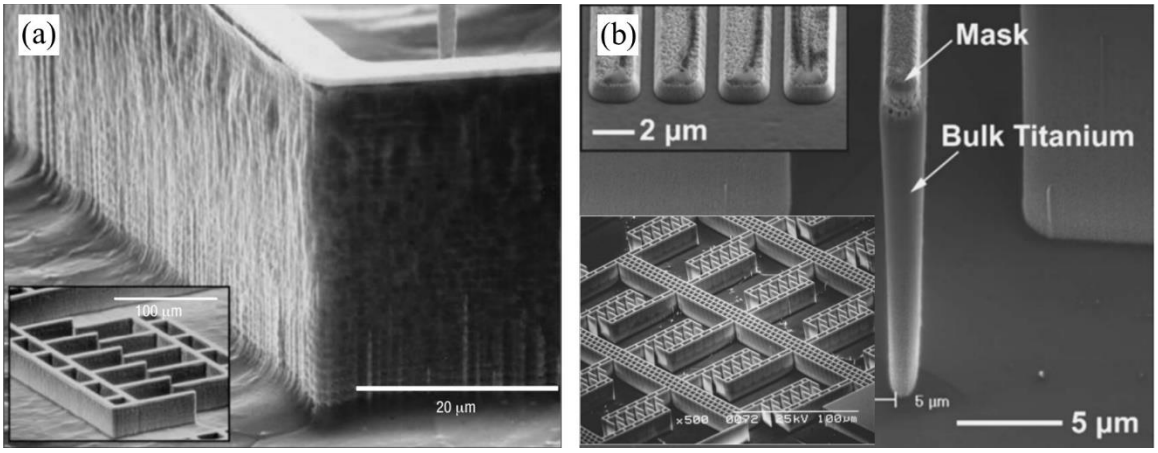

Figure 3.1. Comparison of MEMS devices fabricated using the MARIO and TIDE processes. A) Comb drive actuator fabricated via MARIO process, note the scalloped sidewalls of the larger feature.[68] B) Deep etched feature and comb drive structure etched using the TIDE process, note the smooth vertical sidewalls.[69]

3.6. Passivation Removal

The final step of the fabrication process is passivation removal. Passivation is a build-up of etching by-products, e.g. $Ti_xCl_yO_z$, that deposits onto the vertical sidewalls of the microfabricated features. Passivation is resistant to lateral etching from the plasma and contributes to anisotropy. The passivation must be removed prior to NPT oxidation because chlorine species can contaminate the TiO_2 and lower photocatalytic performance. Wet or dry etching techniques can be used for this procedure; however, fine control must be maintained to ensure that the underlying Ti is minimally affected. For this reason, dry

etching was first attempted, since it offered potential for exploiting gas chemistries that offer high selectivity (e.g., CF_4:O_2), and thus, minimal etching of the underlying Ti. However, the inability to achieve desired etch rates and isotropy with accessible instrumentation motivated the development of an alternate sidewall passivation removal process based on hydrofluoric (HF) acid etching. While HF is known to etch Ti aggressively, the use of dilute solutions (2.3% HF) allowed sufficient control to minimize the impact on device feature fidelity.

4 OPTIMIZATION OF NANOPOROUS TITANIA FOR USE WITHIN MICROREACTORS

4.1. Introduction

Over the past decade, interest in chip-based, photocatalytic microreactors for water treatment applications has significantly increased. Due to their microscale dimensions, microreactors have several advantages over traditional bulk reactor systems, as discussed in Chapter 2. Many publications have reported on the use of planar microreactors for water purification, yet most found that only flow rates <50 µl/min were capable of degrading over 90% of contaminants.[47,74–76] One approach to overcome these limitations is to scale-up device dimensions, however this has been difficult to accomplish without sacrificing advantages that only exist at small length scales.[77] Another approach would be to redesign the traditional systems to accommodate increased flow rates without efficiency loss. This can be achieved by adding catalyst loading mechanisms, such as scaffolding within the reaction chamber to increase surface area for catalyst fixation. If the rate of degradation could be improved, either through device design and/or photocatalyst optimization, then increased flow rates can be achieved.[23]

Photoactivity and film integrity are critical parameters that significantly affect NPT's applicability within microreactors. An effective NPT film has high photo-degradation capability and good adherence to the substrate. However, the oxidation conditions that influence these two quality characteristics have been demonstrated to be inversely proportional. NPT films tuned to improve photocatalytic efficiency often suffer from excessive cracking and delamination. Thicker NPT films possess morphological characteristics that contribute to surface area enhancements and improve the overall photocatalytic properties of the material.[51] However, the severity of cracking and

subsequently, delamination, have been proven to be closely related to film thickness.[57] When considering NPT's use within a microfluidic system in which NPT would be exposed to high flow-induced shear stress, excessive cracking and poor substrate adhesion could ultimately lead to a loss of material and eventual device failure. To mitigate risk of NPT delamination during operation of a microfluidic device, NPT must be optimized not only to maximize photocatalytic efficiency but to minimize crack size as well.

Herein, we have conducted a Taguchi DOE study with grey relational analysis (GRA) to optimize NPT for use within microfluidic reactors based upon two responses. The Taguchi method is ideal compared to other DOE methods, such as factorial analysis, because a large amount of information can be obtained with a relatively limited number of samples. Although Taguchi-based DOE has been previously reported for optimizing the synthesis of other types of TiO_2 photocatalysts, to the authors' knowledge, it has never been applied for the optimization of peroxide-based growth of compact NPT films.[78–82] In this study, NPT was optimized based upon two responses, each with different units, namely maximizing the reaction rate constant (k) and minimizing average crack size. GRA was used in conjunction with the Taguchi study to effectively normalize and combine each response into a single grade to rank each sample. With a single graded response, the ideal oxidation conditions were found, and a confirmation study was carried out to demonstrate the performance of optimized NPT. Finally, a Ti micropillar array was fabricated and oxidized with the optimized NPT conditions to demonstrate the feasibility of NPT for use within microreactors.

4.2. Materials and Methods

4.2.1. Taguchi Experimental Design

The most easily controllable parameters for NPT oxidation are H_2O_2 concentration, temperature, and oxidation time. Each parameter was divided into three levels representing the minimum, middle, and maximum conditions. The H_2O_2 concentration range (10, 20, 30%) was based on chemical availability and is within the range of concentrations commonly reported by others in the literature.[83] Temperature values (80, 85, 90˚C) were selected based upon results from an earlier study by others, which found that temperatures greater than 90ºC resulted in excessive cracking of the TiO_2 film, and temperatures below 80ºC were too low to produce a film of sufficient thickness.[84] The time parameter (1, 3, 5 hours) was kept to a maximum of five hours to limit NPT film delamination, since samples oxidized for six hours showed signs of excessive delamination.

Using Taguchi DOE, an L9 orthogonal array was constructed producing nine NPT growth conditions (Table 4.1). Mean values of the responses were converted to signal-to-noise (S/N) ratios, which quantify performance based upon the desired optimization outcome and are categorized under three scenarios: larger-is-better, smaller-is-better, or nominal-is-best. This parameter study sought to maximize *k* (larger-is-better) and minimize the average crack size (smaller-is-better). The S/N ratio for a larger-is-better response was calculated using

$$SN_{LiB} = -10\log\left(\frac{1}{n}\right)\sum_{i=1}^{n}\frac{1}{y_{ij}^2} \quad (1)$$

where SN_{LiB} is the S/N ratio for a larger-is-better scenario, n is the number of experimental replicates, and y_{ij} is the experimental result of response $i=1, 2,...n$ and condition $j=1, 2,...k$. A smaller-is-better response was calculated by

$$SN_{SiB} = -10 \log\left(\frac{1}{n}\sum_{i=1}^{n} y_{ij}^2\right) \quad (2)$$

where SN_{SiB} is the S/N ratio for a smaller-is-better scenario.[85]

Sample	A (% H_2O_2)	B (˚C)	C (Hours)
1	10	80	1
2	10	85	3
3	10	90	5
4	20	80	3
5	20	85	5
6	20	90	1
7	30	80	5
8	30	85	1
9	30	90	3

Table 4.1. Taguchi orthogonal array of experimental oxidation conditions, A = H_2O_2 concentration, B = temperature (˚C), C = time (hours)

4.2.2. Nanoporous Titania Sample Preparation

Single-side polished, commercially pure (CP), grade 1 polycrystalline, Ti foil (Tokyo Stainless Grinding Co.) with a thickness of 320 μm was cut into 1x1 in^2 squares and ultrasonically cleaned in acetone, isopropanol, and deionized (DI) water. The Ti samples were acid etched in dilute HF (4.9% HF) for one minute to remove the native oxide layer, and then thoroughly rinsed in a sonicating DI bath for 10 minutes. Directly afterward,

the samples were submerged into a heated H_2O_2 bath to form amorphous NPT. Upon removal from the H_2O_2, the sample was rinsed in DI and annealed in air at 300˚C for 8 hours forming anatase TiO_2 (Thermo Scientific Lindberg Blue M). See Appendix E for a detailed step-by-step process.

4.2.3. Reaction Rate Constant Analysis

The photocatalytic efficiency of each NPT sample was evaluated via bulk reactor-based degradation of methylene blue (MB), an organic dye commonly used as a target pollutant in TiO_2 studies.[14,86-88] The experimental setup is displayed in Figure 4.1. Each NPT sample was suspended in a room temperature, water-jacketed, glass reactor with 50 mL of 5 mg/L MB undergoing continuous stirring. A 1.5 mm thick quartz disk was placed on top of the reactor to prevent evaporation. The reactor was then covered for 30 minutes to allow dark adsorption equilibrium to be achieved on the catalyst surface. Next, a UV lamp (Blak-Ray B-100A 100W, 79 mW/cm^2) with a wavelength of 365 nm was positioned 1 inch above the sample and used to expose the NPT to UV light for two hours. MB concentration was measured every 30 minutes using a UV-Visible spectrometer (Evolution 60, Thermo Scientific) at a fixed wavelength of 665 nm, the absorption wavelength of MB. Samples for each of the nine growth conditions were produced and tested in triplicate, and polished titanium was used as a control. The reaction rate constant, *k*, was calculated using the Langmuir-Hinshelwood model for pseudo-first-order reactions.[89,90] The negative natural log of the post-degradation MB concentration normalized by the initial

concentration was plotted against time; *k* was determined by the slope of the linear fit for each sample and is described by

$$k = -\frac{ln\left(\frac{C}{C_o}\right)}{t} \quad (3)$$

where *C* is the post-degradation MB concentration and C_o is the initial (post-adsorption) MB concertation, *t* is the residence time in minutes.[25]

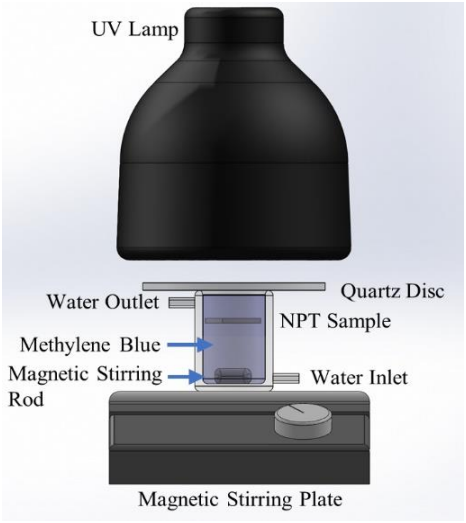

Figure 4.1. NPT bulk reactor experimental setup for degradation of methylene blue.

4.2.4. Crack Size Analysis

To quantitatively measure the morphological changes between the nine NPT growth conditions, the average crack size across the films was measured using scanning electron microscopy (SEM, Leo Supra 55) and image segmentation. Each sample was imaged at four locations using identical SEM parameters, and high-resolution images were captured to maximize the pixels-per-inch (PPI) for use in the segmentation process. Using the trainable WEKA segmentation plugin for ImageJ, part of the imaging suite Fiji (National Institute of Health), the images were binarized to highlight only the cracks in the

NPT and filter the pores and nanowires into the background.[91,92] The pixels highlighted within a crack were counted and averaged across each image to measure the change in crack size between samples.

4.2.5. Grey Relational Analysis

GRA is a multi-step process that mathematically transforms the S/N ratios of each response into a single set of unitless grades between 0 to 1.[93] These grades were used to rank the performance of each of the nine growth conditions found in Table 4.1. The S/N ratios were normalized based on the maximum and minimum S/N ratio in the dataset of each response. S/N ratios were always a larger-is-better scenario, and normalization of each response was performed using

$$x_{ij} = \frac{SN_{ij} - Min_{ij}}{Max_{ij} - Min_{ij}} \tag{4}$$

where x_{ij} is the normalized data for condition $j=1,2\ldots9$ of response $i=1,2$, Min_{ij} is the minimum condition j of the S/N dataset for response i, and Max_{ij} is the maximum condition j of the S/N dataset for response i. The grey relational coefficient compares the normalized dataset x_{ij} to the reference or ideal outcome (x_{0j} = 1), and was calculated for each response using

$$GRC = \frac{\Delta_{min} + \zeta\Delta_{max}}{\Delta_{ij} + \zeta\Delta_{max}} \tag{5}$$

where *GRC* is the grey relational coefficient, $\Delta_{ij} = |x_{0j} - x_{ij}|$, $\Delta_{min} = Min\{\Delta_{ij}\} = 0$, $\Delta_{max} = Max\{\Delta_{ij}\} = 1$, and ζ is the distinguishing coefficient. The distinguishing coefficient has a range of 0 to 1 and was set to 0.5, which is common when the responses are equally weighted.[94] Finally, the grey relational grade was found using

$$G = \sum_{i=1}^{n} w_i GRC \tag{6}$$

where *G* is the grey relational grade ($0 \leq G \leq 1$) and w_i is the weight of response *i*.[85,95] The weights were kept equal at 0.5 each for *k* and crack size. The result was a single set of grades that equally prioritized maximizing *k* and minimizing crack size. A response table was generated based upon the average grade of each level for the three parameters, and the levels with the highest average grade of each parameter produced the optimized conditions for NPT growth.

4.2.6. Analysis of Variance and Confirmation Test

Analysis of variance (ANOVA) was conducted on the results of the Taguchi study to determine the significance of effect that each parameter had on the grey relational grade. The predicted grade and confidence interval of the optimized conditions were calculated and used as a target for experimental performance. The *k* value and crack size were found using the same analysis methods as earlier. The experimental grey relational grade was calculated and used to rank the optimized NPT against the other nine growth conditions.

4.2.7. Feasibility Study

A 1x1 inch^2 micropillar array was fabricated on a 100 mm diameter Ti wafer using the TIDE process discussed in Chapter 3. The micropillars had a target diameter of 20 μm (post-fabricated diameter of 15 μm), with a 40 μm pitch, and were etched to a depth of 100 μm. During anisotropic etching, a passivation layer formed on the sidewalls of the micropillars, which can impede growth of NPT. In such cases, it was removed using a dilute HF etch. Lastly, the patterned substrate was submerged in heated H_2O_2 at the optimized conditions to form NPT on the micropillar scaffolding. SEM was used to verify the level of film adhesion and uniformity of coverage.

4.3. Results and Discussion

4.3.1 Photocatalytic Performance of NPT

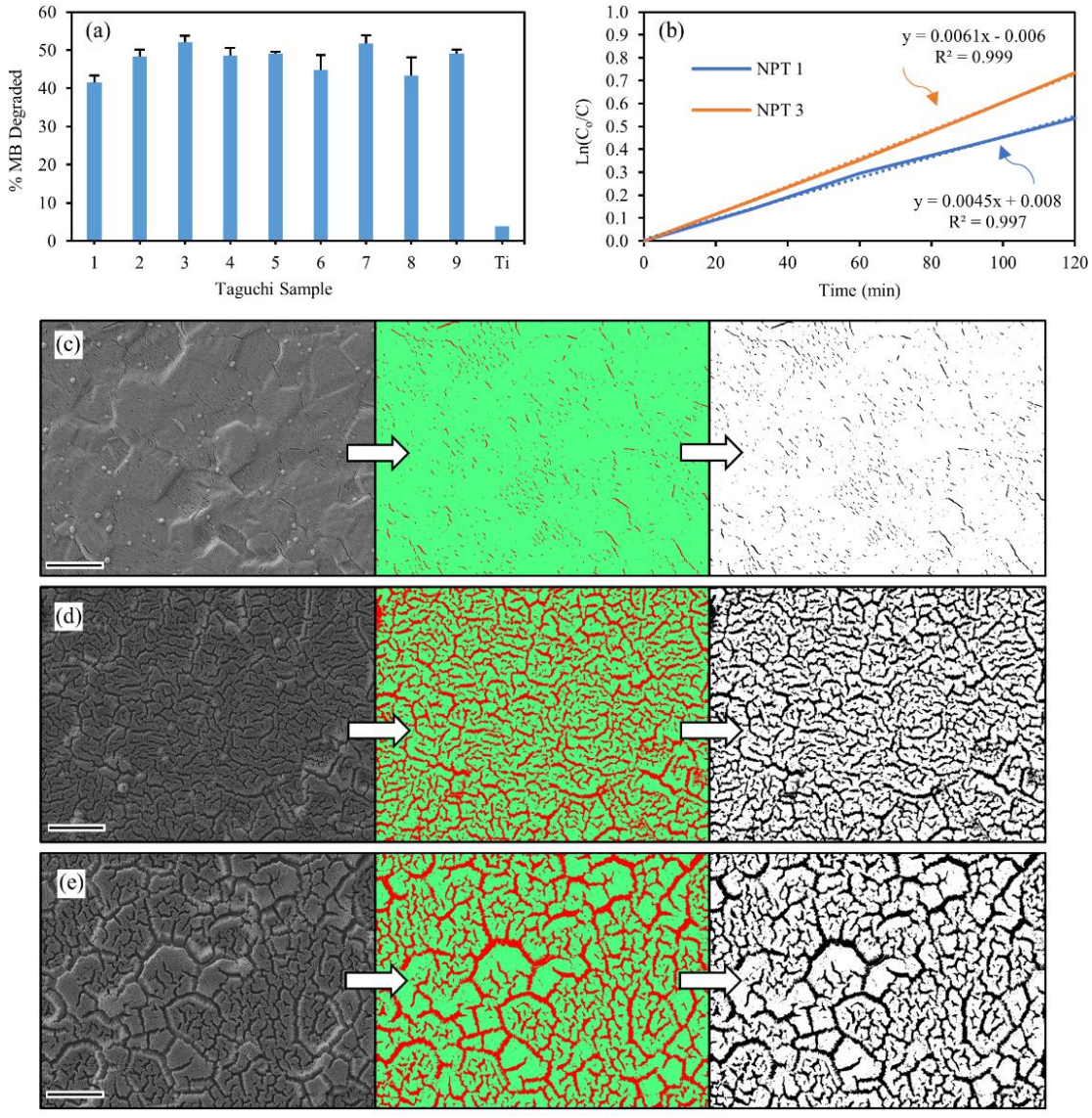

Figure 4.2. a) Percentage of MB degraded after 2 hours of NPT exposure to UV light. b) Plot of first-order reaction kinetics of MB degradation for best and worst performing samples; the slope is the reaction rate constant. c-d) process for quantifying crack size in NPT samples (NPT 1, 2, 3 shown respectively); *left to right:* SEM image, WEKA segmentation, and analysis of object size (black objects are cracks). Scale bar = 20 µm. Data in (a) = mean + standard deviation (n = 3); data in (b) = mean (n=3)

Response Table for S/N *k*					
	Response Table (S/N value)			Delta	Rank
Parameter	*Level 1*	*Level 2*	*Level 3*		
Conc. H2O2	-45.474	-45.475	**-45.283**	0.192	3
Temp	-45.522	-45.535	**-45.175**	0.359	2
Time	-46.502	-45.141	**-44.589**	**1.913**	1

Table 4.2. Response table for reaction rate constant, *k*. Response table of signal-to-noise ratios of only the reaction rate constant. Delta indicates the difference between the smallest and largest level in each parameter, therefore time had the largest effect. Bold indicates the ideal sample conditions for maximizing the reaction rate constant. S/N ratio values closer to zero are better.

Response Table for S/N Crack Size					
	Response Table (S/N value)			Delta	Rank
Parameter	*Level 1*	*Level 2*	*Level 3*		
Conc. H2O2	**-57.494**	-58.100	-58.321	0.827	3
Temp	**-55.990**	-59.443	-58.483	3.453	2
Time	**-49.641**	-61.781	-62.494	**12.853**	1

Table 4.3. Response table for crack size. Response table of signal-to-noise ratios of average crack size. Time yielded the greatest effect on the outcome. The ideal sample to minimize the crack size is level 1 for each parameter. This is confirmed by the performance of NPT 1. S/N ratios closer to zero are better.

The mean percentages of MB degraded for all nine NPT growth conditions after two hours of UV exposure is shown in Figure 4.2a. The negligible MB degradation observed for the polished Ti control indicated that there was minimal UV-based photolysis of the MB, as would be expected, given the use of relatively long-wavelength UV for these studies. NPT 3 (10%, 90˚C, 5 h) produced the highest performance, eliminating 52.98 $\pm$ 1.79%, while NPT 1 (10%, 80˚C, 1 h) had the lowest performance, degrading 41.42 $\pm$ 1.91% of the MB. The *k* values were calculated by the slope of the pseudo-first order reaction found in figure 4.2b. NPT 1 (*k* value of 0.0045 min^{-1}) and NPT 3 (*k* value of 0.0061 min^{-1}) are the only samples represented in figure 4.2b, however all samples fit the reaction

kinetics model with R^2 values over 0.997. The complete experimental results can be found in table 4.4 (see Appendix B for XRD of NPT, and Appendix C for a comparison study between NPT and P25).

Response table 4.2, shows the average S/N ratio for each level of the three parameters, and was used to determine the effect of each parameter on *k*. Oxidation time proved to have the largest influence on *k*. This was also observed in the experimental results, as three of the four samples with the largest *k*, NPT 3 (10%, 90˚C, 5 h), NPT 7 (30%, 80˚C, 5 h), and NPT 5 (20%, 85˚C, 5 h) were each oxidized for five hours. Table 4.2 also shows that level 3 of each parameter had largest average S/N ratios, thus indicating that NPT photocatalytic performance improved with more aggressive growth conditions.

The performance improvement with respect to increasing oxidation conditions can be largely attributed to the increase in film thickness which is primarily reliant on oxidation time. Studies have shown that longer oxidation times led to increased reaction rates as a result of thicker films, larger pores, and taller microstructure.[58,96] Each of these morphological changes benefits the photocatalytic efficiency of the material either through improvements in surface area, allowing more pollutant adsorption sites, or via greater fluidic accessibility. Optimization based purely on maximizing the reaction rate constant would demand that NPT growth be conducted at the highest level for each parameter. However, to decrease complications of cracking and delamination commonly associated with thicker films, lower oxidation conditions were investigated.

4.3.2. NPT Crack Size

NPT SEM images and the steps for image segmentation and crack size measurement are depicted in Figure 4.2c-d. NPT 3 (10%, 90˚C, 5 h) yielded the largest cracks measuring, on average, 2071 ± 184 pixels; while NPT 1 (10%, 80˚C, 1 h) had the smallest crack size of 135 ± 5 pixels. Response table 4.3 shows that time had the greatest effect on cracking. NPT cracking is largely a result of two factors 1) compressive stresses due to thermal mismatch between the growing oxide layer and the Ti substrate, and 2) film shrinkage due to dehydration during annealing.[53] NPT films oxidized at higher levels likely produced much thicker films, resulting in larger cracks compared to films oxidized at lower levels. Table 4.3 also shows that level 1 of each parameter had the largest S/N ratio and would therefore be the oxidation conditions used to most effectively limit cracking. However, optimization based solely on decreasing crack size would negatively impact photoactivity, as demonstrated by the MB degradation performance of NPT 1 (10%, 80˚C, 1 h), which was oxidized with level 1 conditions. NPT 1 had the smallest crack size but the worst photocatalytic performance. Thus far, we have demonstrated that oxidation conditions that influence *k* and crack size are inversely proportional to each other. Higher level oxidations resulted in improved *k* values, while lower level conditions led to smaller cracks. Therefore, GRA was necessary in order to find oxidation conditions that equally balanced the two quality characteristics.

Sample	A (%)	B (˚C)	C (hours)	%MB Deg	k (min^{-1})	CS (pixels)	S/N *k*	S/N CS	Grade	Rank
1	10	80	1	41.42 ± 1.91	0.0045	135 ± 5	-46.936	-42.604	0.667	1
2	10	85	3	48.22 ± 1.95	0.0055	1505 ± 81	-45.193	-63.553	0.478	7
3	10	90	5	51.98 ± 1.79	0.0061	2072 ± 184	-44.293	-66.326	0.667	1
4	20	80	3	48.61 ± 2.01	0.0055	1536 ± 99	-45.193	-63.725	0.477	8
5	20	85	5	49.07 ± 0.50	0.0056	946 ± 62	-45.036	-59.515	0.526	5
6	20	90	1	44.78 ± 3.90	0.0049	357 ± 26	-46.196	-51.059	0.497	6
7	30	80	5	51.68 ± 2.20	0.0060	1208 ± 74	-44.437	-61.640	0.643	3
8	30	85	1	43.40 ± 4.71	0.0048	579 ± 41.6	-46.375	-55.260	0.436	9
9	30	90	3	49.20 ± 0.94	0.0056	800 ± 48	-45.036	-58.064	0.537	4

Table 4.4. Experimental results for each growth condition, signal-to-noise transformations, grey relational grade, and performance ranking; A = H_2O_2 concentration, B = temperature (˚C), C = time (hour), CS = crack size

4.3.3. Grey Relational Analysis

GRA was applied to the results of the MB degradation and crack size analysis studies to determine the optimal NPT growth conditions. S/N ratios were calculated using equation 1 for *k*, with a larger-is-better scenario, and equation 2 for crack size, with a smaller-is-better scenario. The grey relational grade, which was calculated from the S/N ratios using equations 4, 5, and 6, is displayed in Table 4.4, along with the respective rankings. NPT 1 and NPT 3 both scored identical grades of 0.667 and tied for first rank. This was a result of the normalization process and the balanced performance between the two samples. NPT 1 had the smallest *k* and the smallest cracks and therefore represented the minimum and maximum S/N ratios for normalizing the two responses. Whereas NPT 3 had the opposite performance, exhibiting the largest *k* and the largest cracks, equating to the maximum and minimum values used in the respective responses.

The new optimized oxidation conditions were found using Table 4.5, which shows the average grade of samples oxidized at each level of the three parameters. The optimal oxidation conditions are level 1 concentration with a grade of 0.604, level 1 temperature at 0.596, and level 3 time at 0.612 (10%, 80˚C, 5 hours). Temperature and time had nearly the same effect on the grade with a max-min delta of 0.115 and 0.114 respectively, while concentration had the smallest influence with a delta of 0.104. It has been previously demonstrated that longer oxidation time produces thicker films and larger pores[57], while concentration and temperature have a more direct effect on the rate of NPT growth. Greater densities of H_2O_2 molecules yield increased oxidation rates and higher temperatures increase the rate of NPT growth and produce taller nanostructures.[84] Therefore it is possible that temperature and time, which had similar effects on the outcome, had an inversely proportional relationship. Within the optimized process a level 1 oxidation temperature may have slowed the reaction rate enough to balance a level 3 oxidation time to produce a film with the desired characteristics.

In addition, samples oxidized with level 2 of any parameter had the lowest grades compared to samples produced at the other levels. This was likely because the two responses were inversely related to each other. Level 1 oxidations did the most to minimize crack size, while level 3 oxidations had the greatest effect on increasing *k.* It is possible that level 2 oxidations may not have significantly contributed to *k* or crack size, and instead led to samples with middling performance in each response. This explanation was further demonstrated by the fact that the average grade for each level 2 parameter was 0.500 or close to it, falling in the middle of the range for the grey relational grade.

Parameter	Level 1	Level 2	Level 3	Effect
Conc. H2O2	0.604*	0.500	0.539	0.104
Temp	0.596*	0.480	0.567	0.115
Time	0.533	0.498	0.612*	0.114

Table 4.5. Response table of the grey relational grade showing the effect of each parameter; * indicates levels for optimized NPT

4.3.4. Analysis of Variance and Predicted Performance

ANOVA was conducted to determine the significance of each parameter on the outcome. The sum of squares for each parameter and the sum of squares total were calculated using the grey relational grade and the following equations,

$$SS_A = N[(\overline{A_1} - G_m)^2 + (\overline{A_2} - G_m)^2 + (\overline{A_3} - G_m)^2] \quad (7)$$

where SS_A is the sum of squares for parameter A, N is the total number of experiments in the orthogonal array, $\overline{A_1}$, $\overline{A_2}$, and $\overline{A_3}$ are the average grades for level 1, 2, and 3 samples of parameter A found in table 4.5, and G_m is the average grade for all experiments. Sum of squares total, SS_T, was calculated using

$$SS_T = \sum_{j=1}^{N} \left(G_j - G_m\right)^2 \quad (8)$$

where G_j is the grade of the j^{th} experiment.[97] The Fisher's F-test was used to evaluate the significance that each parameter had on the outcome and was calculated by dividing the mean square of each parameter by the mean square error. Table 4.6 shows the results of the ANOVA analysis calculated using a commercial statistical software package (Minitab® 18). All three F-ratios were greater than 4.0, thus indicating that each parameter was significant and contributed to the outcome. If the F-ratio was small, then that parameter

would not need to be included in optimization, therefore, the optimized condition was considered valid.[98] The percent contributions of each parameter emulated the results from response table 4.5, in that temperature and oxidation time had similar effects, while H_2O_2 concentration had a smaller effect.

Source	DF	SS	MS	F-ratio	% Cont.
Conc.	2	0.0165	0.0083	4.070	26.3
Temp	2	0.0217	0.0108	5.350	34.5
Time	2	0.0206	0.0103	5.070	32.7
Error	2	0.0041	0.0020		6.5
Total	8	0.0628			

Table 4.6. ANOVA Results for Grey Relational Grade

4.3.5. Optimized Confirmation Results

The grey relational grade of the optimized sample (10%, 80˚C, 5 hours) was predicted using

$$G_p = G_m + \sum_{i=1}^{q} (G_i - G_m) \quad (9)$$

where G_p is the predicted grey relational grade for the optimized sample, q is the number of significant parameters, and G_i is the average grade for optimized conditions.[97] The predicted grey relational grade was 0.716, with a 95% confidence interval of $0.546 \leq G \leq 0.887$. Experimental measurements showed that the optimized NPT degraded 51.56 $\pm$ 2.00% of the MB with a k of 0.0060 min^{-1} and ranked third among the nine original growth conditions, degrading only 0.42% and 0.12% less MB than NPT 3 and NPT 7. The crack size was measured to be an average of 1700 $\pm$ 174 pixels, 372 pixels smaller than NPT 3

and 164 pixels larger than NPT 4, thus ranking ninth overall. The optimized NPT achieved a grade of 0.628, falling within the confidence interval, but below the predicted grade, and ranked fourth overall. However, these optimized conditions produced promising results, yielding a *k* value only 1.6% below the best performing sample and 17.9% smaller cracks than the recorded maximum.

The large crack size of the confirmation sample was the main factor that contributed to a lower grade. Crack size generally increased as oxidation conditions were increased, but a degree of variability was observed. This variability could have been attributed to a statistical distribution of pits that formed in the stage 1 oxide layer.[60] During the oxidation process pitting can occur in areas that have not reached the critical oxide thickness to begin forming stage 2 oxide, and this would result in a recess that ultimately formed cracks.[60] It is possible that the distribution and size of the initial pitting ultimately translated to unexpected variations in crack size between samples. There were instances where several more aggressively oxidized samples had smaller cracks than expected. For instance, NPT 5 (20%, 85˚C, 5 hours) had an average crack size 45% smaller than the confirmation sample but was fabricated at higher levels of concentration and temperature. The predicted grade did not fully account for the crack size variations from sample to sample, but served as a target for expected performance. Because the confirmation did fall within the confidence interval these optimized conditions can be used for future studies to reliably achieve a result that equally balances reaction rate constant and film quality.

4.3.6. Feasibility Study

Figure 4.3 shows the titanium micropillar array before and after NPT oxidation with the optimized growth conditions. NPT was able to fully oxidize the micropillar array without delaminating from the curved surfaces. Cracking was present in the film but did not appear to limit uniformity of coverage and there were no signs of delamination, which is an indication of good film quality and adhesion. NPT oxidation onto Ti micropillars had been previously investigated for applications other than water purification, but at much milder growth conditions.[57] The addition of micropillars markedly improved the SA:V ratio, increasing the area for catalyst loading by over 6.7x compared to a flat sample of the same footprint. When applied to a microreactor, expected additional benefits would include reduced diffusion distance and increased photon utilization and light trapping, thus translating to potential for significant improvements in photocatalytic efficiency.

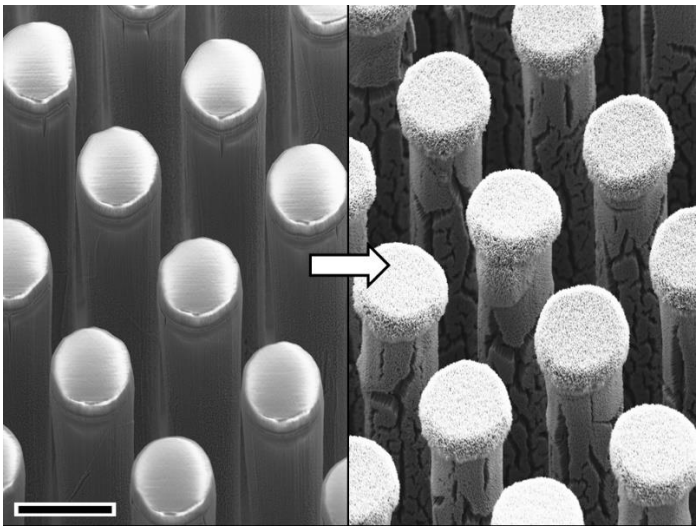

Figure 4.3. *Left:* SEM of Ti micropillars fabricated using deep reactive ion etching. *Right:* Micropillars after oxidation with optimized NPT growth conditions. Scale bar = 20 μm.

4.4. Conclusions

A Taguchi-based DOE study was conducted using GRA for optimization of NPT growth conditions based on maximizing *k* and minimizing crack size. The results showed that more aggressive oxidation conditions were ideal for increasing *k*, but milder conditions were more suitable for decreasing crack size. GRA predicted that the optimal NPT oxidation parameters would be the lowest H_2O_2 concentration and oxidation temperature, and the longest oxidation time (10% H_2O_2, 80˚C, 5 hours). ANOVA verified that each parameter significantly contributed to the outcome of the quality characteristics and validated the optimized conditions. The optimized sample was tested in a confirmation study and ranked fourth overall. The confirmation grade fell below the predicted grade, but was within the confidence interval. Although the confirmation sample did not exceed the overall performance of original nine growth conditions, we believe these NPT conditions represent a reliable process for use in future studies. When the optimized conditions were applied to the growth of NPT within a titanium micropillar array, there were no observed signs of delamination, and the film appeared to have good adhesion to the substrate. In Chapter 5, these optimized conditions were applied to the growth of NPT within Ti micropillar-based microreactor devices, and the impact thereof on photocatalytic performance was evaluated.

5 TITANIUM MICROREACTOR CONCEPT FOR WATER PURFICATION

5.1. Introduction

As discussed earlier, we have proposed the use of photocatalytic microreactors as a potential solution for improving the reliability and performance of water recovery systems (WRS) intended for use in future manned deep space missions. Chapter 1 touched upon the limitations of the thermal catalytic oxidation reactor used for VOC degradation, an essential, but chronically problematic component of the current WRS. The high temperatures and pressures required to operate the catalytic reactor lead to premature seal and pump failure, thus requiring replacement on timescales that are unlikely to be compatible with future mission durations. Photocatalytic microreactors, which operate at standard temperature and pressure, may provide opportunity for mitigating such issues, and also significantly reducing overall system size and weight (e.g., by allowing use of smaller pumps, lighter piping and hardware, as well as elimination of heaters, heat exchangers, thermal insulation, etc.). Finally, by exploiting the UV-rich environment of space, photocatalytic microreactors may also offer potential for reducing power consumption considerably (e.g., by eliminating need for heaters and high-pressure pumps).

Since the catalytic reactor in the WRS is housed in a cylinder 3.5 cm in diameter and 18.1 cm in length, replacement devices with comparable dimensions would be preferred, to maximize compatibility with the existing system architecture.[7] Consequently, this places emphasis on not only increasing device efficiency and throughput, but also doing so in as a space-efficient manner as possible. As will be detailed in this chapter, our novel microfluidic reactor design shows promise in this regard.

Due to differences in photocatalytic microreactor dimensions, design, catalyst, light source, and experimental conditions it can be difficult to compare one device against another. There is no universally accepted procedure for analyzing microreactors, however there are performance metrics that are commonly reported, such as change in pollutant concentration and reaction rate constant. These two metrics are measured against residence time, the amount of time it takes the contaminant to pass through the entire device, which is a factor of chamber volume and flow rate. Constant residence time allows dissimilar devices to be measured on the same scale; however other factors, such as contaminant concentration, can have a significant impact on the outcome. There are many forms of organic dyes, VOCs, and molecules that have been used as contaminants, each with different degradation mechanics, and there are rarely standardized operating conditions. While MB is a commonly used model contaminant for characterizing microreactor performance, its utility for directly quantifying photocatalytic performance is limited, since it degrades into various byproducts that can block catalyst surface sites, and/or consume additional hydroxyl radicals. However, it was nevertheless chosen for use in this study, since it allowed for more direct comparison to the widest body of work in the microreactor literature.[47,74,76,99]

Herein, we have conducted a study to quantify the effect of micropillars within the reaction chamber of a PMFR device. Titanium micromachining techniques were used to fabricate the two microreactor designs, one with micropillars and one without, otherwise each was identical. Each device was fabricated to three different depths to measure the impact on photocatalytic degradation and to investigate photon-micropillar interaction. To

compare the two devices to those found in literature, we evaluated PMFR performance via four different performance metrics at five residence times for each reactor. By compiling the chamber volumes, flow rates, residence times, degradation ratios and rates from other devices reported in the literature, we were able to directly benchmark the performance of our reactors against the current state-of-the-art.

5.2. Materials and Methods

5.2.1. New Microreactor Concept

Reaction Chamber

The new microreactor concept originates from the traditional chip-based planar reactor design for its optimal use of a single open chamber vs. a multi-channel or single channel system. A micropillar scaffolding array was introduced into the reaction chamber to further increase the SA:V ratio without the need to modify device dimensions. The added complexity of vertical features limits the forms of TiO_2 that can be used within the system (see Chapter 2 for details). Therefore, NPT was used as the photocatalyst due to its ability to oxidize any exposed Ti surface upon exposure to H_2O_2. The DOE-optimized NPT conditions (10%, 80˚C, 5 hours) were incorporated onto the micropillar array for the study. To properly use NPT, the reactor was fabricated out of a bulk Ti wafer so that NPT could be formed directly onto the micropillar array.

The dimensions of the reaction chamber were established to yield a chamber volume consistent to other devices found in the literature. The 2 x 2.048 cm reaction chamber consisted of 512,000 micropillars with a target diameter of 20 µm and a 40 µm pitch (micropillar diameter was measured to be an average of 15 µm after fabrication,

calculations were made using this diameter). Each row of micropillars was offset to increase mixing. The devices were fabricated to three different depths of 50, 100, and 150 μm, with greater depths potentially improving the benefit of the micropillars by increasing the surface area for catalyst fixation by 3.7x, 6.7x, and 9.7x respectively over a flat planar device. In addition to greater surface area, other potential advantages of micropillars include a decreased and fixed mass diffusion distance (max of 6.5 μm vs max of 150 μm for micropillar vs planar devices) resulting in greater mass transfer rates; increased light trapping and photon utilization; and significantly improved reaction rates.

Flow Distribution Network

To minimize the pressure drop across the system we adopted a bifurcating tree-branch design for the flow distribution network at the inlet and outlet.[100] Bifurcating flow distributors begin with a large initial channel from the inlet and double the number of channels at each additional branch, until there are channels spanning the entire reaction chamber entrance. Bifurcating designs are commonly used to slowly decrease the speed of the fluid as it enters the reaction chamber to effectively modulate the pressure between the inlet and outlet and uniformly distribute the flow across the entire reaction chamber. To ensure that the initial channel was not excessively wide, channel width was decreased by a factor of 1.6 between each successive branch following the model established by Vangelooven et al.[100] There were 256 iterations of the smallest branch, each iteration consisted of two openings 20 μm wide in an offset position to the first row of micropillars. Figure 5.1 shows the two microreactor designs compared in this study.

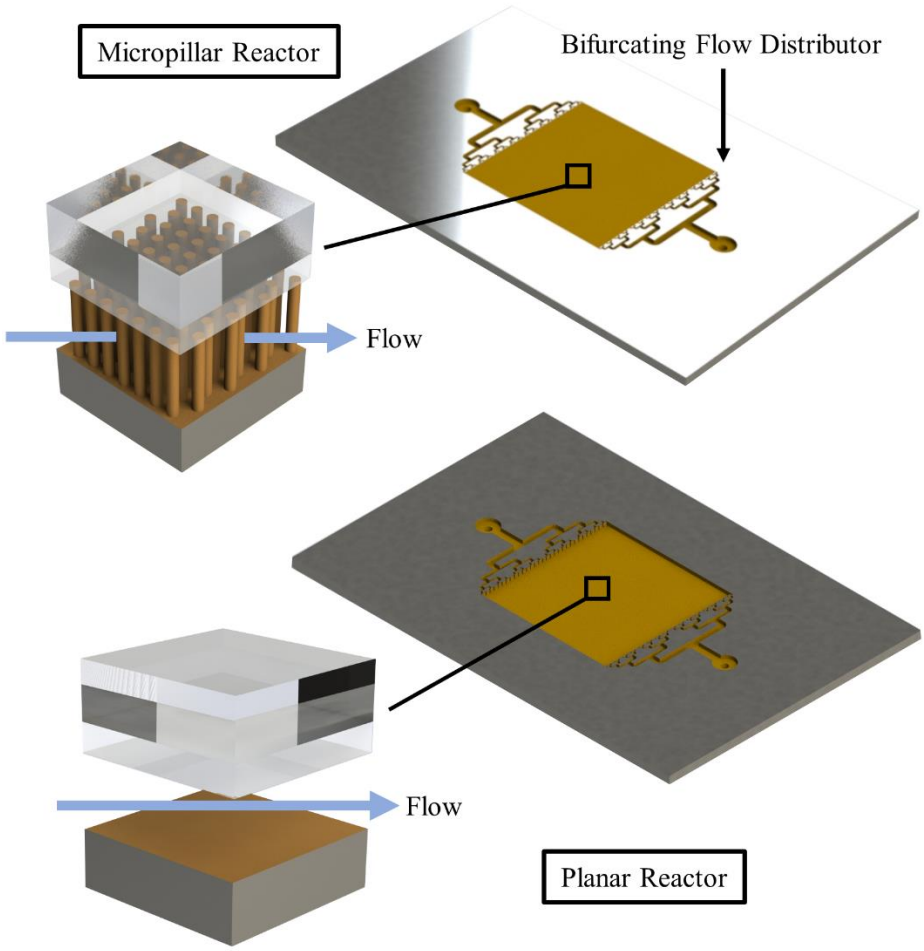

Figure 5.1. *Top*, schematic of micropillar reactor with blown-up image of NPT grown *in situ* on a titanium micropillar core. *Bottom*, planar reactor with blown-up image of chamber.

5.2.2 Microreactor Fabrication

Micropillar and planar reactors were both fabricated using an identical process seen in Figure 5.2. From this point on a micropillar device will be referred to as "MP50" for a 50μm depth reactor and "P50" for a 50 μm depth flat planar device. Grade 1 commercially pure titanium wafers (100 mm) were cleaned using Acetone, Isopropanol, and DI water and placed into a Plasma Enhanced Chemical Vapor Deposition (PECVD) system to deposit 4.2 μm of SiO_2 as a hard mask. The Ti wafers were then mounted onto 100 mm

polycrystalline Si wafers using 3M double-sided thermally conductive tape. The wafers were cleaned with solvents and using a spin bench photoresist was spun onto the Ti wafers to protect the surface during the next step. Each wafer was then diced into two rectangular chips 60 mm x 40 mm using a Disco DAD 321 Automatic Dicing saw with Disco Diamond blades. The photoresist protects the surface of the oxide from potential contamination and damage during the dicing process, while the Si wafer mounted beneath the Ti helps to dress the blade (i.e., reduce buildup of titanium on the blade). Each chip is then ultrasonically cleaned in solvents and DI water to remove the residual photoresist.

Two photomasks were made using the IC Layout Editor L-Edit. These were produced with identical dimensions, the only difference being the micropillars. Following dicing and cleaning, the chips were subjected to photolithographic patterning using the film masks. First, HMDS was spun onto the Ti chips to promote photoresist adhesion. Then, SPR-220-7.0 was spun onto the chips to a thickness of 5.5 μm and exposed using a Karl SUSS MA-6 Mask Aligner. Samples were then developed in AZ 300 MIF developer and pattern quality was evaluated via optical microscopy.

After lithographic patterning, the samples were subjected to SiO_2 plasma etching using an ICP Oxford Cobra Plasmalab System 100 with a plasma chemistry of C_4/F_8 until the lithographic pattern had been transferred to the hard mask. The residual photoresist was then removed through brief ultrasonic agitation in acetone, rinsed in isopropanol, and DI water, and finally, dried on a hotplate at 115˚C. An Oxford Cobra Plasmalab System 100 Metal Trench Etcher was used with a Cl_2/O chemistry to define the planar reactors and a Panasonic E626I ICP System was used with a Cl_2/Ar chemistry to etch the micropillar

reactors. The Oxford system, located at UC Riverside, uses much high ICP source power and higher Cl_2 flow rates compared to the Panasonic system, located at the UC Santa Barbara nanofabrication facility. Efforts were made to develop a process capable of etching micropillar features on the Oxford system but could not be properly refined for use in this study. Therefore, the Oxford system was only used to etch planar devices while the Panasonic system was used to define the micropillar devices. After Ti etching, the samples were submerged in acetone for 72 hours to dissolve the tape and remove the Si backing from the Ti chip. A Dremel tool was used to drill inlet and outlet holes in the Ti chip, 1 mm in diameter, at the origin of each flow distributor.

As mentioned in Chapter 3, a passivation layer forms on vertical surfaces during Ti deep etching to prevent lateral etching from occurring. This passivation must be removed to expose the pure Ti underneath prior to NPT oxidation. This was to ensure that impurities, such as Cl, did not react during NPT oxidation, which could negatively impact the photocatalytic performance. Passivation was removed by subjecting the samples to dilute HF (2.3%) for 40 seconds followed by sonication in a DI water bath for 5 minutes. The reactors were then immediately placed into the heated H_2O_2 solution. All reactors were oxidized under the same optimized conditions from the NPT parameter study found in Chapter 4 (i.e., 10%, 80˚C, & 5 hours). Upon removal from the H_2O_2, samples were rinsed with DI water and placed into a Lindberg Blue M Box Oven and annealed in air at 300˚C for 8 hours. A detailed step-by-step process is described in Appendix D.

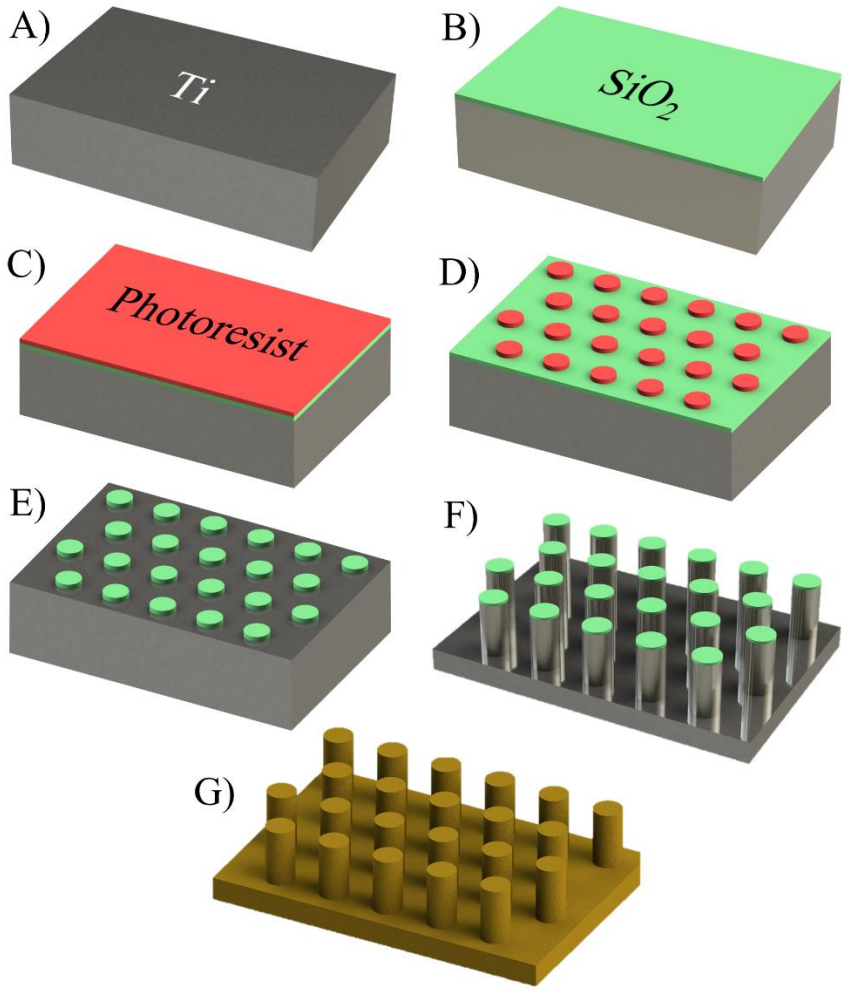

Figure 5.2. Process flow for fabrication of microreactors. A) Bulk titanium wafer; B) SiO_2 deposited onto Ti surface with PECVD; C) Photoresist spun onto sample using Spin Coater; D) Photoresist exposed with mask aligner and developed to reveal mask pattern; E) Photoresist mask pattern transferred into the SiO_2 hard mask using reactive ion etching; F) Mask pattern fully transferred into the Ti via deep reactive ion etching method; G) Directly after passivation removal the device was submerged into H_2O_2 to form NPT.

5.2.3. Photocatalytic Reactor Studies

To quantify the effect of micropillars we investigated the photocatalytic performance of each device at different residence times and conducted a durability evaluation. In order to use the microreactors as a functioning device a fixture set was constructed to enclose the entire system forming a water-tight seal. CAD modeling was

used to design an enclosure that could clamp a glass cover over the open channels to ensure the solution was forced through the device. Several iterations were designed and tested using a 3D-printed ABS plastic, however the plastic proved to be insufficient and fractured under load resulting in leaking. To solve this problem the fixture set was fabricated out of aluminum which successfully produced a water-tight seal on the reactor (see Appendix E for detailed schematics). In addition to the fixture set, other layers were added to ensure a secure fit and reduce the potential for cracking the glass cover. The schematic for the constructed microreactor device is shown in Figure 5.3. The constructed device consisted of the base Aluminum (Al) fixture set, on top of that a 1 mm thick PDMS gasket, followed by the reactor, then a thin 250 μm PDMS sheet bonded to a 1mm thick glass slide, beneath a 1 mm PDMS gasket to distribute load, all beneath the top Al fixture set. Threading was integrated into the holes of the base fixture set and M5 screws were used to tighten all layers together.

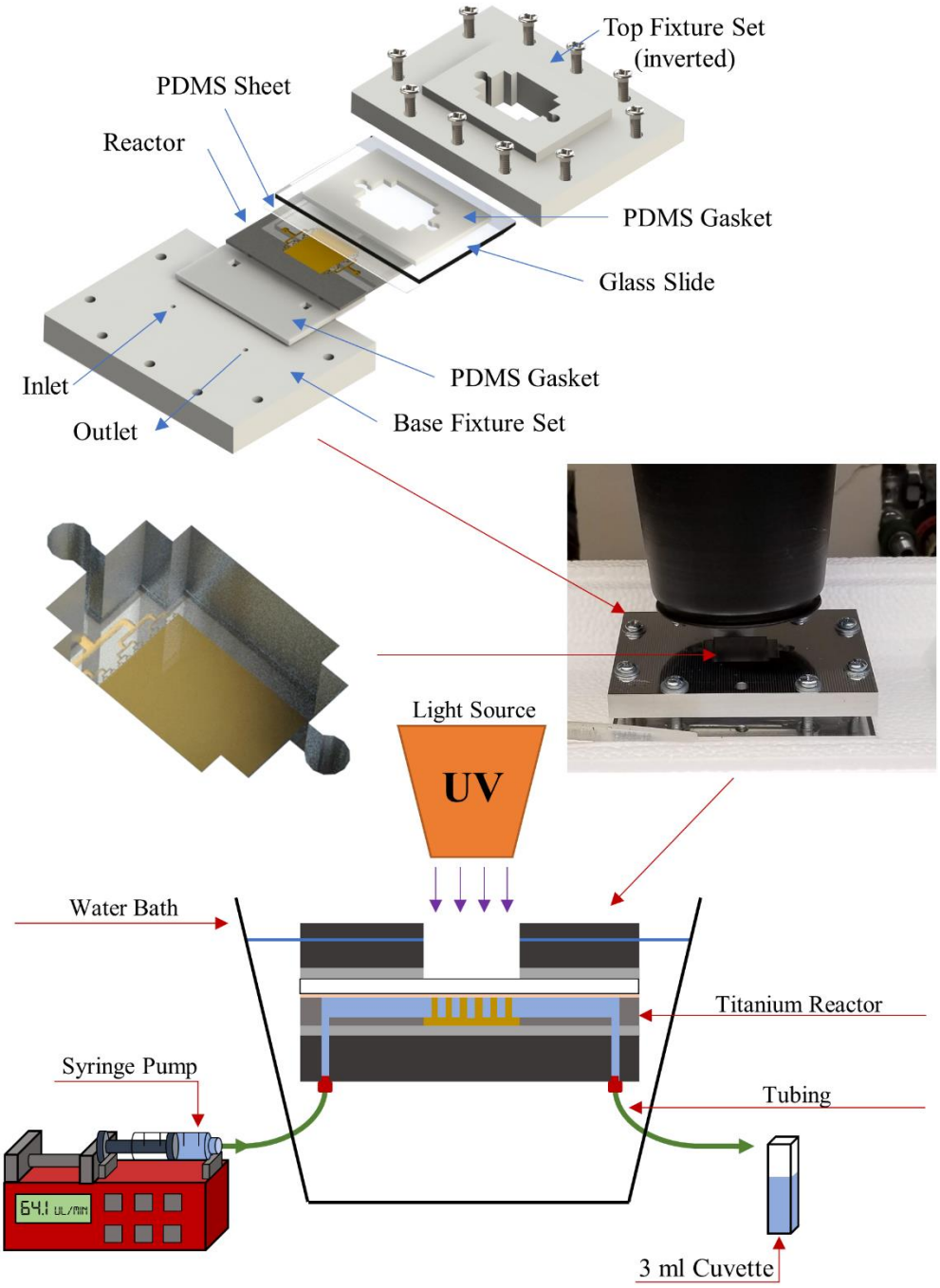

Figure 5.3. (Top) Exploded view of constructed microreactor in fixture set. The top fixture set is depicted upside down to show the extruded platform that was used to localize pressure only to the area of the microreactor. (Bottom) Experimental setup for measuring MB degradation, constructed device was placed into room temperature water bath and a syringe pump was used to flow MB through the system.

To conduct the experiments, finger-tight fittings and 0.010" ID tubing (Idex) were connected to the bottom of the base fixture set to allow flow to be passed through the device. The inlet tubing was connected to a 10 ml glass syringe (Hamilton) and fixed into a syringe pump for precisely controlling flow of MB solution. The constructed reactor was placed into a room-temperature water bath to control temperature. A 365 nm Blak-Ray B-100A 100W lamp with a funnel was positioned 1" above the Ti reactor, yielding a light intensity of 5.5 mW/cm^2 when measured through the glass slide bonded to PDMS (i.e., identical conditions to the experimental setup). The outlet tubing was placed into an Erlenmeyer flask for collecting processed MB. To make the experiment comparable to those reported in the literature, 20 µM (7.478 mg/L) of MB was selected as the target concentration. This concentration was double that of the ISO standard reported for bulk reactor degradation and is identical to the concentration used in a 2018 study by Li et al.[47,101]

To compare the performance of all six devices, 5 fixed residence times were selected (40, 30, 20, 10, 5 sec) and flow rates were adjusted according to the chamber volume and desired residence time. After enclosing the reactor into the fixture set there was air present in the channels, so 2 ml of 200 proof ethanol was flowed through the device at the longest residence time to purge the system. Ethanol's low surface tension helped to prevent air bubbles from forming and getting trapped inside the chamber. To clean ethanol out of the system, 2 ml of DI water was sent through the device at the same flow rate. Afterwards, the MB solution was flowed through the reactor at a residence time of 40 seconds for a total of 1 hour while the glass window was covered to allow dark adsorption

to occur. After 60 minutes, 1.5 ml of MB was collected for a post-adsorption measurement. A UV-Vis Thermo Scientific Evolution 60 spectrometer was used to take MB absorption measurements at a wavelength of 665 nm. After the adsorption measurement the cover was removed, and the UV lamp was positioned above the sample. To purge the system of unexposed MB, 1 ml was passed through the device before the photocatalytically degraded MB was collected. This procedure was repeated for each of the five flow rates, after collecting 1.5 ml of degraded MB the flow rate would be increased and 1 ml was passed through before collection at the new flow rate began. This experiment was repeated three times for each device to measure an average. Reactors were reused due to the complexity of device fabrication. To ensure there was minimal contamination between experiments, 5 ml of ethanol was sent through the device at the fastest flow rate followed by 5 ml of DI water. This process helped to remove adsorbed contaminants within the device through shear forces. A new 250 μm PDMS sheet and glass slide were used for each experiment because MB fouling did occur on the PDMS as it was exposed to MB flow. Reactors were also visually inspected with SEM to ensure there was no damage to the NPT or excessive adsorbed MB. In addition, a MP100 and a P100 without NPT were subjected to the same process as above to establish a baseline and ensure that MB degradation was not a result of UV photolysis.

To measure the effect of prolonged MB degradation, we conducted a durability study using a MP100 reactor. MP100 was subjected to the same procedure above, but with a constant flow rate equivalent to 40 seconds residence time. Spectroscopy measurements were made every hour for 15 hours. Only one depth was used because durability was

expected to be similar across all depths. The experimental conditions are listed in Table 5.1.

Device	Chamber Vol. (µL)	Flow Rate (µL/min)				
P50	24	36.0	48.0	72.0	144.0	288.0
P100	49	73.5	98.0	147.0	294.0	588.0
P150	73	109.5	146.0	219.0	438.0	876.0
MP50	24	36.0	48.0	72.0	144.0	288.0
MP100	42	63.0	84.0	126.0	252.0	504.0
MP150	65	97.5	130.0	195.0	390.0	780.0
	Residence Time (s)	40	30	20	10	5

Table 5.1. Chamber volumes and corresponding flow rates for each of the 6 devices tested. P50 and MP50 had similar volumes because the chamber depth of MP50 was deeper than the 50 µm target depth. Target depths of 50, 100, and 150 µm were nominal and actual etch depth varied due to variations in geometry and etching dynamics.

5.2.4 Performance Metrics

Each device was evaluated using four performance metrics to establish a detailed analysis of micropillar and depth effects. These include percentage of MB degraded (% MB), reaction rate constant (k, min^{-1}), degradation rate (µg/h), and activity (mg/hL). The % MB is the difference between the post-adsorption measurement and the MB absorption value after it has passed through the system. The k values were calculated identically to the values reported for bulk reactor degradation found in Chapter 4, described by equation 3. Degradation rate is the mass of MB degraded per hour, which is heavily influenced by initial concentration, chamber volume, and flow rate. Activity is equivalent to degradation rate but normalized to the chamber volume. While their use is not as commonplace, the degradation rate and activity were reported herein to allow direct performance comparisons to the broader microreactor literature (i.e., comparison to those reports that provided

sufficient experimental details to allow calculation of these parameters retrospectively). Activity was also a metric of particular interest herein, since this provided means for evaluating the most space-efficient reactor design, a critical consideration for the target application within the WRS.

5.3. Results and Discussion

5.3.1. Microreactor Performance Evaluation

Each sample was characterized with SEM imaging and Dektak surface profilometry to get an accurate depth measurement for calculating chamber volume. The measured chamber volume was used to determine the flow rate for each residence time. Images of a micropillar reactor are shown in Figure 5.4.

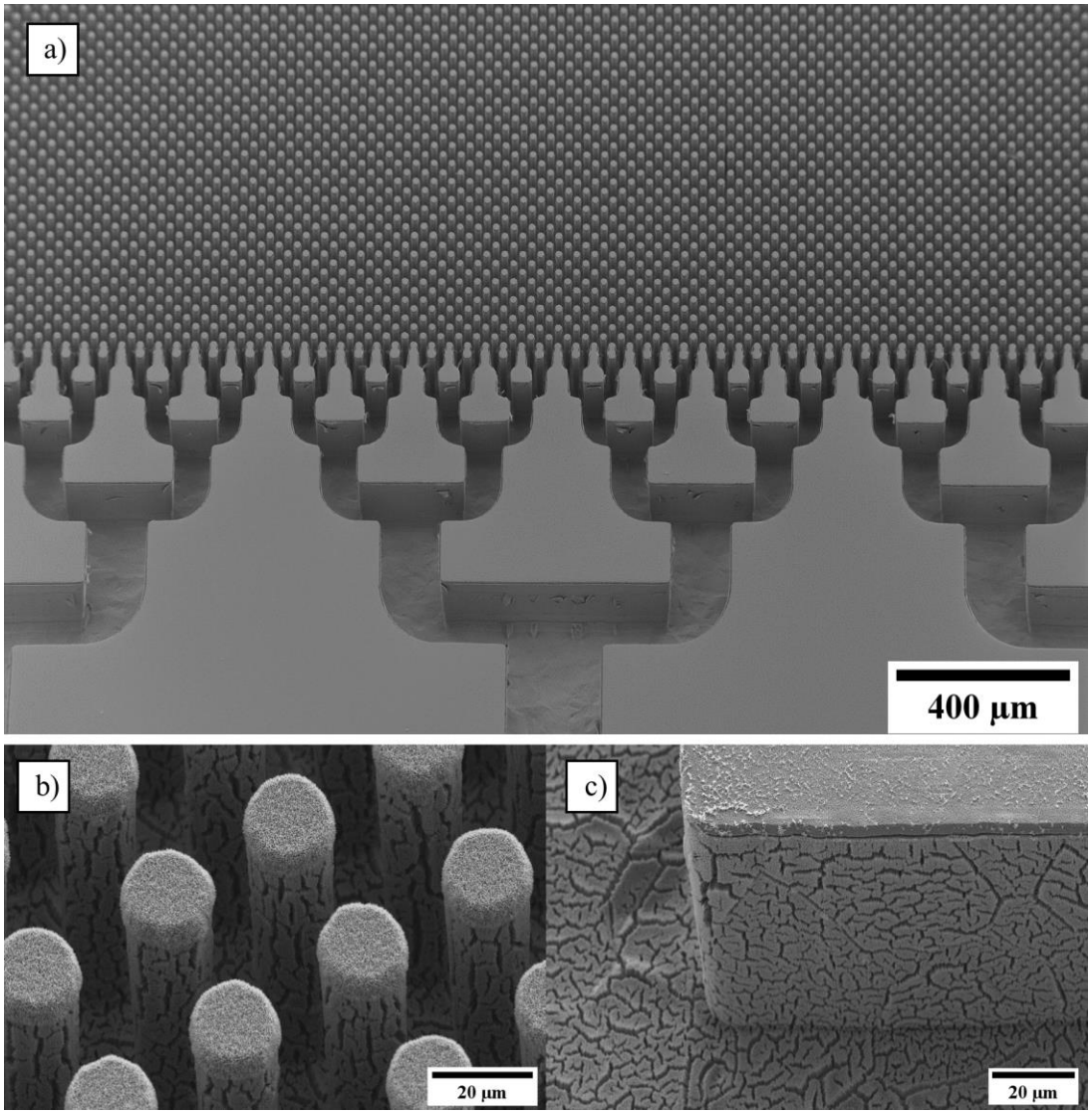

Figure 5.4. Scanning electron micrographs of a) MP100 after Ti etching, showing good sidewall profile control, etch uniformity, and feature fidelity; b) close-up image of micropillars from MP50 coated with NPT, showing minimal NPT delamination; and c) close-up of sidewall and channel floor of bifurcating flow distributor for MP50 device, showing NPT morphology similar to that sees on the micropillars, and the flat Ti foils discussed in Chapter 4.

5.3.1.1. Methylene Blue Concentration Change

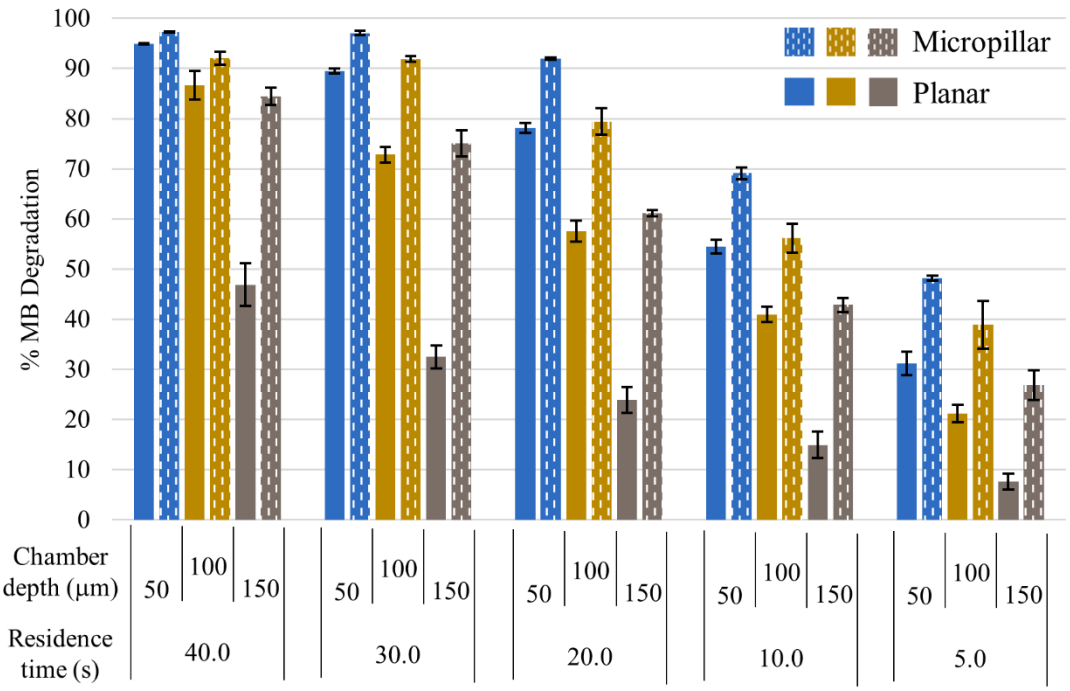

Figure 5.5. Plot of methylene blue degradation for each device. The bars with vertical dashes indicate micropillar reactors, while the solid bars indicate performance of planar reactors. Micropillars increased %MB degradation, while increasing depth decreased %MB degradation.

The concentration change of MB for each of the six devices is shown in Figure 5.5. Of the six devices, MP50 degraded the largest concentration of MB, eliminating an average of 97.26 $\pm$ 0.16% at a residence time (*rt*) of 40 seconds. As *rt* was decreased, MP50's performance dropped marginally but did not fall below 90% until a *rt* of 10 seconds. P50, the flat counterpart to MP50, degraded 94.91 $\pm$ 0.16% MB at the longest *rt*, only 3% less than MP50. However, this differential widened as *rt* was decreased, since P50 performance dropped off at a faster rate with decreasing *rt*. The largest differential between the two devices occurred at a *rt* of 5 seconds, during which MP50 degraded 16.97% more MB than P50. This trend was repeated when comparing the results of MP100 to P100 (largest

differential of 21.82%) and MP150 to P150 (largest differential of 42.60%). In every case, the micropillar reactor degraded more MB than its flat planar counterpart. Due to identical geometry between MP and P devices of the same depth, apart from micropillars, it can be concluded that the performance improvement was solely attributed to the addition of the micropillar array.

MB degradation was observed to be inversely related to microreactor depth for both micropillar and flat planar reactors, i.e. as reactor depth increased, the percentage of MB degraded decreased. This can be explained for planar devices, since flow was laminar and mass diffusion distance increased with depth, thus requiring MB molecules to diffuse greater distances to reach the NPT on the reactor floor. Additionally, deeper devices required photons to travel a greater distance through the MB solution to reach the NPT. Larger photon diffusion distances increase the probability for the photon to be scattered or absorbed prior to interaction with the catalyst.

Micropillar devices also suffered a loss in efficiency as depth was increased, though to a lesser extent compared to planar devices, likely due to the constant mass diffusion distance at every depth. Unlike in planar devices, the maximum diffusion distance in a micropillar device is linked to half the distance between two offset micropillars and stays constant at 6.5 μm regardless of depth. As such, pillar-induced scattering was likely the primary factor that impacted deeper micropillar devices. Specifically, we hypothesize that absorption or diffuse scattering of photons incident upon the pillar sidewalls would cause a decrease in the photon flux with increasing depth into the chamber, and thus, the concentration of hydroxyl radicals available for degradation of MB.

5.3.1.2. Reaction Rate Constant

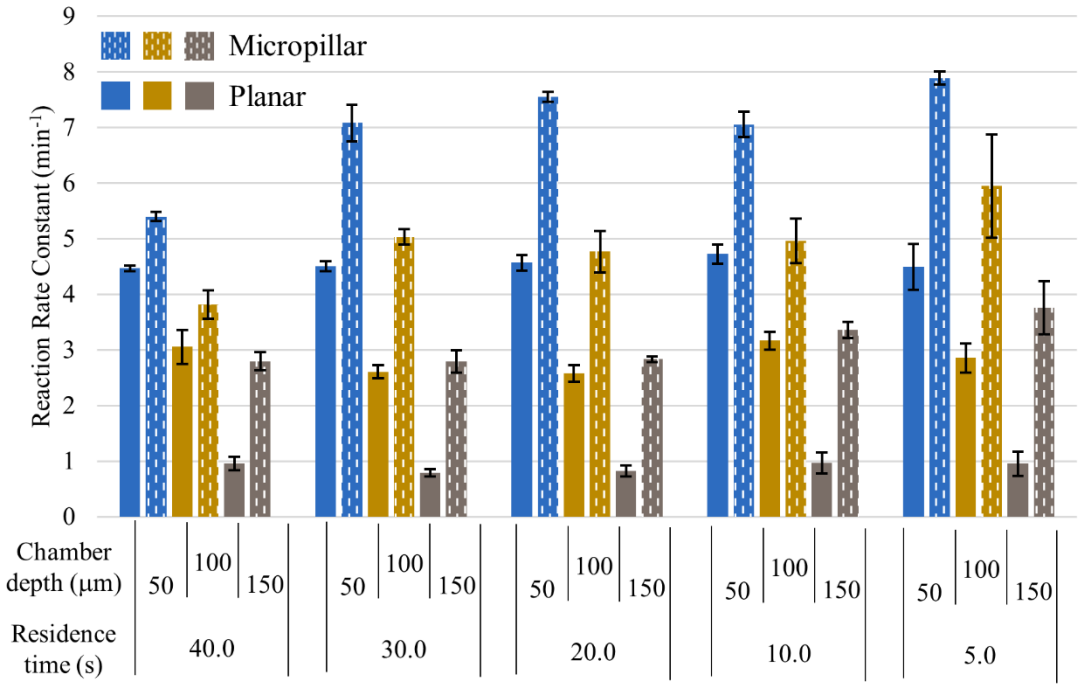

Figure 5.6. Plot of reaction rate constant (min^{-1}) calculated from the Langmuir-Hinshelwood model for first order reactions. Larger reaction rate constants indicate faster reaction rates. Micropillar devices exhibited greater reaction rate constants than their planar counterparts. Reaction rate constants also decreased with increased depth for both MP and P devices; however, while they generally increased with shorter residence times for MP devices, they remained largely constant for P device.

The reaction rate constant was calculated to gain insight into the rate of reaction and for comparison to the bulk reactor system reported in Chapter 4. Figure 5.6 shows the results of the *k* for the six devices. MP50 had the largest reaction rate of 7.89 $\pm$ 0.120 min^{-1} at a *rt* of 5 seconds, while P50's *k* value of 4.450 $\pm$ 0.413 min^{-1}, though still large compared to other published devices, was over 1.5x smaller than its micropillar counterpart. Performance dropped off more significantly as depth increased for planar devices compared to micropillar devices, each with a *k* value range of 0.79 to 4.450 min^{-1} and 2.79 to 7.89 min^{-1} respectively. The largest disparity being between the MP50 and the

P150 device which had an order of magnitude difference between the *k* values, thus demonstrating the significant effects of micropillars and chamber volume. Overall, the results showed that each micropillar device had a larger *k* than its planar counterpart. The *k* values for the both types of devices decreased as depth increased and the *k* values generally increased as the *rt* decreased. The longer optical pathways associated with increased depth lowered the catalyst irradiance slowing the reaction rate and the taller channels decreased MB diffusion to the region of photocatalytic activity.[23] Shortening the *rt* often led to larger *k* values due to the higher rate of mass transfer. The greater flow rates associated with shorter *rt*'s led to more MB interacting with the catalyst and therefore larger *k* values.[47]

When we compared the microreactor results to those of the bulk NPT reactor study found in Chapter 4, we found that minimizing reactor volume to the microliter-scale resulted in vast improvements to the *k* values. The optimized NPT sample in a bulk reactor system managed a *k* value of 0.0060 min^{-1} compared to the largest *k* of 7.89 min^{-1} for MP50, an improvement of three orders of magnitude over the bulk reactor system. The *k* value is strongly influenced by factors such as chamber geometry, mass transfer rate, and intrinsic reaction rate.[29] When decreasing the dimensions of the reactor, all the microreactor advantages mentioned in Chapter 2 come into effect. The mass transfer rate was arguably the most significant advantage and was vastly improved in the microreactor due to a reduction in reaction chamber volume from 50 ml (bulk system) to 24 μL (MP50). The second major factor was dramatic differences in SA:V ratios, the bulk reactor system had a SA:V ratio three orders of magnitude smaller than the micropillar devices. This was

because the small 1 in^2 immobilized catalyst was suspended in a solution volume 2000x larger than that of the microreactor chamber volume. These two characteristics were also the reasons why a micropillar device showed notable improvement in *k* values over a planar device.

5.3.1.3. Degradation Rate

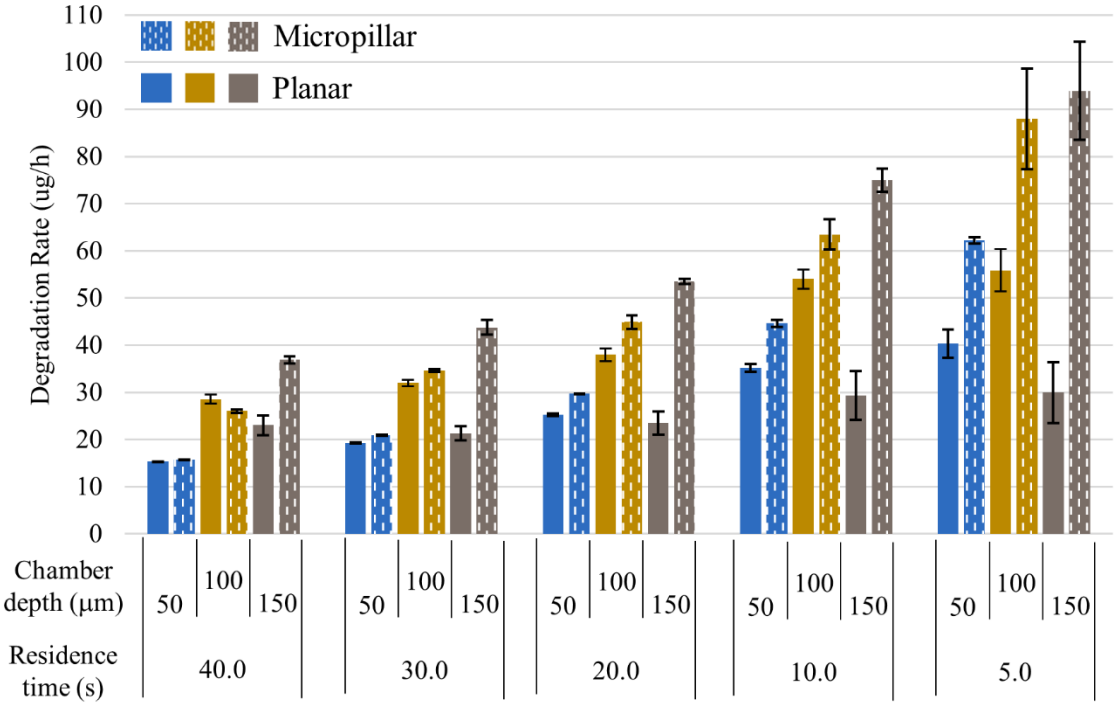

Figure 5.7. Plot of degradation rate (µg/h) vs. each device at varying residence times. Degradation rate is the mass of MB degraded per hour. The key parameters that greatly influenced the degradation rate were shorter residence times (increased flow rates) and larger chamber volumes. Even though the larger devices were less efficient (see figure 5.5 and 5.6), the devices with the larger chamber volume could produce the greatest level of throughput which contributed to large degradation rates.

Based on the results found in Figure 5.7, the degradation rate was heavily influenced by residence time (flow rate) and chamber volume. As is the case with the other

two performance metrics discussed thus far, the addition of micropillars contributed to improved degradation rates over the planar counterparts in every instance except for MP100 vs P100 at *rt* 40.0 seconds (negligible performance difference). MP50 yielded the largest concentration change of MB, and the largest *k*, but it produced the lowest degradation rate of the micropillar devices at 62.27 $\pm$ 0.67 μg/h at a *rt* of 5 seconds. MP150 produced the greatest degradation rate overall at 93.94 $\pm$ 10.39 μg/h at a *rt* of 5 seconds.

For all micropillar devices, the degradation rate increased as *rt* was decreased. This was due to the higher flow rates, which increased throughput, thus allowing a greater volume of MB to be pushed through the device each hour. Even though the MP reactors were less efficient at greater flow rates, as seen in Figure 5.5, a greater volume of fluid was passed through the system, collectively accounting for a larger mass of MB degraded over an hour. The second noticeable trend was that the degradation rate increased as chamber volume was increased. This was because deeper devices have a larger chamber volume and must accommodate larger flow rates to maintain the predetermined *rt*. MP150 had the largest chamber volume (65 μL) among micropillar devices, and at a *rt* of 5 seconds (780.0 μL/min), had a throughput rate of 46.8 ml of solution per hour. Even though MP150 had only demonstrated a MB degradation percentage of 26.84 $\pm$ 2.97% at a *rt* of 5 seconds, more MB would be degraded over an hour compared to MP50. MP50 would yield a maximum throughput rate of only 17.3 ml an hour with a MB degradation percentage of 48.19 $\pm$ 0.52%, at the same *rt*.

Planar devices did not follow the same overall trend, in that the reactor with the largest degradation rate was P100 (55.88 $\pm$ 4.5 μg/h at a *rt* of 5 seconds) and not P150

(29.98 ± 6.45 μg/h at a *rt* of 5 seconds). The degradation rate increased from P50 to P100 but dropped off at a depth of 150 μm. This was because P150 was too inefficient for the degradation rate to further increase over P100. Even though P150 had the largest flow rate compared to the other planar devices, its lower efficiency (see Figure 5.5 or 5.6) severely impacted the degradation rate, and the trend observed for the micropillar devices was not able to continue beyond a depth of 100 μm for the planar devices. The degradation rate of the P150 device illustrates that planar reactors with depths greater than 150 μm will experience a significant detriment to performance that would outweigh the benefits of a larger chamber volume. Therefore, the depth of a planar reactor should be kept between 100 and 150 μm deep to maintain the balance of higher throughput with degradation efficiency.

These results further demonstrate the utility of the micropillar array. In Chapter 2 we reported that throughput is the major limitation of microreactor technology, and one commonly reported solution is to scale-up reactor dimensions. However, as demonstrated by the results of the planar reactors in this study (and those of several studies by others that have investigated depth effects in planar reactors), we can conclude that scaling up dimensions to accommodate increased throughput is not viable beyond depths of 100 to 150 μm. The results for the micropillar devices clearly demonstrate that the addition of catalyst scaffolding within the reaction chamber allows realization of high throughputs while reducing the efficiency loss penalty relative to planar reactors.

5.3.1.4. Activity

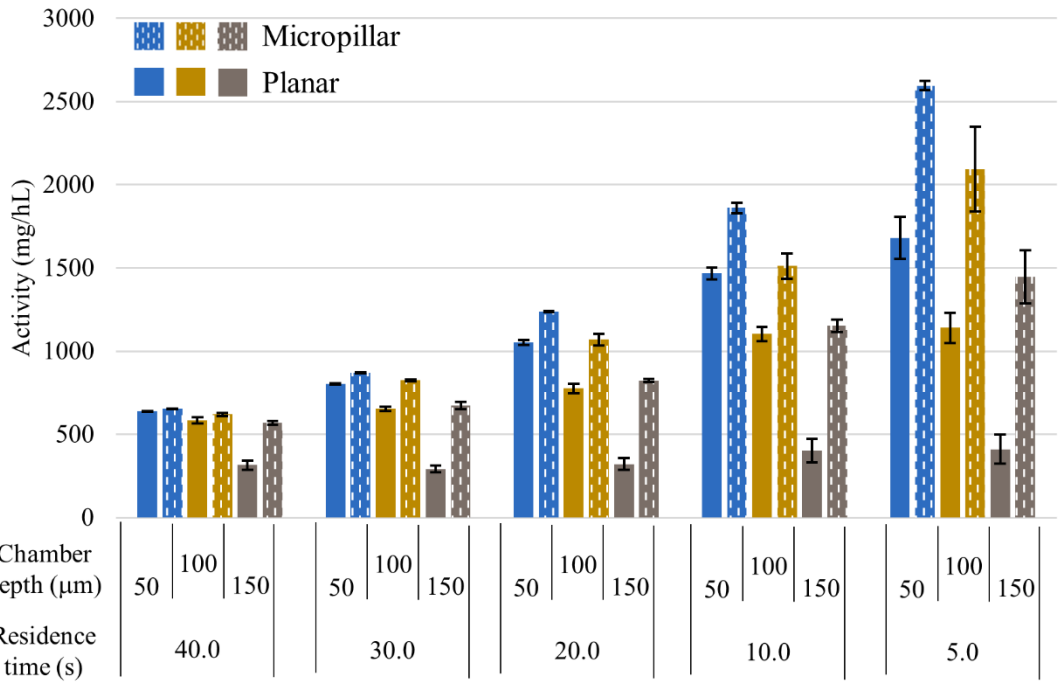

Figure 5.8. Plot of activity (mg/hL) vs. residence time for each device. Activity is a metric of reactor efficiency, and is calculated by normalizing the degradation rate by the chamber volume. MP50 yielded the highest activity at each *rt*, due its combination of a large reaction rate constant and small chamber volume.

The activity performance metric, defined as the degradation rate normalized by the chamber volume, was calculated to determine which device was most efficient for its size. As can be seen in Figure 5.8, each micropillar device exhibited greater activity than its planar counterpart. MP50 produced the highest activity, 2595 $\pm$ 28 mg/hL at a *rt* of 5 seconds, while P150 had the lowest activity, 291.6 $\pm$ 20 mg/hL at a *rt* of 30 seconds. Activity increased as *rt* decreased, due to the increased reaction rate at higher flow rates, and the increase in degradation rate with greater flow rates. Devices with larger chamber volumes were observed to be less efficient and displayed lower activity compared to devices with smaller chamber volumes. There was a 75% decrease in activity between P50

and P150 at a *rt* of 5 seconds, however, MP50 and MP150 only experienced a loss in activity of 44% between the two depths. The increased photoactive surface area and fixed mass diffusion distance contributed to a smaller performance deficit between the two depths.

Photocatalytic microreactor publications commonly report degradation percentage and *k* to demonstrate performance of the novel device over a conventional one. However, directly comparing these two performance metrics to other published devices is not ideal because experimental conditions, such as target contaminant, concentration, flow rates, residence times, chamber volume, and light intensity can vary between each study, and each parameter can dramatically affect the outcome. The degradation percentage and *k* values are heavily dependent on the operating conditions, so the use of degradation rate and activity, which include concentration, *rt*, degradation percentage, and chamber volume in their calculation, allows for more direct comparisons. The precedent for using degradation rate and activity for the purpose of comparison has been well-established in the literature. For example, Fernández-Pérez et al. used activity to evaluate and compare a ZnO flow-through photo reactor to other reported microfluidic devices,[102] and Lin et al. used it for comparison of a metal-ion doped microreactor.[76]

One parameter not investigated in this study that has an effect on the four performance metrics discussed in this chapter is light intensity. Photonic efficiency (ξ) is the ratio of the reaction rate to the incident light intensity and is described by

$$\xi = \frac{rate\ of\ reaction}{incident\ monochromatic\ light\ intensity} \tag{10}$$

where incident light is the light intensity on the reactor.[44] It has been demonstrated that increasing light intensity leads to an increase in photocatalytic activity. A higher photonic flux produces a greater density of hydroxyl radicals and improves the reaction rate. As light intensity is increased beyond a critical value to a point of photonic saturation, the reaction rate becomes independent of light intensity.[103] We did not investigate light intensity because of the targeted application for the NPT MP reactor. In the UV-rich environment of space there should be no shortage of photons for reactor irradiation and the rate limiting factor would likely be flow rate. The light intensity used in this study is also sufficiently low that we can confidently claim that the high MP reactor performance was not primarily due to a large light intensity. However, a future study to investigate the effect of light intensity should be conducted. The micropillars in the reaction chamber contributed significant photocatalytic enhancement at greater depths compared to flat planar devices. Each micropillar device had a uniform molecular diffusion distance, independent of depth, meaning that photon penetration was the rate limiting factor. A future study could investigate the effect of greater light intensities on micropillar devices. With a greater incident photonic flux, the probability of photons reaching all NPT surfaces of MP150 devices would increase resulting in improved degradation percentages that may match those of the MP50 device.

5.3.2. Microreactor Durability

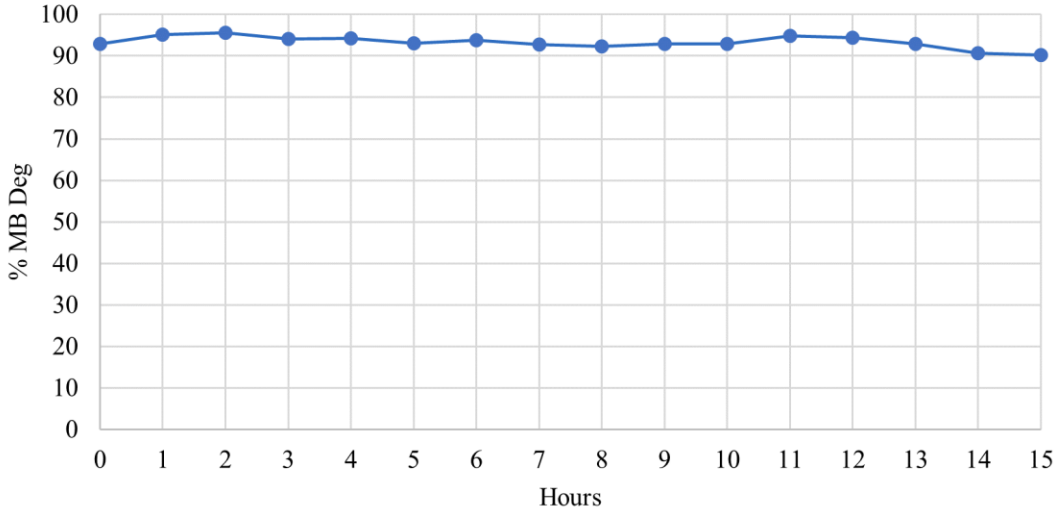

Figure 5.9. MB degradation for MP100 over 15 hours. Data was collected identically to the MB flow rate studies and a residence time of 40 seconds with a flow rate of 63.0 µL/min was used. An initial concentration measurement, at time 0h, was recorded after the post-adsorption step and over 15 hours the percentage of MB degradation only decreased by 2.7%, indicating stable performance over a prolonged period.

The durability of the micropillar reactor was investigated because MB fouling is a commonly reported problem when reusing devices. The longest *rt* of 40 seconds, equivalent to 63.0 µL/min, was used across the entire experiment and an initial measurement was collected with UV exposure after the adsorption step. As shown in Figure 5.9, MP100 degraded 92.84% of MB at the initial time point zero and rose to a peak degradation amount of 95.53% after two hours, ultimately ending after 15 hours of continuous flow at a degradation percentage of 90.17%. From beginning to end of the experiment, MP100 only exhibited a loss of 2.67% and a maximum loss of 5.36% as a result of fouling. This reflects a highly efficient device overall and suggests that the micropillar devices experienced some mild self-cleaning effects. We hypothesize that fluid shear contributed to removal of adsorbed intermediate species that could block photoactive

sites on NPT. The durability performance of the NPT MP reactor demonstrated a high degree of reliability compared to several other publications which reported a similar study.[47,74] The high level of NPT MP durability also shows promise for use in deep space applications. A replacement for the thermal catalytic oxidation reactor would need proven reliability to make it a cost effective alternative. The performance of the NPT MP reactor bodes well for continuing to investigate long-term reliability studies to further support the case for photocatalytic devices as a viable replacement for thermal catalytic reactors.

5.3.3. Literature Comparison

Device	Light Source	MB (mg/L)	Reaction Volume (µL)	Flow Rate (µL/min)	Residence Time (s)	Degradation Percentage	Reaction Rate Constant (min^{-1})	Degradation Rate (µg/h)	Activity (mg/hL)
MP50 (this work)	100 W, 5.5 mW/cm^2	7.478	24	288	5	48.2	7.89	62.3	2595
				144.0	10	69.1	7.05	44.7	1861
				72.0	20	91.8	7.50	29.7	1237
				48.0	30	97.1	7.08	20.9	871
				36.0	40	97.3	5.40	15.7	655
P50 (this work)	100 W, 5.5 mW/cm^2	7.478	24	288.0	5	31.2	4.50	40.3	1681
				72.0	20	78.2	4.57	25.3	1052
				36.0	40	94.9	4.47	15.3	639
Dual Film NR[47]	150 W, 2.0 mW/cm^2	7.478	40	120	20	48	2.0	25.8	646
				30	80	90	1.75	12.1	303
Metal-Ion MR[76]	200 W, 8.0 mW/cm^2	20	150	500	18	20	0.74	120.0	800
				100	90	63	0.66	75.6	504
Biomimetic MR[99]	150 W, 100 mW/cm^2	11.217	5	75	4	13	2.09	6.6	1312
				25	12	41	2.64	6.9	1380
P25 MR[45]	16 W, 1.1 mW/cm^2	11.217	90	600	9	13	0.92	52.5	583
				75	72	55	0.67	27.8	308
Coated Fiberglass MR[74]	150 W, 2.0 mW/cm^2	7.478	50	200	15	45	2.39	40.4	808
				33.3	90	90	1.535	13.5	269
ZnO Continuous Flow-Through Reactor[102]	400 W, 9.9 mW/cm^2	10	99	333.3	17.8	64.6	3.500	129.2	1305

Table 5.2. Caption is on the following page.

Table 5.2. Summary table of photocatalytic microreactor performance data and experimental conditions for the current work, as well as previous reports from others, all for degradation of MB specifically. The ZnO reactor is included to show performance of a different material and because Fernández-Pérez et al. reported on activity as a means for comparing work reported by different authors.[102] Important note: In cases where certain performance metrics were not reported explicitly in the cited studies, these were estimated based upon experimental conditions reported therein.

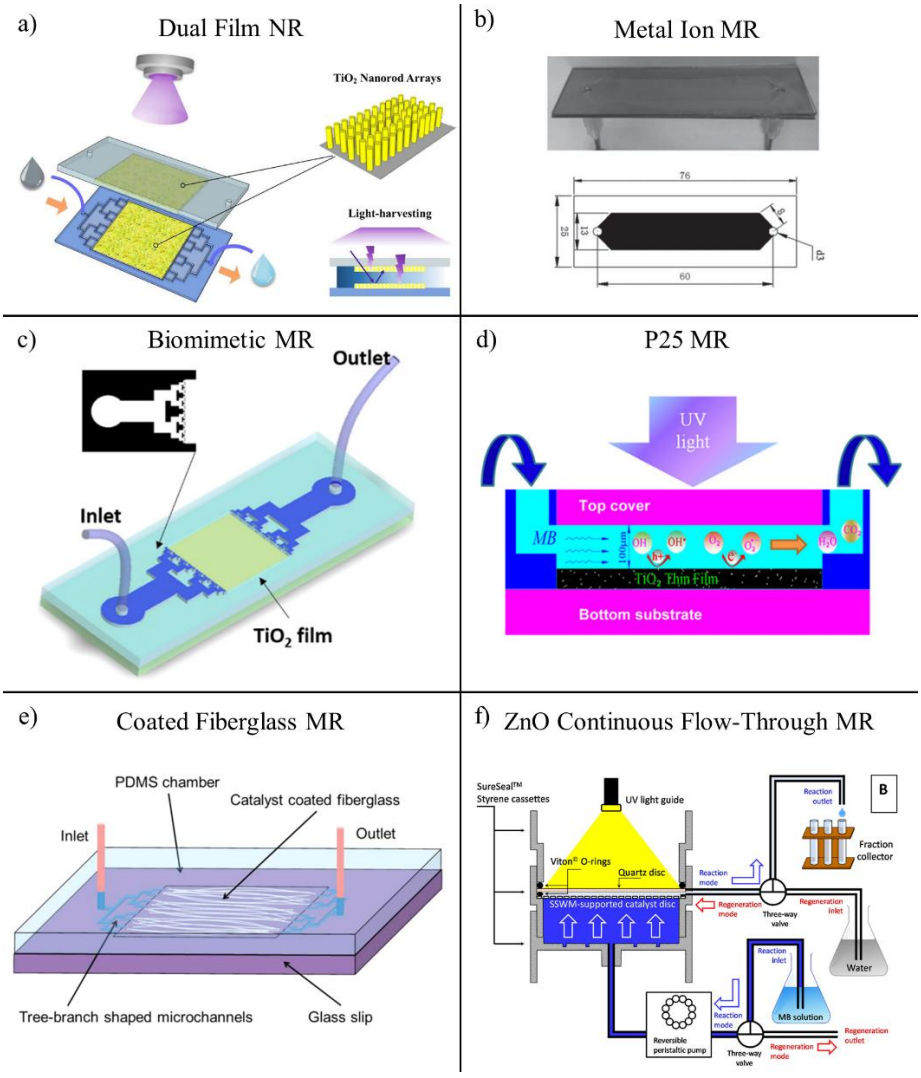

Figure 5.10. Schematics of all six devices that are listed in Table 5.2. a) Dual Film NR[47]; b) Metal-Ion MR[76]; c) Biomimetic MR[99]; d) P25 MR[45]; e) Coated Fiberglass MR[74]; f) ZnO Continuous Flow-Through Reactor[102].

Parameters from similar microreactor publications were collected and organized in Table 5.2 and schematics are displayed in Figure 5.10, for comparison to MP50, the best performing device in this study. Since degradation rate and activity were only reported in two of the six publications listed in the table, these performance metrics were calculated for the other four publications using experimental conditions reported therein. As shown in the table, the MP50 devices were able to achieve activities that surpassed previously reported devices by 2 to 5-fold. Below, we further discuss the critical advantages of the MP reactor, thus demonstrating the advantages conferred by the increase catalyst loading and reduced diffusion lengths therein.

The most recent comparable study was conducted by Li et al. in which they doubled the SA:V ratio of a planar reactor by depositing TiO_2 nanorod arrays on the top and bottom surfaces of the reaction chamber.[47] This dual-film construction yielded an activity of 646 mg/hL, 4x smaller than MP50. The design of the Dual-Film NR device was novel and succeeded in increasing the photoactive surface area, however the design had some weaknesses that hindered its performance. For example, absorption within the upper nanorod film reduced photon flux reaching the nanorod layer on the chamber floor, thus limiting its ultimate contribution to degradation. Additionally, as we observed in the current work, photocatalytic efficiency drops off significantly between depths of 100 and 150 μm in flat planar devices. It is likely that the Dual Film NR reactor suffered some efficiency loss due to mass and photon transfer limitations at a chamber depth of 200 μm. It is important to note that the light intensity used in the Dual-Film NR study was only 2.0

mW/cm^2, compared to MP50's incident light intensity of 5.5 mW/cm^2, so it is possible the Dual-Film NR performance would be improved with a higher intensity light source.

The Metal-Ion MR sought to improve photocatalytic degradation of MB by comparing a multi-channel reactor to a planar one and experimenting with metal-ion doped TiO_2.[76] The planar reactor with 0.05% Cu^{2+} doped TiO_2 yielded the best results and reported a maximum activity of 800 mg/hL, over 3x times lower than MP50. This was one of two papers that reported activity and used it for literature comparison, with the authors referring to activity as degradation rate per reaction volume (DRPRV). In addition, this was also one of two devices that achieved a greater degradation rate than any of the NPT reactors. The Metal-Ion MR reported a degradation rate of 120.0 µg/h, roughly twice that of MP50. Important differences between the two devices that contributed to this difference are the chamber volumes and MB concentration. Each of these parameters affects the outcome of the degradation rate, in addition to the other parameters listed above, but these two likely had the largest effect. The chamber volume of the Metal-Ion MR was 150 µL, 6x larger than MP50, which allowed higher flow rates to be used with longer residence times. It is also important to note that only two MP50 devices in parallel are needed to achieve the same degradation rate as the Metal Ion MR, at only one third of the reaction chamber volume. The MB concentration was 20 mg/L, this larger concentration in combination with larger flow rates, led to an increased degradation rate because a greater volume of fluid processed over an hour and there is more available MB for degradation. Comparing two devices based solely on degradation rate would mean that, in most cases, the device with a larger degradation rate may not be the most efficient due to differences

in experimental conditions and chamber volume. By normalizing the degradation rate with chamber volume one can compare two devices and determine which is more effective for its size. A critical conclusion to make when the target application has dimensional constraints.

The Biomimetic MR sought to improve degradation percentage by decreasing the pressure drop within the system and improving flow velocity to yield a faster photocatalytic reaction rate within the reactor by using a biomimetic-inspired flow distribution network.[99] This device had the largest activity behind MP50 in Table 5.2. The small chamber volume of the Biomimetic MR (5 μL), a constant depth of 50 μm, and a larger fluctuation in flow velocity, which facilitated greater mixing, contributed to the higher level of activity. One notable difference with this experimental setup is the light intensity was 100 mW/cm^2, far larger than any other light source used in the comparable literature. However, without a study for each device to determine photonic efficiencies at different light intensities it is difficult to assess the contribution of a more powerful light source.

The P25 MR was selected for comparison due to its resemblance to a traditional planar reactor design and its use of Degussa P25 nanoparticles, the most widely used form of TiO_2 photocatalyst. This study sought to compare differences in three colloidal TiO_2 solutions applied using the sol-gel method for use within microreactors. They found that the water-based P25 colloidal dispersion performed best in a microfluidic reactor setup.[45] The P25 MR listed in Table 5.2 was fabricated using the water-based P25 method and achieved a max activity of 583 mg/hL with a chamber volume of 90 μL. In a bulk reactor system, P25 has proven to be more photocatalytically active than NPT, due to its ideal

combination of anatase and rutile crystal structure. When comparing the two materials in a microreactor setup, such as P100 vs P25 MR, we found that the NPT reactor yielded better performance with an activity of 1140.3 mg/hL and a degradation rate of 55.9 μg/h. The clear advantage of NPT over P25 is its ability to form homogeneously over any exposed Ti, allowing uniform deposition of TiO_2 on horizontal and vertical features. P25 applied to a micropillar reaction chamber via the sol-gel method would cause dense aggregates to form around the array and lead to complications with uniform flow and clogging. It is likely that the NPT reactor performed better than the P25 MR because NPT was formed not only in the reaction chamber but within the flow distribution network and vertical sidewalls as well. This added surface area likely improved the degradation rate and activity by increasing the SA:V.

The Coated Fiberglass MR study was most comparable, in theory, to the micropillar reactors. Li et al. used fiberglass coated in TiO_2 to increase the SA:V ratio and introduce turbulence within the flow that would contribute to mixing and reaction rate enhancements. They found that the Coated Fiberglass MR had superior performance compared a conventional flat film microreactor.[74] Adding photocatalyst surface area to the reaction chamber via TiO_2-coated fiberglass is the same, in principle, as adding NPT-oxidized micropillars, both types of reactors utilized scaffolding to improve catalyst loading. The maximum activity of the Coated Fiberglass MR was calculated to be 808 mg/hL, 4x smaller than MP50. It is possible the activity could have been larger if residence times shorter than 15 seconds (larger flow rates) were explored. Several improvements to the device design may have helped to improve the activity. The fiberglass itself was disordered and may have

blocked pathways or created channels, meaning that there would not be a consistent degradation rate across the chamber. Using a scaffolding method that is easier to manipulate would allow uniform reaction rates and possibly improve degradation. Secondly, the Coated Fiberglass MR only had TiO_2 on the fiberglass and not on the chamber floor. This was likely to allow a direct comparison to be made between fiberglass and a flat film, but adding TiO_2 to the chamber floor would maximize the SA:V ratio and improve the activity. Lastly, the reaction chamber had a height of 250 µm, while the coated fiberglass had diameters of 14.2 µm. By decreasing the chamber depth mass transport and photon utilization would be improved and increase the reaction rate of the device.

The ZnO Continuous Flow-Through Reactor publication used activity to compare their device to others. Fernández-Pérez et al. sought to improve upon the limitations of traditional microreactor systems and utilized a stainless-steel mesh supported zinc oxide (ZnO) catalytic disc in a microreactor-type setup. They found that even with poor interaction between the largely hydrophobic polar faces of the ZnO and the MB, the flow-through reactor produced greater activity, 1305 mg/hL, over other microreactors published in literature.[102] MP50 had an activity twice that of the ZnO Continuous Flow-Through Reactor, but a degradation rate half that of the ZnO device.

The two devices listed in Table 5.2 that achieved higher degradation rates than MP50 were the Metal-Ion MR and the ZnO Continuous Flow-Through MR. From the results it is evident that chamber volume and flow rate have a significant impact on the degradation rate. The Metal-Ion MR had a chamber volume of 150 µL and the ZnO Continuous-Flow Reactor had a chamber volume of 99 µL, 6x and 4x larger than MP50.

For microreactor use in a confined space, such as a replacement for the catalytic reactor on the ISS, the ideal reactor would be the smallest most efficient device to optimize the use of available space. Therefore, devices with the highest level of activity should be considered for confined space applications. Even with maximization of throughput as the goal, reactors with the largest activity would be more advantageous over devices with lower activity but a higher degradation rate. This is due to the overall size of each device, the reaction volume of MP50 is 4x smaller than that of the ZnO Continuous Flow-Through reactor but the degradation of rate of MP50 is only half that of the ZnO device. Two MP50 reactors running in parallel would achieve the same degradation rate as the ZnO reactor with only half of the chamber volume. In any real-world application multiple reactors would be required to produce practical flow rates on the order of ml/min, so the ideal photocatalytic water purification device would consist of many MP50 devices in parallel. Operating under the principle that multiple reactors would be needed in real-world applications means that any of the reactors in Table 5.2 would work but MP50 would produce the smallest overall package.

5.3.4. High Throughput Device Concept

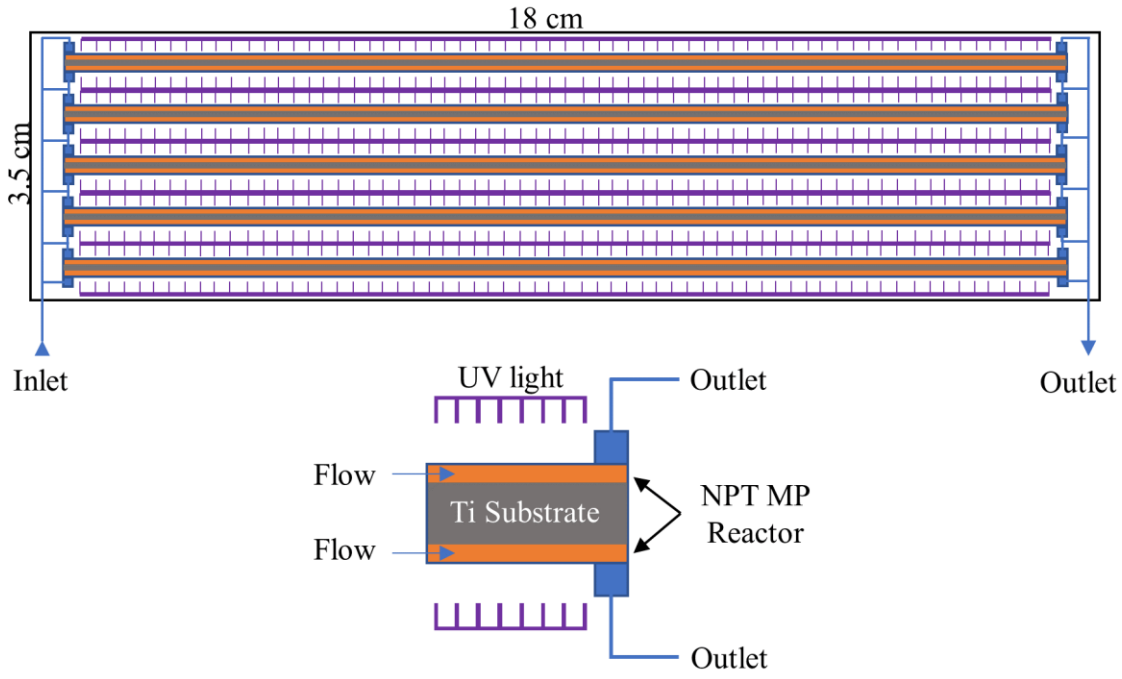

Figure 5.11. A Photocatalytic Multi-Reactor Concept (PMRC) high throughput photocatalytic water purification device. Multiple devices stacked on top of each other with dual-sided UV LED lights allows a greater number of reactors to be combined into a single enclosure. Due to the fabrication method a reactor (orange in picture) can be produced on each side of a titanium substrate (gray) allowing space inside the enclosure to be maximized.

In order to commercialize microreactor technology, multiple PMFRs would need to be plumbed into one complete unit to enable practical flow rates to be achieved. Figure 5.11 depicts a theoretical concept of how a multi-reactor device may be designed and operated. Using the thermal catalytic reactor replacement as an example, the Photocatalytic Multi-Reactor Concept (PMRC) would need to process at least 3 gallons of water a day to support a crew of six.[1] With the PMRC operating 24 hours a day, a flow rate of 7.9 ml/min would be required and it would need to have the same overall dimensions as the catalytic

reactor (3.5 cm diameter and 18.1 cm in length) to avoid complex modifications to the entire WPA system.[7] To ensure that at least 90% of contaminants are degraded, the residence time would need to be at least 20 seconds based on results of MB degradation. The thermal catalytic reactor only degrades VOCs, so studies to determine the ideal flow rate for MP50 to achieve degradation of VOCs would be needed to make a more accurate comparison; however, for the purpose of this example we are assuming the degradation rate would stay the same.

The proposed theoretical design would be constructed into a box 3.5 cm x 3.5 cm x 18 cm and contain 6 titanium substrates with micropillar reactors fabricated on each side (top and bottom) for a total of 12 reactors positioned in parallel. The titanium substrates would be 150 µm thick and each side would have a depth of 50 µm, be 16.2 cm long, and 3.5 cm wide. The reaction chamber would contain micropillars 15 µm in diameter, at a 40 µm pitch. To make the devices watertight a glass wafer with high UV-transmittance can be anodically bonded directly to each side of the titanium substrate.[73] The chamber volume of each single reactor would be 221 µL and require a flow rate of 663 µL/min to sustain a residence time of 20 seconds. All 12 reactors operating in parallel would yield a cumulative flow rate of 8.0 ml/min, enough to process 3 gallons of water every 24 hours. With the 6 titanium substrates occupying less than 1 mm of cumulative vertical space and 12, 500 µm thick glass wafers equaling a total thickness of 6 mm, there would be 28 mm of height remaining to include UV LED panels (or fiber optic waveguides emitting photons redirected from the UV-rich environment of space), wiring, plumbing, and tolerances.

This is purely a theoretical design to propose a solution to the major limitations of microreactor technology. There are several complications with the proposed concept that would need significant testing and optimization to make the design viable. First, the much higher flow rate and longer reaction chamber would dramatically increase the pressure drop across the system. If the pressure becomes too high then serious complications may arise. For example, the glass wafer could crack, or the bond could separate; the NPT could delaminate from the micropillars; and in severe conditions, the micropillars may deform due to fluid impingement. Improvements to the flow distributors and overall design of the reaction chamber could help to minimize the negative effects of pressure drop. The high level of scalability and adjustability of titanium microreactor fabrication allows devices to be tailored for any number of related applications. The PMRC represents a thought experiment to demonstrate the potential of this technology to be useful in real-world scenarios.

5.4. Conclusion

In this chapter we presented a study to quantify the effect of micropillars situated within the reaction chamber of a planar microfluidic reactor and compared performance at three different depths. NPT optimized in the parameter study from Chapter 4 was oxidized onto the titanium micropillar and planar reactors producing high surface area films free of delamination. The results of the MB degradation study concluded that the added surface area and improved mass transfer of the micropillars resulted in significant performance enhancements over the flat counterparts at all depths and residence times. Performance of

the micropillar devices did decrease as depth increased but to a lesser extent than flat devices. The micropillars maintained a constant mass diffusion distance at each depth so it is likely that photon penetration into the micropillar array was the rate limiting factor. Modifying the micropillar diameter and pitch would increase light capture and penetration depth and can be studied in future experiments. Activity was used to compare the results of the micropillar reactors to other microfluidic devices published in literature. MP50, the device with the largest activity in this study, doubled the activity of the next best device found in literature. The superior performance of MP50 shows that not only is MP50 the smallest most efficient microfluidic reactor, but the micropillars significantly improve photocatalytic efficiency of PMFRs as well.

6 CONCLUSION

6.1. Summary of Novel Microfluidic Reactor Concept

Microfluidic reactors present a compelling solution to simplifying the VOC removal process for deep space exploration life support systems. Herein, we have established the groundwork for development of a 3D high-density microfluidic reactor with unmatched photocatalytic performance for its size. To fully utilize the high surface area design improvements of the novel PMFR concept we applied a grey-based Taguchi optimization process to optimize NPT by maximizing the reaction rate constant and minimizing the crack size. The optimized oxidations conditions performed well overall and were successfully deposited onto a Ti micropillar array, demonstrating the feasibility of NPT within PMFRs. NPT is likely the only form of highly photoactive TiO_2 that can be deposited, with such a high degree of uniformity, onto vertical surfaces, a necessity to fully utilize the surface area enhancements of micropillars. The simplicity of NPT oxidation is another advantage over traditional photocatalytic TiO_2, such as P25 nanoparticles. The one-step process of *in situ* oxidation of titanium substrates in H_2O_2 allows a high level of scalability without excess complexity. These advantages are critical to create new, innovative microreactor designs for future implementation.

To demonstrate the performance enhancements of micropillars we compared two PMFR designs, one with micropillars and one without each at three depths. The increased SA:V ratio, light trapping, and decreased molecular diffusion distance, greatly improved the reaction rate of the micropillar devices over the flat counterparts. The micropillar device with a depth of 50 μm, MP50, yielded the largest activity, a performance metric for mass degraded per hour normalized by chamber volume. Activity was used to compare

micropillar reactor performance to that of other devices published in literature. MP50 achieved an activity twice that of the next closest device reported in the literature, indicating that MP50 is the most efficient reactor for its size by a minimum factor of two. The concept of 3D photocatalyst scaffolding has been previously investigated but, to the author's knowledge, has not been as successful as the NPT micropillar reactors presented in this work. This work sets the precedent to explore new design possibilities and seek further improvements, such as photon utilization, to create devices capable of greater performance. While advancements in microreactor technology have stagnated over the past few years, the remarkable performance enhancements of the MP devices reported herein show potential for rejuvenating the field and suggest exciting new directions for future research.

6.2. Future Work for NPT Optimization

The NPT optimization study presented in Chapter 4 worked well to develop baseline oxidation conditions for use within the microfluidic reactors discussed in Chapter 5, but further improvements can be made. Firstly, the optimization study was conducted on flat films and tested in a bulk reactor setup to save time and resources. Performing the parameter study with microfluidic reactors would not have been practical with the number of samples needed to complete the Taguchi study. Additionally, at the time, the Ti microreactor fabrication process was still under development. The operating conditions, growth mechanics, and fluidic forces vary significantly between an immobilized bulk reactor setup and a microfluidic reactor. It may be possible to further improve NPT

oxidation by conducting a smaller-scale parameter study using microfluidic devices. The current study did not include any NPT oxidation conditions that could produce delamination, a critical sign of oxidation failure. A future optimization study could expand the parameter space to include more aggressive oxidation conditions grown within a PMFR. The flow rate studies from Chapter 5 can then be repeated with ramping oxidation conditions until delamination is observed. The new ideal oxidation conditions would then be the values of concentration, temperature, and time that fall just below the conditions that induce delamination. If conditions more aggressive than 10%, 80˚C, 5 hours are possible, then the photocatalytic activity of the micropillar reactor would be further enhanced.

Integrating plasmonic noble metal-based nanoparticles within TiO_2 has been shown to increase photon absorption and photoactivity of the material. Due to its band gap, TiO_2 is only photoactive in the UV spectrum. By broadening photon absorption into the visible range, sunlight could potentially be used as the only light source (6% of sunlight is UV while 50% is in the visible range).[104] Gold, silver, and platinum are common plasmonic nanoparticle materials that, when integrated into the TiO_2, form a Schottky barrier at the interface of the two materials. The metal nanoparticles act as an electron trap and facilitate interfacial charge transfer that decreases the rate of recombination and increases the lifetime of electron-hole pairs.[105] Several studies have investigated doping NPT with nitrogen to modify the microstructure and increase photoactive surface area,[96,106] but there is minimal research on plasmonics-based enhancement of NPT. A potentially simple method to integrate plasmonics into NPT would be to add noble metal nanoparticles into the H_2O_2 solution during the Ti oxidation process. These nanoparticles would become

dispersed in the solution and could potentially be captured within the NPT as it forms. A study to quantify the effect of plasmonics on NPT could be conducted, in which the quantity and type of noble metal is varied, and its photocatalytic performance evaluated using a bulk reactor setup and a light source that extends into the visible range.

6.3. Future Work for Titanium Micropillar Reactor

The micropillar reactors performed exceedingly well compared to other devices published in the literature; however, there are improvements that can be made and other studies that can be conducted to further demonstrate its utility. An investigation into light intensity could be advantageous for designing a high throughput device. Photon penetration was likely the main factor limiting the performance of deeper devices, thus conducting a study under different light intensities may show improved performance at greater depths. If the performance of MP150 could match that of MP50, which is theoretically possible if photon flux is the same across all points along the z-axis of the reaction chamber, then increased flow rates could be sustained and fewer devices would be needed for a multi-reactor high throughput device.

There is also potential for the design of the micropillar reactor to be improved. There is currently a collaborative effort underway to gain a deeper understanding of fluid-micropillar and photon-micropillar interactions. Computational modeling is being used to study light absorption by micropillars of varying diameters, height, and pitch. These three geometric properties also influence the mass transfer of reactants and degradation reactions during fluid flow through the array. Preliminary results have shown that photon penetration

depth is severely limited beyond a depth of 50 μm. Increasing the pitch between the pillars may allow more light into the array but would come with a drop in surface area because fewer pillars would fit into the same space. We are seeking a micropillar geometry to maximization light trapping and mass transfer efficiencies. This new geometry can then be tested experimentally and compared to the results of the current generation of devices.

An improvement can also be made to the packaging of the microreactor by developing a process to anodically bond a glass wafer to the titanium reactor. This would create a water-tight seal and remove the need for the bulky aluminum fixture set and PDMS layers. Khandan et al. demonstrated that an NBK-7 glass wafer with high UV-transmittance can be anodically bonded to a titanium wafer.[107] The major complication with anodic bonding is that NPT, oxidized onto the titanium prior to anodic bonding, would disrupt the bonding process. The conductivity of the NPT would interfere by limiting cation mobility to the cathode during anodic wafer bonding. NPT at the interface of Ti and glass would likely restrict the formation of permanent bonds between the two materials during the anodic oxidation process and the bond would fail. One solution would be to grow the NPT after the bonding process by flowing heated H_2O_2 through the reactor. However, it is not clear how well this would work because the morphology of the NPT may be affected due to the directional flow. There would be significant benefits if the anodic bonding process was successful, since a fully constructed microreactor would have fewer components, and it would allow multi-reactor devices to be packaged in a smaller container.

Thus far, the micropillar reactors have only been tested using MB. In order to demonstrate the technology's potential for supplanting the thermal catalytic oxidation

reactor in life support systems designed for deep space travel, the micropillar PMFE concept must be tested with VOC degradation. Near-term studies can be designed to eliminate the Ersatz solution and DMSD discussed in Chapter 1. Initial tests can be focused on degradation of one VOC component of the Ersatz solution, such as ethanol, the largest source of TOC. There is precedent that TiO_2 can photocatalytically decompose ethanol, therefore it should be possible to do so with the NPT micropillar reactor.[108] The next step would be to attempt degradation of the Ersatz solution and compare the micropillar reactor activity to that of the current thermal catalytic reactor.[4,7] The final study should be focused on degradation of DMSD. This compound had been producing larger concentrations of TOC in the post-processed purified water until NASA was able to discover its source. By decreasing the number of DMSD contributors, the WPA system was able to process and remove measurable quantities of DMSD and decrease TOC, although at the detriment to the lifetime of the Multifiltration Beds. NASA also investigated UV photolysis-based mitigation of DMSD using a flow cell reactor to be used in combination with the catalytic reactor.[11] A future study can be conducted to compare the performance of the photocatalytic micropillar reactor to the photolytic UV flow cell reactor. This DMSD degradation device would have to be designed for use within the confined space of the WPA system so the reactor with larger activity would produce the smallest overall package.

One of the most common applications for photocatalytic microreactors described in literature is water purification. However, there are many cheaper alternative methods to purify water for personal use such as chemical additives. Chlorine is a well-known disinfectant for oxidizing and inactivating pathogens but can produce harmful carcinogenic

by-products.[109] There are also several forms of water-borne bacteria that are resistant to chlorine oxidation such as *Cryptosporidium* and *Giardia* which require a higher dose of chemicals to eliminate. Photocatalytic degradation is an effective alternative to chlorine, in which various mechanisms damage the bacterial cells.[110] In most practical applications, such as point of use systems designed for personal use, a porous filtration system would be more cost effective. Bacteria are commonly on the order of microns and can easily be filtered out by most commercially available and inexpensive porous filtration systems, such as activated carbon. However, harmful viruses can be on the order of tens to hundreds of nanometers and would pass through porous filtration systems. Photocatalytic degradation is a potential solution for eliminating chemical-resistant, nanometer-scale viruses and multiple studies have demonstrated its effectiveness. Photocatalytic degradation has been shown to kill viruses such as Influenza, Poliovirus 1, Hepatitis B, Norovirus, SARS, and Vaccinia.[111] Bacteriophages, such as MS2, are commonly used in experimental studies as surrogate viruses because they are non-hazardous to humans, have a biosafety level 1, are simple to incubate with bacteria like *E-Coli*, and are susceptible to TiO_2 photocatalytic disinfection.[112–114] A future study could be conducted using MS2 bacteriophage as a surrogate to evaluate the micropillar reactor's potential for viral disinfection.

BIBLIOGRAPHY

(1) Mccoy, J. T. 2012 Guidelines for Water Reuse U.S. Water Recovery System on the International Space Station US-TX-NASA Project Background or Rationale.

(2) Carter, D. L.; Tobias, B.; Orozco, N. Y. Status of ISS Water Management and Recovery. *43rd Int. Conf. Environ. Syst.* **2016**, No. July 2016. https://doi.org/10.2514/6.2013-3509.

(3) Kayatin, M. J.; Carter, D. L.; Schunk, R. G.; Pruitt, J. M. Upgrades to the ISS Water Recovery System. **2016**, No. July, 10–14.

(4) Yu, P.; Nalette, T.; Kayatin, M. J. Development of Advanced ISS-WPA Catalysts for Organic Oxidation at Reduced Pressure/Temperature. *46th Int. Conf. Environ. Syst.* **2016**, 1–12.

(5) Bagdigian, R. M.; Dake, J.; Gentry, G.; Gault, M. International Space Station Environmental Control and Life Support System Mass and Crewtime Utilization In Comparison to a Long Duration Human Space Exploration Mission. *45th Int. Conf. Environ. Syst.* **2015**, 1–16.

(6) Carter, L.; Brown, C.; Orozco, N. Status of ISS Water Management and Recovery. *43rd Int. Conf. Environ. Syst.* **2013**, 1–11.

(7) Nalette, T.; Snowdon Hamilton Sundstrand Karen Pickering, D.; Callahan NASA, M. *The ISS Water Processor Catalytic Reactor as a Post Processor for Advanced Water Reclamation Systems 07ICES-39*.

(8) Carter, L.; Bowman, E.; Wilson, M.; Gentry, G.; Rector, T.; Introduction, I.; Support, L.; Team, D.; Engineer, T. L.; Laboratories, B. H.; et al. Investigation of DMSD Trend in the ISS Water Processor Assembly. **2013**, 1–12.

(9) Containing, P.; Methyl, V.; Vms, S.; Marshall, G. C.; Flight, S. Dimethylsilanediol (DMSD) Source Assessment and Mitigation on ISS: Estimated Contributions from Personal Hygiene Products Containing Volatile Methyl Siloxanes (VMS). *48th Int. Conf. Environ. Syst.* **2018**, No. July, 1–12.

(10) Delzeit, L.; Hunter, C. UV Chemistry and Mitigation of Siloxane. *48th Int. Conf. Environ. Syst.* **2018**, 1–12.

(11) Labs, W.; Field, M. Ultraviolet (UV) Mitigation of Dimethylsilanediol (DMSD). *48th Int. Conf. Environ. Syst.* **2018**, No. July, 1–10.

(12) Fujishima, A.; Zhang, X.; Tryk, D. A. TiO2 Photocatalysis and Related Surface Phenomena. *Surf. Sci. Rep.* **2008**, *63* (12), 515–582.

https://doi.org/10.1016/j.surfrep.2008.10.001.

(13) Madhusudan Reddy, K.; Manorama, S. V; Ramachandra Reddy, A. Bandgap Studies on Anatase Titanium Dioxide Nanoparticles. *Mater. Chem. Phys.* **2003**, *78* (1), 239–245. https://doi.org/10.1016/S0254-0584(02)00343-7.

(14) Xu, C.; Rangaiah, G. P.; Zhao, X. S. Photocatalytic Degradation of Methylene Blue by Titanium Dioxide: Experimental and Modeling Study. *Ind. Eng. Chem. Res.* **2014**, *53* (38), 14641–14649. https://doi.org/10.1021/ie502367x.

(15) Fox, M. A.; Dulay, M. T. Heterogeneous Photocatalysis. *Chem. Rev* **1993**, *93*, 341–357.

(16) Fujishima, A.; Honda, K. Electrochemical Photolysis of Water at a Semiconductor Electrode. *Nature* **1972**, *238*, 37–38. https://doi.org/10.1038/238037a0.

(17) Nakata, K.; Fujishima, A. TiO2 Photocatalysis: Design and Applications. *J. Photochem. Photobiol. C Photochem. Rev.* **2012**, *13* (3), 169–189. https://doi.org/10.1016/j.jphotochemrev.2012.06.001.

(18) Dijkstra, M. F. .; Michorius, A.; Buwalda, H.; Panneman, H. .; Winkelman, J. G. .; Beenackers, A. A. C. . Comparison of the Efficiency of Immobilized and Suspended Systems in Photocatalytic Degradation. *Catal. Today* **2001**, *66* (2–4), 487–494. https://doi.org/10.1016/S0920-5861(01)00257-7.

(19) McCullagh, C.; Skillen, N.; Adams, M.; Robertson, P. K. J. Photocatalytic Reactors for Environmental Remediation: A Review. *J. Chem. Technol. Biotechnol.* **2011**, *86* (8), 1002–1017. https://doi.org/10.1002/jctb.2650.

(20) Heggo, D.; Ookawara, S. Multiphase Photocatalytic Microreactors. *Chem. Eng. Sci.* **2017**, *169*, 67–77. https://doi.org/10.1016/j.ces.2017.01.019.

(21) Wang, N.; Zhang, X.; Chen, B.; Song, W.; Chan, N. Y.; Chan, H. L. W. Microfluidic Photoelectrocatalytic Reactors for Water Purification with an Integrated Visible-Light Source. *Lab Chip* **2012**, *12* (20), 3983–3990. https://doi.org/10.1039/c2lc40428a.

(22) Wang, N.; Zhang, X.; Wang, Y.; Yu, W.; Chan, H. L. W. Microfluidic Reactors for Photocatalytic Water Purification. *Lab Chip* **2014**, *14* (6), 1074–1082. https://doi.org/10.1039/C3LC51233A.

(23) de Sá, D. S.; Vasconcellos, L. E.; de Souza, J. R.; Marinkovic, B. A.; Del Rosso, T.; Fulvio, D.; Maza, D.; Massi, A.; Pandoli, O. Intensification of Photocatalytic Degradation of Organic Dyes and Phenol by Scale-up and Numbering-up of Meso- and Microfluidic TiO2 Reactors for Wastewater Treatment. *J. Photochem.*

Photobiol. A Chem. **2018**, *364*, 59–75. https://doi.org/10.1016/J.JPHOTOCHEM.2018.05.020.

(24) Lindstrom, H.; Wootton, R.; Iles, A. High Surface Area Titania Photocatalytic Microfluidic Reactors. *AIChE J.* **2007**, *53* (3), 695–702. https://doi.org/10.1002/aic.11096.

(25) Zhao, P.; Qin, N.; Wen, J. Z.; Ren, C. L. Photocatalytic Performances of ZnO Nanoparticle Film and Vertically Aligned Nanorods in Chamber-Based Microfluidic Reactors: Reaction Kinetics and Flow Effects. *Appl. Catal. B Environ.* **2017**, *209*, 468–475. https://doi.org/10.1016/J.APCATB.2017.03.020.

(26) Meng, Z.; Zhang, X.; Qin, J. A High Efficiency Microfluidic-Based Photocatalytic Microreactor Using Electrospun Nanofibrous TiO2 as a Photocatalyst. *Nanoscale* **2013**, *5* (11), 4687–4690. https://doi.org/10.1039/c3nr00775h.

(27) He, Z.; Li, Y.; Zhang, Q.; Wang, H. Capillary Microchannel-Based Microreactors with Highly Durable ZnO/TiO2 Nanorod Arrays for Rapid, High Efficiency and Continuous-Flow Photocatalysis. *Appl. Catal. B Environ.* **2010**, *93* (3–4), 376–382. https://doi.org/10.1016/J.APCATB.2009.10.011.

(28) Takei, G.; Kitamori, T.; Kim, H.-B. Photocatalytic Redox-Combined Synthesis of l-Pipecolinic Acid with a Titania-Modified Microchannel Chip. *Catal. Commun.* **2005**, *6* (5), 357–360. https://doi.org/10.1016/J.CATCOM.2005.02.010.

(29) Lei, L.; Wang, N.; Zhang, X. M.; Tai, Q.; Tsai, P.; Chan, H. L. W.; Tsai, D. P. Optofluidic Planar Reactors for Photocatalytic Water Treatment Using Solar Energy. *Cit. Biomicrofluidics* **2010**, *4* (4), 043004. https://doi.org/10.1063/1.3491471.

(30) Lee, S.-Y.; Park, S.-J. TiO2 Photocatalyst for Water Treatment Applications. *J. Ind. Eng. Chem.* **2013**, *19* (6), 1761–1769. https://doi.org/10.1016/J.JIEC.2013.07.012.

(31) Nowotny, M. K.; Bogdanoff, P.; Dittrich, T.; Fiechter, S.; Fujishima, A.; Tributsch, H. Observations of P-Type Semiconductivity in Titanium Dioxide at Room Temperature. *Mater. Lett.* **2010**, *64* (8), 928–930. https://doi.org/10.1016/J.MATLET.2010.01.061.

(32) Diebold, U. The Surface Science of Titanium Dioxide. *Surf. Sci. Rep.* **2003**, *48* (5–8), 53–229. https://doi.org/10.1016/S0167-5729(02)00100-0.

(33) Luttrell, T.; Halpegamage, S.; Tao, J.; Kramer, A.; Sutter, E.; Batzill, M. Why Is Anatase a Better Photocatalyst than Rutile? - Model Studies on Epitaxial TiO2 Films. *Sci. Rep.* **2014**, *4*, 4043. https://doi.org/10.1038/srep04043.

(34) Ahmad, H.; Kamarudin, S. K.; Minggu, L. J.; Kassim, M. Hydrogen from Photo-Catalytic Water Splitting Process: A Review. *Renew. Sustain. Energy Rev.* **2015**, *43*, 599–610. https://doi.org/10.1016/j.rser.2014.10.101.

(35) Eranna, G.; Joshi, B. C.; Runthala, D. P.; Gupta, R. P. Oxide Materials for Development of Integrated Gas Sensors—A Comprehensive Review. *Crit. Rev. Solid State Mater. Sci.* **2004**, *29* (3–4), 111–188. https://doi.org/10.1080/10408430490888977.

(36) Carp, O.; Huisman, C. L.; Reller, A. Photoinduced Reactivity of Titanium Dioxide. *Prog. Solid State Chem.* **2004**, *32*, 33–177. https://doi.org/10.1016/j.progsolidstchem.2004.08.001.

(37) J. Frank, A.; Kopidakis, N.; Lagemaat, J. van de. Electrons in Nanostructured TiO2 Solar Cells: Transport, Recombination and Photovoltaic Properties. *Coord. Chem. Rev.* **2004**, *248*, 1165–1179. https://doi.org/10.1016/J.CCR.2004.03.015.

(38) Chen, J. S.; Tan, Y. L.; Li, C. M.; Cheah, Y. L.; Luan, D.; Madhavi, S.; Boey, F. Y. C.; Archer, L. A.; Lou, X. W. Constructing Hierarchical Spheres from Large Ultrathin Anatase TiO 2 Nanosheets with Nearly 100% Exposed (001) Facets for Fast Reversible Lithium Storage. *J. Am. Chem. Soc.* **2010**, *132* (17), 6124–6130. https://doi.org/10.1021/ja100102y.

(39) Fan, R.; Chen, X.; Wang, Z.; Custer, D.; Wan, J. Flow-Regulated Growth of Titanium Dioxide (TiO_2) Nanotubes in Microfluidics. *Small* **2017**, *13* (30), 1701154. https://doi.org/10.1002/smll.201701154.

(40) Jayamohan, H.; Smith, Y. R.; Gale, B. K.; Mohanty, S. K.; Misra, M. Photocatalytic Microfluidic Reactors Utilizing Titania Nanotubes on Titanium Mesh for Degradation of Organic and Biological Contaminants. *J. Environ. Chem. Eng.* **2016**, *4* (1), 657–663. https://doi.org/10.1016/j.jece.2015.12.018.

(41) Cao, F.; Xiong, J.; Wu, F.; Liu, Q.; Shi, Z.; Yu, Y.; Wang, X.; Li, L. Enhanced Photoelectrochemical Performance from Rationally Designed Anatase/Rutile TiO 2 Heterostructures. *ACS Appl. Mater. Interfaces* **2016**, *8* (19), 12239–12245. https://doi.org/10.1021/acsami.6b03842.

(42) Lv, M.; Zheng, D.; Ye, M.; Xiao, J.; Guo, W.; Lai, Y.; Sun, L.; Lin, C.; Zuo, J. Optimized Porous Rutile TiO2 Nanorod Arrays for Enhancing the Efficiency of Dye-Sensitized Solar Cells. *Energy Environ. Sci.* **2013**, *6*, 1615–1622. https://doi.org/10.1039/c3ee24125d.

(43) Xie, Y.; Wu, Z.; Wu, Q.; Liu, M.; Piao, L. Effect of Different Base Structures on the Performance of the Hierarchical TiO2 Photocatalysts. *Catal. Today* **2014**, *225*, 74–79. https://doi.org/10.1016/j.cattod.2013.11.025.

(44) Pelaez, M.; Nolan, N. T.; Pillai, S. C.; Seery, M. K.; Falaras, P.; Kontos, A. G.; Dunlop, P. S. M.; Hamilton, J. W. J.; Byrne, J. A.; O'Shea, K.; et al. A Review on the Visible Light Active Titanium Dioxide Photocatalysts for Environmental Applications. *Appl. Catal. B Environ.* **2012**, *125*, 331–349. https://doi.org/10.1016/j.apcatb.2012.05.036.

(45) Wang, N.; Lei, L.; Zhang, X. M.; Tsang, Y. H.; Chen, Y.; Chan, H. L. W. A Comparative Study of Preparation Methods of Nanoporous TiO2 Films for Microfluidic Photocatalysis. *Microelectron. Eng.* **2011**, *88* (8), 2797–2799. https://doi.org/10.1016/J.MEE.2010.12.051.

(46) Jayamohan, H.; Smith, Y. R.; Hansen, L. C.; Mohanty, S. K.; Gale, B. K.; Misra, M. Anodized Titania Nanotube Array Microfluidic Device for Photocatalytic Application: Experiment and Simulation. *Appl. Catal. B Environ.* **2015**, *174–175* (February), 167–175. https://doi.org/10.1016/j.apcatb.2015.02.041.

(47) Li, L.; Tang, D.; Song, Y.; Jiang, B. Dual-Film Optofluidic Microreactor with Enhanced Light-Harvesting for Photocatalytic Applications. *Chem. Eng. J.* **2018**, *339*, 71–77. https://doi.org/10.1016/J.CEJ.2018.01.074.

(48) Wu, J.-M.; Hayakawa, S.; Tsuru, K.; Osaka, A. Porous Titania Films Prepared from Interactions of Titanium with Hydrogen Peroxide Solution. *Scr. Mater.* **2002**, *46* (1), 101–106. https://doi.org/10.1016/S1359-6462(01)01207-6.

(49) DeRosa, D. M.; Zuruzi, A. S.; MacDonald, N. C. Formation of Nanostructured Titania: Effect of Thickness on Oxidation Kinetics of Titanium Thin Films in Aqueous Hydrogen Peroxide. *Adv. Eng. Mater.* **2006**, *8* (1–2), 77–80. https://doi.org/10.1002/adem.200500186.

(50) Wu, J.-M. Low-Temperature Preparation of Titania Nanorods through Direct Oxidation of Titanium with Hydrogen Peroxide. *J. Cryst. Growth* **2004**, *269* (2–4), 347–355. https://doi.org/10.1016/j.jcrysgro.2004.05.023.

(51) Wu, J.-M. Photodegradation of Rhodamine B in Water Assisted by Titania Nanorod Thin Films Subjected to Various Thermal Treatments. *Environ. Sci. Technol.* **2007**, *41* (5), 1723–1728.

(52) Wu, J.-M.; Xue, H.-X. Photocatalytic Active Titania Nanowire Arrays on Ti Substrates. *J. Am. Ceram. Soc.* **2009**, *92* (9), 2139–2143. https://doi.org/10.1111/j.1551-2916.2009.03153.x.

(53) Zuruzi, A. S.; MacDonald, N. C. Facile Fabrication and Integration of Patterned Nanostructured TiO2 for Microsystems Applications. *Adv. Funct. Mater.* **2005**, *15* (3), 396–402. https://doi.org/10.1002/adfm.200400135.

(54) Zuruzi, A. S.; Kolmakov, A.; MacDonald, N. C.; Moskovits, M. Highly Sensitive Gas Sensor Based on Integrated Titania Nanosponge Arrays. *Appl. Phys. Lett.* **2006**, *88* (10), 102904. https://doi.org/10.1063/1.2185247.

(55) Zuruzi, A. S.; MacDonald, N. C.; Moskovits, M.; Kolmakov, A. Metal Oxide "Nanosponges" as Chemical Sensors: Highly Sensitive Detection of Hydrogen with Nanosponge Titania. *Angew. Chemie* **2007**, *119* (23), 4376–4379. https://doi.org/10.1002/ange.200700006.

(56) Zuruzi, A. S.; Nurmawati, M. H.; Yeo, Y. H.; Wu, S.; Chee Hoong Lai, P.; Chen, Z. A Simple Strategy to Incorporate Pt into TiO2 Nanosponges via Wet Oxidation of Multilayered Films. *RSC Adv.* **2013**, *3*, 19971–19977. https://doi.org/10.1039/c3ra41162a.

(57) Zuruzi, A. S.; Gardner, H. C.; Monkowski, A. J.; MacDonald, N. C. Tailored Nanostructured Titania Integrated on Titanium Micropillars with Outstanding Wicking Properties. *Lab Chip* **2013**, *13* (12), 2414–2418. https://doi.org/10.1039/c3lc50098e.

(58) Song, X.-M.; Wu, J.-M.; Yan, M. Photocatalytic Degradation of Selected Dyes by Titania Thin Films with Various Nanostructures. *Thin Solid Films* **2009**, *517* (15), 4341–4347. https://doi.org/10.1016/j.tsf.2009.02.132.

(59) Ao, Y.; Gao, Y.; Wang, P.; Wang, C.; Hou, J.; Qian, J. Investigation on Preparation and Photocatalytic Activity of TiO2 Nanosheet Film on Ti Substrate. *Mater. Lett.* **2013**, *102–103*, 36–38. https://doi.org/10.1016/j.matlet.2013.03.101.

(60) Ao, Y.; Gao, Y.; Wang, P.; Wang, C.; Hou, J.; Qian, J. Solvent-Controlled Preparation and Photocatalytic Properties of Nanostructured {TiO}2 Thin Films with Different Morphologies. *Mater. Res. Bull.* **2014**, *49*, 223–228. https://doi.org/10.1016/j.materresbull.2013.09.002.

(61) Khandan, O.; Kahook, M. Y.; Rao, M. P. Fenestrated Microneedles for Ocular Drug Delivery. *Sensors Actuators B Chem.* **2016**, *223*, 15–23. https://doi.org/10.1016/j.snb.2015.09.071.

(62) Long, M.; Rack, H. . Titanium Alloys in Total Joint Replacement—a Materials Science Perspective. *Biomaterials* **1998**, *19* (18), 1621–1639. https://doi.org/10.1016/S0142-9612(97)00146-4.

(63) Boyer, R. R. An Overview on the Use of Titanium in the Aerospace Industry. *Mater. Sci. Eng. A* **1996**, *213* (1–2), 103–114. https://doi.org/10.1016/0921-5093(96)10233-1.

(64) Spearing, S. . Materials Issues in Microelectromechanical Systems (MEMS). *Acta*

Mater. **2000**, *48* (1), 179–196. https://doi.org/10.1016/S1359-6454(99)00294-3.

(65) Wang, S.; Zhou, C.; Ru, H.; Zhang, Y. Optimized Condition for Etching Fused-Silica Phase Gratings with Inductively Coupled Plasma Technology. *Appl. Opt.* **2005**, *44* (21), 4429–4434.

(66) Horiike, Y. High Rate and Highly Selective SiO2 Etching Employing Inductively Coupled Plasma and Discussion on Reaction Kinetics. *J. Vac. Sci. Technol. A Vacuum, Surfaces, Film.* **1995**, *13* (3), 801–809. https://doi.org/10.1116/1.579831.

(67) Parker, E. R.; Rao, M. P.; Turner, K. L.; Meinhart, C. D.; Macdonald, N. C. Bulk Micromachined Titanium Microneedles. *J. MICROELECTROMECHANICAL Syst.* **2007**, *16* (2), 289–295. https://doi.org/10.1109/JMEMS.2007.892909.

(68) Aimi, M. F.; Rao, M. P.; MacDonald, N. C.; Zuruzi, A. S.; Bothman, D. P. High-Aspect-Ratio Bulk Micromachining of Titanium. *Nat. Mater.* **2004**, *3* (2), 103–105. https://doi.org/10.1038/nmat1058.

(69) Parker, E. R.; Thibeault, B. J.; Aimi, M. F.; Rao, M. P.; Macdonald, N. C. Inductively Coupled Plasma Etching of Bulk Titanium for MEMS Applications. *J. Electrochem. Soc.* **2005**, *152* (10), C675–C683. https://doi.org/10.1149/1.2006647.

(70) Woo, B. W. K.; Gott, S. C.; Peck, R. A.; Yan, D.; Rommelfanger, M. W.; Rao, M. P. Ultrahigh Resolution Titanium Deep Reactive Ion Etching. *ACS Appl. Mater. Interfaces* **2017**, *9* (23), 20161–20168. https://doi.org/10.1021/acsami.6b16518.

(71) Lu, J.; Rao, M. P.; MacDonald, N. C.; Khang, D.; Webster, T. J. Improved Endothelial Cell Adhesion and Proliferation on Patterned Titanium Surfaces with Rationally Designed, Micrometer to Nanometer Features. *Acta Biomater.* **2008**, *4* (1), 192–201. https://doi.org/10.1016/j.actbio.2007.07.008.

(72) Gott, S. C.; Jabola, B. A.; Rao, M. P. Vascular Stents with Submicrometer-Scale Surface Patterning Realized via Titanium Deep Reactive Ion Etching. *J. Micromechanics Microengineering* **2015**, *25* (8), 085016. https://doi.org/10.1088/0960-1317/25/8/085016.

(73) Khandan, O.; Stark, D.; Chang, A.; Rao, M. P. Wafer-Scale Titanium Anodic Bonding for Microfluidic Applications. *Sensors Actuators B Chem.* **2014**, *205*, 244–248. https://doi.org/10.1016/j.snb.2014.08.083.

(74) Li, L.; Chen, R.; Zhu, X.; Wang, H.; Wang, Y.; Liao, Q.; Wang, D. Optofluidic Microreactors with TiO $_2$ -Coated Fiberglass. *ACS Appl. Mater. Interfaces* **2013**, *5* (23), 12548–12553. https://doi.org/10.1021/am403842b.

(75) Meng, Z.; Zhang, X.; Qin, J. A High Efficiency Microfluidic-Based Photocatalytic

Microreactor Using Electrospun Nanofibrous TiO2 as a Photocatalyst. *Nanoscale* **2013**, *5* (11), 4687–4690. https://doi.org/10.1039/c3nr00775h.

(76) Lin, C.; Liu, M.; Yang, Z. Performance of a Metal Ion-Doped Titania-Coated Planar Photocatalytic Microreactor. *Chem. Eng. Technol.* **2016**, *39* (1), 88–96. https://doi.org/10.1002/ceat.201400776.

(77) Yusuf, A.; Garlisi, C.; Palmisano, G. Overview on Microfluidic Reactors in Photocatalysis: Applications of Graphene Derivatives. *Catal. Today* **2018**, *315*, 79–92. https://doi.org/10.1016/j.cattod.2018.05.041.

(78) Naghibi, S.; Faghihi Sani, M. A.; Madaah Hosseini, H. R. Application of the Statistical Taguchi Method to Optimize TiO2 Nanoparticles Synthesis by the Hydrothermal Assisted Sol–Gel Technique. *Ceram. Int.* **2014**, *40* (3), 4193–4201. https://doi.org/10.1016/j.ceramint.2013.08.077.

(79) Duran, J. E.; Mohseni, M.; Taghipour, F. Design Improvement of Immobilized Photocatalytic Reactors Using a CFD-Taguchi Combined Method. *Ind. Eng. Chem. Res.* **2011**, *50* (2), 824–831. https://doi.org/10.1021/ie101736d.

(80) Lin, W.-C.; Yang, W.-D.; Jheng, S.-Y. Photocatalytic Degradation of Dyes in Water Using Porous Nanocrystalline Titanium Dioxide. *J. Taiwan Inst. Chem. Eng.* **2012**, *43* (2), 269–274. https://doi.org/10.1016/j.jtice.2011.10.010.

(81) Chong, M. N.; Jin, B.; Chow, C. W. K.; Saint, C. P. A New Approach to Optimise an Annular Slurry Photoreactor System for the Degradation of Congo Red: Statistical Analysis and Modelling. *Chem. Eng. J.* **2009**, *152* (1), 158–166. https://doi.org/10.1016/j.cej.2009.04.027.

(82) Chong, M. N.; Jin, B.; Chow, C. W. K.; Saint, C. Recent Developments in Photocatalytic Water Treatment Technology: A Review. *Water Res.* **2010**, *44* (10), 2997–3027. https://doi.org/10.1016/j.watres.2010.02.039.

(83) Zuruzi, A. S.; Yeo, Y. H.; Monkowski, A. J.; Ding, C. S.; MacDonald, N. C. Superhydrophilicity on Microstructured Titanium Surfaces via a Superficial Titania Layer with Interconnected Nanoscale Pores. *Nanotechnology* **2013**, *24* (24), 245304. https://doi.org/10.1088/0957-4484/24/24/245304.

(84) Monkowski, A. J. *Microfabricated Structures and Devices Featuring Nanostructured Titania Thin Films*; ProQuest, 2007.

(85) Haq, A. N.; Marimuthu, P.; Jeyapaul, R. Multi Response Optimization of Machining Parameters of Drilling Al/SiC Metal Matrix Composite Using Grey Relational Analysis in the Taguchi Method. *Int. J. Adv. Manuf. Technol.* **2008**, *37* (3–4), 250–255. https://doi.org/10.1007/s00170-007-0981-4.

(86) Houas, A.; Lachheb, H.; Ksibi, M.; Elaloui, E.; Guillard, C.; Herrmann, J.-M. Photocatalytic Degradation Pathway of Methylene Blue in Water. *Appl. Catal. B Environ.* **2001**, *31* (2), 145–157. https://doi.org/10.1016/S0926-3373(00)00276-9.

(87) Kwon, C. H.; Shin, H.; Kim, J. H.; Choi, W. S.; Yoon, K. H. Degradation of Methylene Blue via Photocatalysis of Titanium Dioxide. *Mater. Chem. Phys.* **2004**, *86* (1), 78–82. https://doi.org/10.1016/j.matchemphys.2004.02.024.

(88) Gnaser, H.; Savina, M. R.; Calaway, W. F.; Tripa, C. E.; Veryovkin, I. V; Pellin, M. J. Photocatalytic Degradation of Methylene Blue on Nanocrystalline TiO2: Surface Mass Spectrometry of Reaction Intermediates. *Int. J. Mass Spectrom.* **2005**, *245* (1–3), 61–67. https://doi.org/10.1016/j.ijms.2005.07.003.

(89) Zhao, Y.; Zhang, X.; Zhai, J.; He, J.; Jiang, L.; Liu, Z.; Nishimoto, S.; Murakami, T.; Fujishima, A.; Zhu, D. Enhanced Photocatalytic Activity of Hierarchically Micro-/Nano-Porous TiO2 Films. *Appl. Catal. B Environ.* **2008**, *83* (1–2), 24–29. https://doi.org/10.1016/j.apcatb.2008.01.035.

(90) Gaya, U. I.; Abdullah, A. H. Heterogeneous Photocatalytic Degradation of Organic Contaminants over Titanium Dioxide: A Review of Fundamentals, Progress and Problems. *J. Photochem. Photobiol. C Photochem. Rev.* **2008**, *9* (1), 1–12. https://doi.org/10.1016/j.jphotochemrev.2007.12.003.

(91) Schneider, C. A.; Rasband, W. S.; Eliceiri, K. W. NIH Image to ImageJ: 25 Years of Image Analysis. *Nat. Methods* **2012**, *9* (7), 671–675. https://doi.org/10.1038/nmeth.2089.

(92) Hall, M.; Frank, E.; Holmes, G.; Pfahringer, B.; Reutemann, P.; Witten, I. H. The WEKA Data Mining Software. *ACM SIGKDD Explor. Newsl.* **2009**, *11* (1), 10–18. https://doi.org/10.1145/1656274.1656278.

(93) Jeyapaul, R.; Shahabudeen, P.; Krishnaiah, K. Quality Management Research by Considering Multi-Response Problems in the Taguchi Method – a Review. *Int. J. Adv. Manuf. Technol.* **2005**, *26* (11–12), 1331–1337. https://doi.org/10.1007/s00170-004-2102-y.

(94) Fung, C.-P. Manufacturing Process Optimization for Wear Property of Fiber-Reinforced Polybutylene Terephthalate Composites with Grey Relational Analysis. *Wear* **2003**, *254* (3–4), 298–306. https://doi.org/10.1016/S0043-1648(03)00013-9.

(95) Kuo, Y.; Yang, T.; Huang, G.-W. The Use of a Grey-Based Taguchi Method for Optimizing Multi-Response Simulation Problems. *Eng. Optim.* **2008**, *40* (6), 517–528. https://doi.org/10.1080/03052150701857645.

(96) Wu, J.-M.; Qi, B. Low-Temperature Growth of a Nitrogen-Doped Titania

Nanoflower Film and Its Ability To Assist Photodegradation of Rhodamine B in Water. *J. Phys. Chem. C* **2007**, *111* (2), 666–673. https://doi.org/10.1021/jp065630n.

(97) Lin, J. .; Lin, C. . The Use of the Orthogonal Array with Grey Relational Analysis to Optimize the Electrical Discharge Machining Process with Multiple Performance Characteristics. *Int. J. Mach. Tools Manuf.* **2002**, *42* (2), 237–244. https://doi.org/10.1016/S0890-6955(01)00107-9.

(98) Su, T.-L.; Kuo, Y.-L.; Wu, T.-J.; Kung, F.-C. Experimental Analysis and Optimization of the Synthesizing Property of Nitrogen-Modified TiO2 Visible-Light Photocatalysts. *J. Chem. Technol. Biotechnol.* **2012**, *87* (1), 160–164. https://doi.org/10.1002/jctb.2702.

(99) Liao, W.; Wang, N.; Wang, T.; Xu, J.; Han, X.; Liu, Z.; Zhang, X.; Yu, W. Biomimetic Microchannels of Planar Reactors for Optimized Photocatalytic Efficiency of Water Purification. *Biomicrofluidics* **2016**, *10* (1), 014123. https://doi.org/10.1063/1.4942947.

(100) Vangelooven, J.; De Malsche, W.; De Beeck, J. O.; Eghbali, H.; Gardeniers, H.; Desmet, G. Design and Evaluation of Flow Distributors for Microfabricated Pillar Array Columns. *Lab Chip* **2010**, *10* (3), 349–356. https://doi.org/10.1039/B916126K.

(101) Mills, A. An Overview of the Methylene Blue ISO Test for Assessing the Activities of Photocatalytic Films. *Appl. Catal. B Environ.* **2012**, *128*, 144–149. https://doi.org/10.1016/J.APCATB.2012.01.019.

(102) Fernández-Pérez, A.; Rodríguez-Casado, V.; Valdés-Solís, T.; Marbán, G. A New Continuous Flow-through Structured Reactor for the Photodegradation of Aqueous Contaminants. *J. Environ. Chem. Eng.* **2018**, *6* (4), 4070–4077. https://doi.org/10.1016/J.JECE.2018.06.018.

(103) Zeghioud, H.; Khellaf, N.; Djelal, H.; Amrane, A.; Bouhelassa, M. Photocatalytic Reactors Dedicated to the Degradation of Hazardous Organic Pollutants: Kinetics, Mechanistic Aspects, and Design – A Review. *Chem. Eng. Commun.* **2016**, *203* (11), 1415–1431. https://doi.org/10.1080/00986445.2016.1202243.

(104) Moan, J. Visible Light and UV Radiation. *Radiat. Home, Outdoors Work.* **2001**, *Oslo: Scan*, 69–85.

(105) Eskandarloo, H.; Badiei, A.; Behnajady, M. A.; Ziarani, G. M. UV-LEDs Assisted Preparation of Silver Deposited TiO2 Catalyst Bed inside Microchannels as a High Efficiency Microphotoreactor for Cleaning Polluted Water. *Chem. Eng. J.* **2015**, *270*, 158–167. https://doi.org/10.1016/j.cej.2015.01.117.

(106) Wang, C.; Wang, M.; Xie, K.; Wu, Q.; Sun, L.; Lin, Z.; Lin, C. Room Temperature One-Step Synthesis of Microarrays of N-Doped Flower-like Anatase TiO2 Composed of Well-Defined Multilayer Nanoflakes by Ti Anodization. *Nanotechnology* **2011**, *22* (30), 305607. https://doi.org/10.1088/0957-4484/22/30/305607.

(107) Khandan, O.; Stark, D.; Chang, A.; Rao, M. P. Wafer-Scale Titanium Anodic Bonding for Microfluidic Applications. *Sensors Actuators B. Chem.* **2014**, *205*, 244–248. https://doi.org/10.1016/j.snb.2014.08.083.

(108) Muggli, D. S.; McCue, J. T.; Falconer, J. L. Mechanism of the Photocatalytic Oxidation of Ethanol on TiO2. *J. Catal.* **1998**, *173* (2), 470–483. https://doi.org/10.1006/JCAT.1997.1946.

(109) Westerhoff, P.; Alvarez, P.; Li, Q.; Gardea-Torresdey, J.; Zimmerman, J. Overcoming Implementation Barriers for Nanotechnology in Drinking Water Treatment. *Environ. Sci. Nano* **2016**, *3* (6), 1241–1253. https://doi.org/10.1039/C6EN00183A.

(110) Li, Q.; Mahendra, S.; Lyon, D. Y.; Brunet, L.; Liga, M. V.; Li, D.; Alvarez, P. J. J. Antimicrobial Nanomaterials for Water Disinfection and Microbial Control: Potential Applications and Implications. *Water Res.* **2008**, *42* (18), 4591–4602. https://doi.org/10.1016/j.watres.2008.08.015.

(111) Foster, H. A.; Ditta, I. B.; Varghese, S.; Steele, A. Photocatalytic Disinfection Using Titanium Dioxide: Spectrum and Mechanism of Antimicrobial Activity. *Appl Microbiol Biotechnol* **2011**, *90* (6), 1847–1868. https://doi.org/10.1007/s00253-011-3213-7.

(112) Kingsley, D. H.; Fay, J. P.; Calci, K.; Pouillot, R.; Woods, J.; Chen, H.; Niemira, B. A.; Doren, J. M. Van. Evaluation of Chlorine Treatment Levels for Inactivation of Human Norovirus and MS2 Bacteriophage during Sewage Treatment. *Appl. Environ. Microbiol.* **2017**, *83* (23), e01270-17. https://doi.org/10.1128/AEM.01270-17.

(113) Liga, M. V.; Bryant, E. L.; Colvin, V. L.; Li, Q. Virus Inactivation by Silver Doped Titanium Dioxide Nanoparticles for Drinking Water Treatment. *Water Res.* **2011**, *45* (2), 535–544. https://doi.org/10.1016/J.WATRES.2010.09.012.

(114) Venieri, D.; Gounaki, I.; Binas, V.; Zachopoulos, A.; Kiriakidis, G. Inactivation of MS2 Coliphage in Sewage by Solar Photocatalysis Using Metal-Doped TiO2. *Appl. Catal. B Environ.* **2015**, *178*, 54–64. https://doi.org/10.1016/J.APCATB.2014.10.052.

7 APPENDICES

Appendix A – ERSATZ

Compound	Load (mg/L)	TOC (mg/L)
Acetaldehyde	2.74	1.49
Acetone	4.4	2.73
Ethanol	39.2	20.44
Methanol	7.94	2.98
Propylene Glycol	35.4	16.76
Ethylene Glycol	5.5	2.13
Formaldehyde	5.9	2.36
1-propanol	0.45	0.27
2-propanol	1.6	0.96
1-butanol	1.5	0.97
Formic acid	49.9	13.02
Urea	3.55	0.71
TOC (ppm)	-	**64.82**

Table A.1. Table of goal Ersatz feed for Type III Challenge Load.[4]

The thermal catalytic oxidation reactor operates at temperatures of 265˚F, requiring high pressure to prevent the water from boiling during oxidation of VOC contaminants. Studies have been conducted to lower the operating temperature which would decrease stress on the catalytic reactor and surrounding components. To emulate the VOC concentrations typically processed on the ISS, NASA and Hamilton Sundstrand (HS) developed the Ersatz solution. Table A.1 is the Type III challenge feed of the Ersatz solution that was used to test alternative low temperature catalytic oxidation reactors. The Type III challenge feed includes ethanol and 2-propanol, which have similar oxidation mechanics as the VOCs found on the ISS, and it includes other compounds such as formic acid and urea. The TOC concentration of the Type III challenge feed is 64.82 ppm, roughly twice that of the Type I and II feeds.[4] Degradation of the Type III challenge feed is the most difficult test for validating replacement catalytic devices.

Appendix B – XRD of NPT

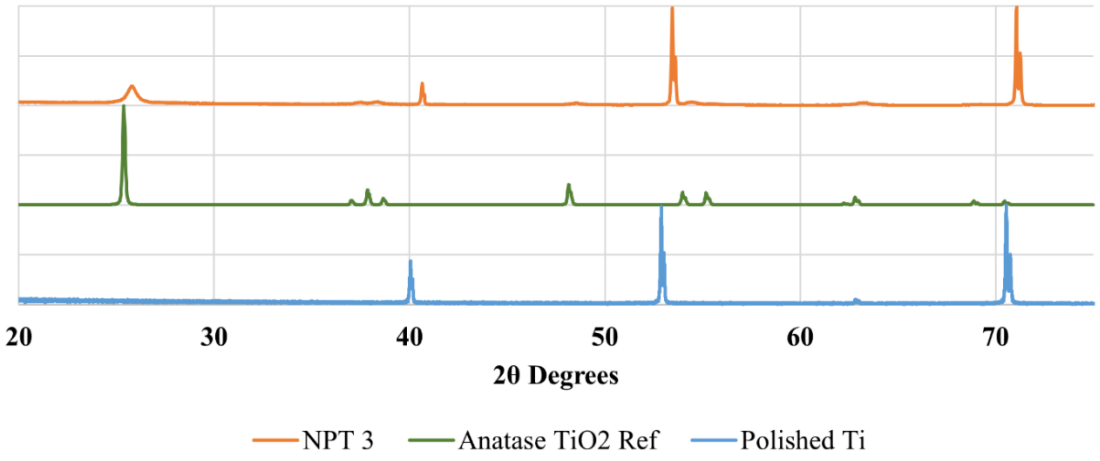

Figure B.1. XRD of the NPT with the highest overall reaction rate constant, NPT 3, compared to an Anatase TiO_2 reference (JCPDS 01-89-4921), and polished titanium. Each spectra was normalized between 0 and 1.

The XRD plot, seen in Figure B.1, was used to compare the crystallinity of NPT to a TiO_2 Anatase reference (JCPDS 01-89-4921). A distinct anatase peak in the NPT and reference spectra can be seen at 25.4˚, this is the main indicator of the presence of anatase TiO_2 in the NPT. There are three noticeable Ti peaks at 40.2˚, 53.0˚, and 70.7˚ in the NPT spectra, this was detected from the underlying Ti substrate. There is also a small peak shift between the three spectra, that is easily noticeable at 25.4˚ and 53.0˚. The NPT spectra is shifted to the right compared to the TiO_2 reference and the polished Ti. The peak shift is most likely a result of an uneven NPT surface. Typically, XRD is conducted on powders so it is relatively simple to produce a flat surface for scanning, but NPT films are oxidized onto Ti foils. The foils used in this experiment were 320 μm thick and were slightly bowed due to the cutting process. A bowed foil would create an uneven surface for NPT oxidation

and may have caused the slight peak shift. Another possibility is that residual stress from the NPT oxidation process may have led to peak shifts.

Appendix C – NPT Comparison to P25

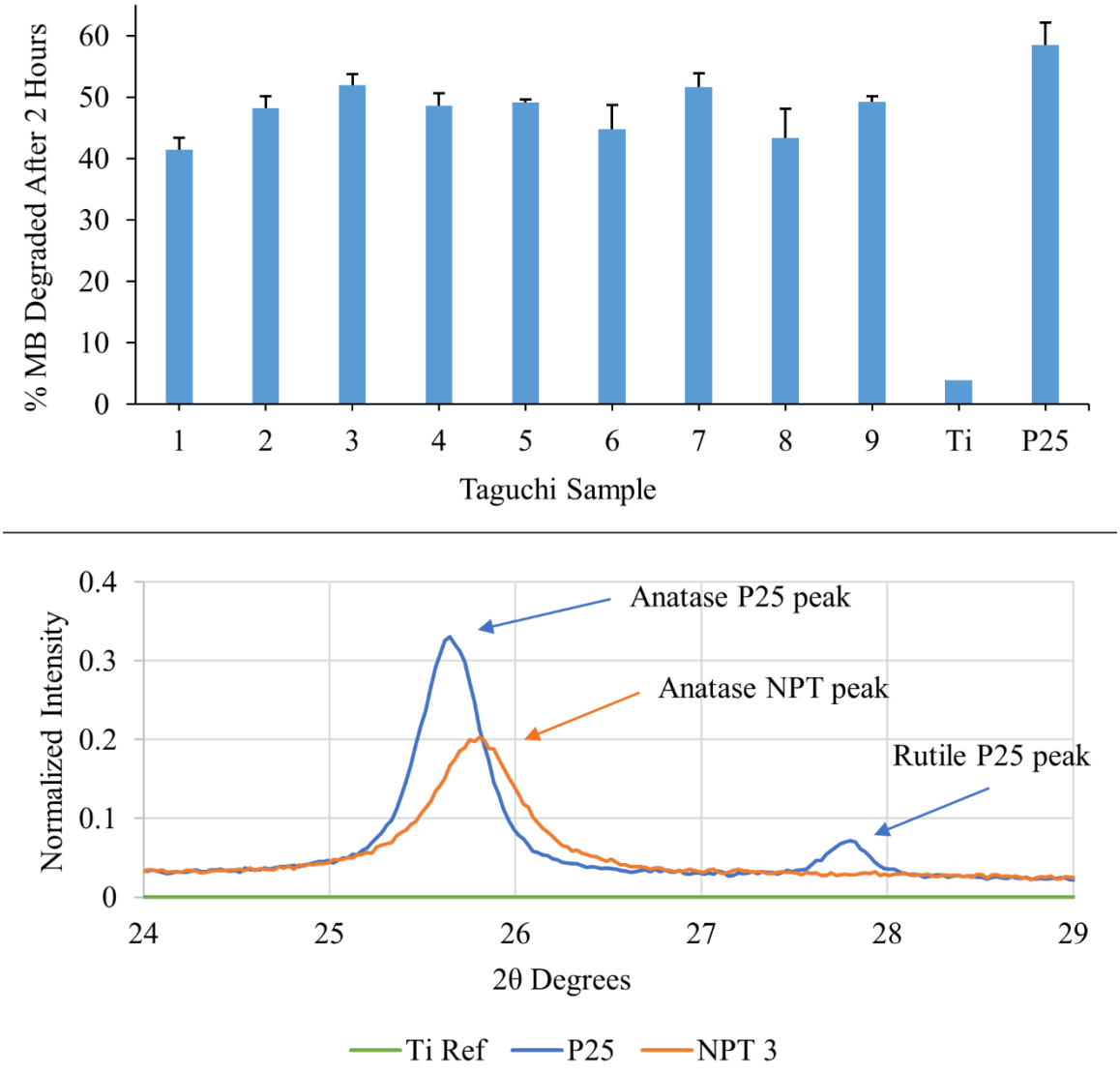

Figure C.1. *Top*: Plot of the percentage of MB degraded over two hours of UV light exposure, this is the same plot found in Figure 4.2a, however the degradation percentage of a P25 drop-cast sample has been included as well. *Bottom:* XRD of the drop-cast P25 sample and NPT 3, the Taguchi sample with the largest reaction rate constant.

P25 is the most commonly used TiO_2 photocatalyst, see Chapter 2 for more details on the use of P25 in literature. We hypothesized that P25 would have greater photocatalytic activity over NPT due to its ideal combination of anatase and rutile crystallinity, as well as its high surface area. A study was conducted with P25 to compare the photocatalytic performance of P25 nanoparticles to NPT. To determine the mass of P25 needed to make a direct comparison to NPT, BET (Brunauer-Emmett-Teller, ASAP 2020 Micromeritics Physiosorption Analyzer) surface area analysis was performed on the NPT sample with the largest *k*, NPT 3. BET uses N_2 adsorption to measure a specific surface area (m^2/g) for the mass analyzed. Typically, BET is conducted with powders, which have a high surface area to mass ratio, but measurements with thin films are possible if the mass of the adsorbing surface is known. For example, if a thin film is sputtered onto a substrate and the substrate is weighed before and after deposition, the difference in mass is the weight of the thin film. Due to the oxidation process for NPT, the true mass of NPT cannot be known so a real specific surface area cannot be measured. NPT 3 had a BET specific surface area of only 0.5895 ± 0.0053 m^2/g, this was because the mass of the analyzed NPT sample was 0.8355 g, nearly all of it being Ti. BET conducted on 0.1998 g of P25 (nanoparticle size of 120 nm) yielded a specific surface area of 50.1929 m^2/g. Without the extra weight of a substrate, the P25 powder had a much higher surface area. We cannot consider the BET measurement for NPT to be its real specific surface area because we do not know the mass contribution of NPT, therefore we cannot make a surface area comparison between P25 and NPT. BET was instead used to determine the mass of P25 required to produce a sample of the same surface area as NPT 3.

To fabricate a P25 sample with comparable surface area to NPT we multiplied the BET surface area of NPT by its mass. The resulting surface area was 0.4926 m^2 for a 1x1 in^2 double-sided NPT sample. To find the mass of NPT required to produce a sample with the same surface area we divided 0.4926 m^2 by the BET surface area of P25, which resulted in a mass of 9.81 mg. Finally, the mass of P25 was divided by two because only one side of the NPT is exposed to UV light in the bulk reactor setup. Therefore, 4.91 mg of P25 would yield a similar surface area to NPT 3. To create a P25 thin film for testing within the bulk reactor setup described in section 4.2.3, we drop-cast a colloidal solution of 4.91 mg P25 and 200 proof ethanol onto a 1x1 in^2 substrate. The P25 thin film was then annealed at 100˚C for 90 minutes to evaporate the ethanol and ensure strong adhesion of the P25 nanoparticles to the substrate.

The P25 thin film sample was tested in the same bulk reactor setup as the NPT in the optimization study from Chapter 4. P25 degraded 58.45 $\pm$ 3.73% of the MB, 6.47% more MB than NPT 3, over two hours of UV exposure. The *k* value for P25 was calculated to be 0.0074 min^{-1}, larger than the *k* for NPT 3, 0.0061 min^{-1}. This was expected due to the photocatalytically advantageous crystallinity of the P25 powder, which was verified by XRD seen in Figure C.1. The P25 spectra had a large anatase peak at 25.4˚, and a smaller rutile peak at 27.7˚. A comparison study between NPT and P25 in a PMFR setup was not conducted, but the novel NPT PMFR concept was compared to a conventional P25 planar microreactor from literature. In Chapter 5, we found that NPT, when used in a PMFR device, outperforms a conventional P25 thin film drop-cast onto the chamber floor of a planar reactor (see section 5.3.3).

To summarize, P25, when compared directly to NPT in a bulk reactor setup yielded greater photoactivity due to its ideal combination of anatase and rutile TiO_2. NPT still came close in photocatalytic performance and only degraded 6.5% less MB than P25 over a two-hour period. For use within PMFR systems, which was the intended application of the NPT parameter study, the unique material properties of NPT make it an advantageous material over P25. Though, a direct comparison between an NPT and P25 PMFR was not made within this study, the NPT PMFR device did show greater photocatalytic performance compared to other microreactors from the literature. The added surface area advantages of NPT and oxidation onto vertical features make it the superior alternative to P25 for use within PMFR devices, as demonstrated by the high activity of MP50.

Appendix D – Fabrication Procedures

D.1. NPT Oxidation for Bulk Reactor Applications

1. Cut Ti foil using metal snips
2. Ultrasonically clean Ti in Acetone, Isopropanol, and DI water for 5 minutes each
3. Wet Etch in 4.9% HF (200 ml of DI water and 20 ml of 49% HF) for 60 seconds
4. Rinse in ultrasonic DI water bath for 10 minutes
5. Submerge Ti foil in heated H_2O_2 at desired concentration, temperature, and time. To make the optimized conditions (10%, 80˚C, 5 hours) use 400 ml of H_2O and 200 ml of 30% H_2O_2 to produce a 10% H_2O_2 solution. Use a hotplate with a thermocouple probe to maintain a constant temperature of 80˚C.
6. After oxidation immediately place sample into water

7. Place sample from water directly into box oven and anneal in air at 300˚C for 8 hours with a slow ramp of 1˚C/min.

D.2. Microreactor Fabrication

Hard Mask Deposition

1. Clean single-side polished, grade 1, CP, Ti wafers (4”) with Acetone, Isopropanol, and DI water
2. Place Ti wafers, polished side face-up, within the PECVD (Plasmatherm 790) and deposit 4.8 μm of SiO_2

Wafer Preparation

1. Clean 4” Si wafers using Acetone, Isopropanol, and DI water
2. Dry completely
3. Completely cover the polished side of the Si wafer with 3M thermally conductive double-sided tape
4. Tape the Si wafer to the unpolished side of the Ti wafer
5. Clean the stacked wafers in Acetone, Isopropanol, and DI water
6. Dry stacked wafers with air
7. Heat stacked wafers on a hotplate at 115˚C for 5 minutes to evaporate remaining moisture between the two wafers

Stacked Wafer Dicing

1. Spin a thick layer of photoresist onto SiO_2 side of the stacked wafers
2. Do a dehydration bake on a 115˚C hotplate for 2 minutes

3. Dice wafer (Disco DAD 321 Automatic Dicing Saw: spindle speed 15000 rpm, feed speed 1.00 mm/s) into two 40 x 60 mm rectangular samples
4. Ultrasonically clean diced samples in Acetone, Isopropanol, DI water for 5 minutes each
5. Dry with air and do a dehydration bake on a hotplate at 115˚C for 5 minutes

Photolithography

1. Place samples (diced 40 x 60 mm stacked Ti and Si wafer samples) onto vacuum chuck at photolithography spin coater
2. Create two recipes for spinning A) HMDS, a resist adhesion promoter, and B) SPR 220-7.0.
    A. Spin Speed: 3000 rpm, Ramp: 600 rpm, Time: 30 seconds
    B. Spin Speed: 5000 rpm, Ramp: 1000 rpm, Time: 35 seconds
3. Use pipet to deposit HMDS onto sample and let it sit for 30 seconds
4. Spin HMDS using the conditions from recipe A
5. Wait 1 minute
6. Use pipet to deposit SPR 220-7.0
7. Spin SPR 220-7.0 using the conditions from recipe B
8. Let the sample sit for 5 minutes
9. Place sample onto hotplate at 115˚C for 2 minutes
10. Let sample cool then begin exposure
11. Expose using the mask aligner (Karl Suss MA-6 Mask Aligner, 34 seconds of exposure, 17.9 mW/cm^2 at 350 W power, Channel CP, hard contact)

12. Let sample sit for 20 minutes
13. Do a post-exposure bake for 2 minutes at 115˚C
14. Let sample cool prior to development
15. Develop photoresist in AZ 300 MIF developer solution
16. Let sample sit in developer for 75 seconds undisturbed, move to water bath and rinse for 20 seconds, then rinse under a light water spray for several seconds, dry using N_2 air gun
17. Examine under optical microscope and add cycles of 15-30 seconds of development time until only the desired pattern remains

SiO_2 Hard Mask Etch

1. Mount sample onto larger 4" Si carrier wafer using Santovac Oil
2. Etch sample for 40 minutes, several more minutes may be needed for the micropillar devices due to the feature size and close-proximity between micropillars (Oxford Cobra Plasmalab 100 – 1 Pa Pressure, 10 sccm C_4F_8, 2000 W ICP Power, 40 W RF Power, -20˚C)
3. Verify that all SiO_2 has been cleared using an optical microscope or SEM
4. Ultrasonically clean samples in Acetone, Isopropanol, and DI water for 3 minutes each to remove residual photoresist
    - After the Acetone sonication the sample can be gently swabbed with foam-tip swabs to wipe off remaining photoresist
5. Do a dehydration bake on a hotplate at 115˚C for 5 minutes

Ti Deep Reactive Ion Etch

Up to this point, the fabrication procedure for the micropillar and planar reactors has been identical. A different mask was used during exposure but there were no other changes to the processing conditions. Different plasma etchers were used for Ti DRIE of planar and micropillar devices. The UC Riverside Oxford Plasmalab 100 has a high-power ICP source and the recipe for Ti etching had not been fully refined for high aspect ratio features. Due to the aggressive nature of the etch brought on by the high ICP power, excessive passivation is needed to produce high aspect ratio features, such as micropillars. This passivation layer was difficult to remove without damaging the underlying Ti so the Panasonic E626I, with a more refined recipe, at UC Santa Barbara's Nanofabrication Facility was used for etching the micropillar devices. The Oxford system at UC Riverside was used to etch the planar devices. The Oxford Plasmalab system is capable of etching micropillar arrays but more process development will be required.

Ti DRIE for Planar Devices

1. Mount samples onto 6" Si carrier wafer using Santovac Oil
2. Etch Planar Microreactors (Oxford Cobra Plasmalab 100, 3.33 μm/min etch rate, 20 Pa Pressure, 250 sccm Cl_2, 0.5 sccm O_2 with a linear ramp increasing the O_2 flow rate by 0.5 sccm every 3 minutes, 2500 W ICP Power, 125 W RF Power, 10˚C)
3. Verify etch depth with Dektak surface profilometer and SEM
4. Place sample into Acetone bath for 72 hours to degrade the 3M double-sided tape, separating the Ti device from the Si chip
5. Finish cleaning the sample with Isopropanol and DI water

6. Dry with air and on hotplate at 115˚C

Ti DRIE for Micropillar Devices

1. Mount samples onto 6” Si carrier wafer using Santovac Oil
2. Etch Micropillar Microreactors (Panasonic E626I, 2.3 μm/min etch rate, 2 Pa Pressure, 100 sccm Cl_2, 5 sccm Ar, 400 W ICP Power, 100 W RF Power, 10˚C)
3. Verify etch depth with Dektak surface profilometer and SEM
4. Place sample into Acetone bath for 72 hours to degrade the 3M double-sided tape, separating the Ti device from the Si chip
5. Finish cleaning the sample with Isopropanol and DI water
6. Dry with air and on hotplate at 115˚C

Drilling Inlet and Outlet Vias

1. Use a 1/32” drill bit (Dremel 8220 at 20000 rpm) to create holes for the inlet and outlet
2. Grind down edge burr on backside of device using Dremel and sanding bit
3. Make sure that there are no edge burrs on both sides, edge burrs may cause leaks during the experimentation process
4. Ultrasonically clean samples in Acetone, Isopropanol, and DI water for 3 minutes each
5. Dry on hotplate at 115˚C for 5 minutes

Oxidizing NPT onto the Microreactors

1. Etch microreactors in 2.3% HF (200 ml DI water and 10 ml of 49% HF) for 40 seconds to remove passivation layer

2. Rinse in ultrasonic DI water bath for 5 minutes
3. Dry with N_2
4. Place into heated H_2O_2 at the optimized conditions (10%, 80˚C, 5 hours)
5. Removed sample from H_2O_2 and place into water
6. Remove sample from water and place into oven to anneal in air at 300˚C for 8 hours

Appendix E – Fixture Set Schematic

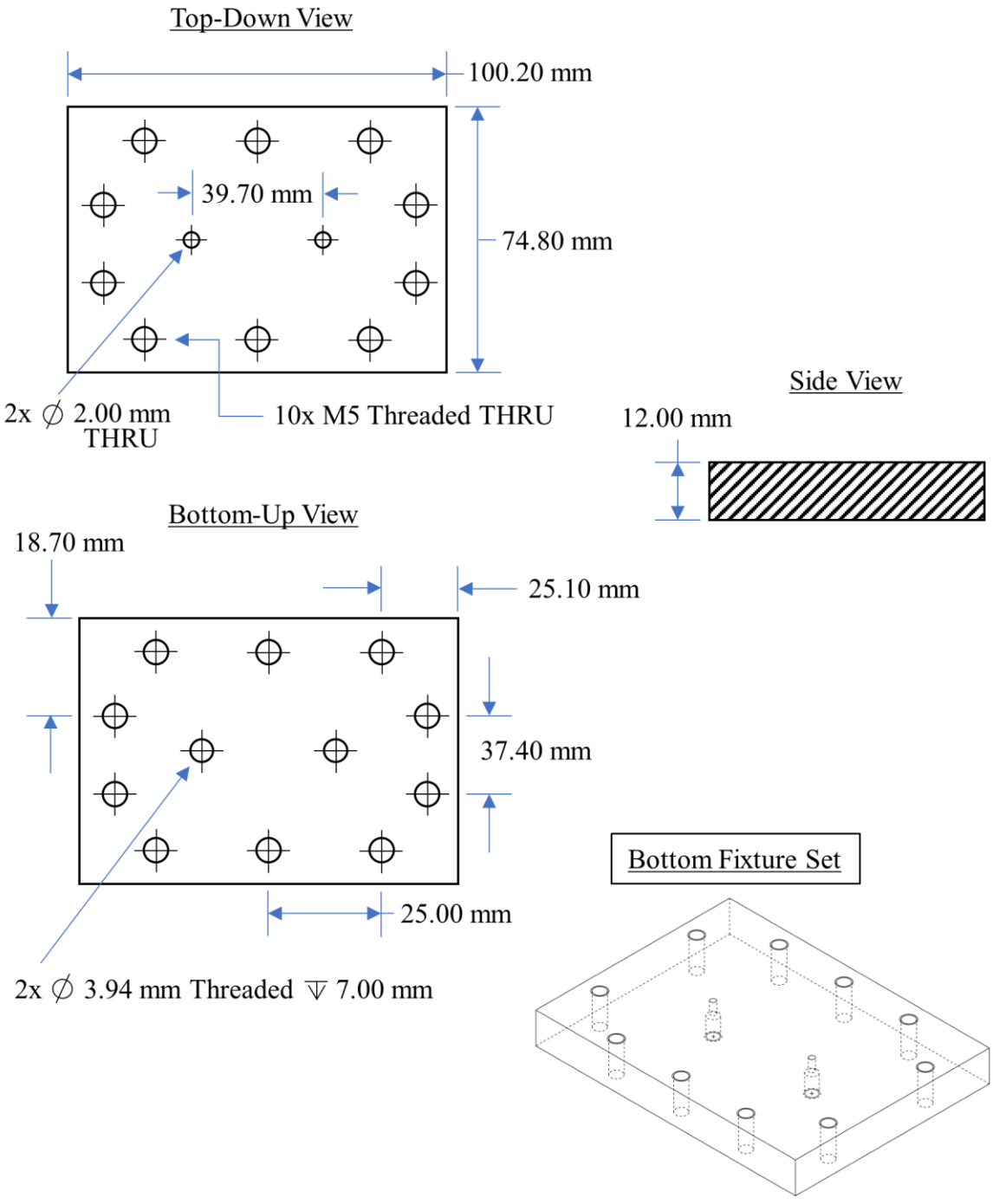

Figure E.1. Schematic of the Bottom Aluminum Fixture Set, see section 5.2.3.

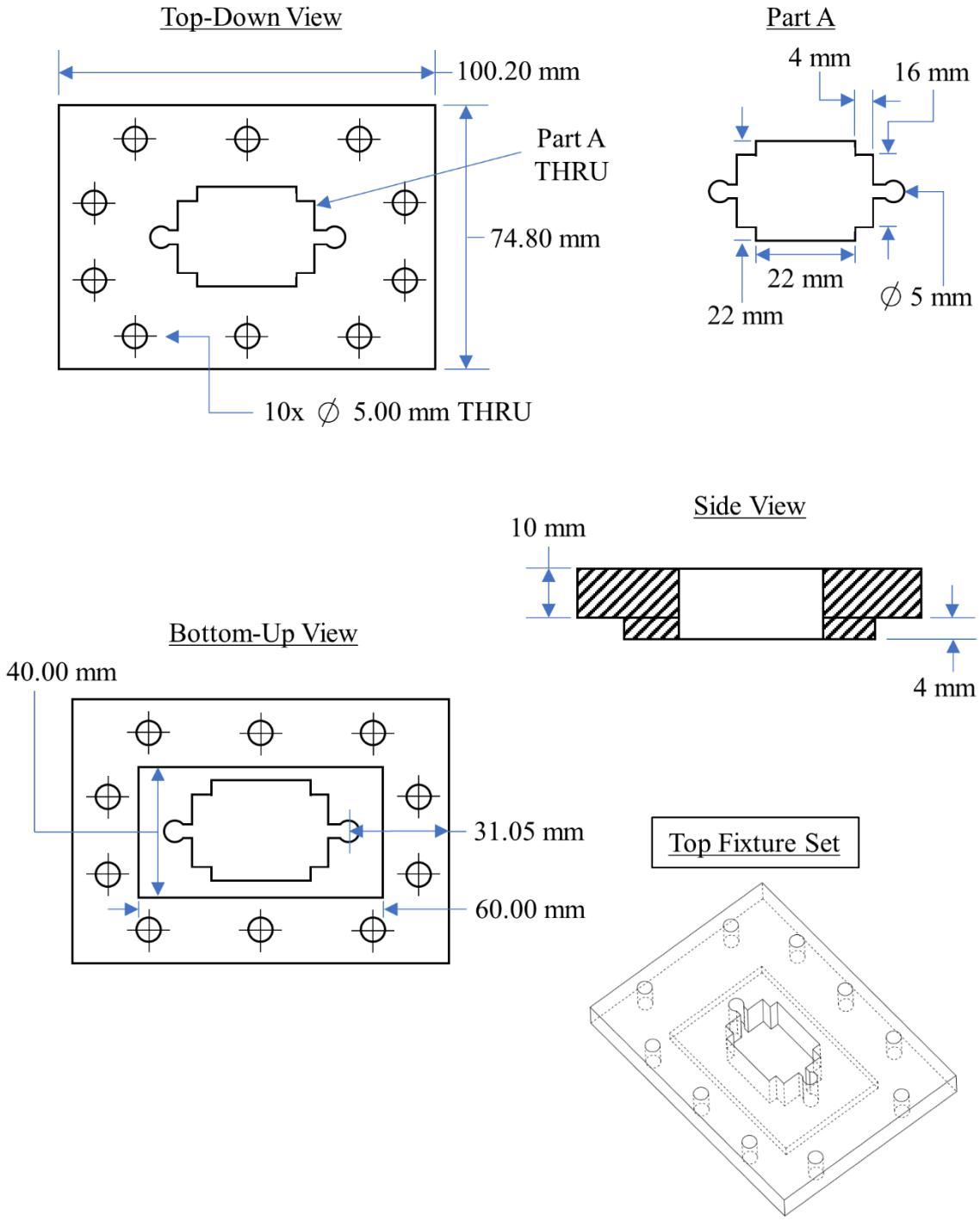

Figure E.2. Schematic of the Top Aluminum Fixture Set, see section 5.2.3.